DISSERTATION

FROM MEGACITES TO WILDFIRE SMOKE: OBSERVATIONAL CONSTRAINTS ON ATMOSPHERIC AMMONIA

Submitted by

Emily R. Lill

Department of Atmospheric Science

In partial fulfillment of the requirements

For the Degree of Doctor of Philosophy

Colorado State University

Fort Collins, Colorado

Spring 2026

Doctoral Committee:

Advisor: Emily V. Fischer

Jeffrey R. Pierce
Jeffrey L. Collett Jr.
Shantanu Jathar

ABSTRACT

FROM MEGACITES TO WILDFIRE SMOKE: OBSERVATIONAL CONSTRAINTS ON ATMOSPHERIC AMMONIA

Urban ammonia (NH_3) emissions are an increasingly important component of atmospheric nitrogen cycling and fine particulate matter ($PM_{2.5}$) formation, yet they remain poorly constrained in both observations and models. While agricultural sources have historically dominated NH_3 budgets, emerging evidence suggests that mobile sources and urban activities may play a larger role than currently represented in emission inventories. This dissertation quantifies the distribution, partitioning, and sources of reduced nitrogen ($NH_x = NH_3 + NH_4^+$) in major U.S. cities using aircraft observations from the 2023 Atmospheric Emissions and Reactions Observed from Megacities to Marine Areas (AEROMMA) campaign, and evaluates the ability of chemical transport models and satellite products to represent urban NH_3.

In Chapter 3, we explore the relationships between NH_3 and other urban pollutants using measurements collected from the NASA DC-8 aircraft during the AEROMMA field campaign in summer 2023. We report on NH_3 abundance, NH_x phase partitioning, enhancement ratios of NH_3 to carbon monoxide (CO), ethyne (C_2H_2), and nitrogen oxides ($NO_{x/y}$), and comparisons of enhancement ratios to previous studies. NH_3 abundance and NH_x phase partitioning varied based on city. Between Los Angeles (LA), Chicago, and New York City (NYC), LA had the highest average NH_3 concentration (4.3 ± 4.0 ppb) whereas NYC had the lowest average NH_3 concentration (0.8 ± 0.4 ppb). ΔNH3:ΔCO ratios ranged from 0.014 ± 0.002 ppb ppb^{-1} in NYC to 0.037 ± 0.004 in LA. The strong correlations with CO, C_2H_2, and $NO_{x/y}$ suggest that vehicles are

the dominant source of NH_3 during the summer months in these locations. The ΔNH_3:ΔCO ratio over NYC observed during the AEROMMA campaign is consistent with National Emissions Inventory (NEI) emissions for on-road vehicles, whereas the ΔNH_3:ΔCO ratios observed over LA and Chicago during AEROMMA are significantly higher than expected from the NEI on-road emissions.

In Chapter 4, we evaluate GEOS-Chem simulations against aircraft observations to assess biases in NH_3, NH_4^+, and NH_x. The model systematically underestimates urban NH_3 enhancements, particularly in traffic-influenced plumes, suggesting that mobile-source emissions are underestimated in current inventories. Biases in nitric acid (HNO_3) further propagate into errors in simulated ammonium nitrate formation (NH_4NO_3), indicating that improvements in both emissions and chemical mechanisms are needed. We also examine wildfire-influenced air masses and find that transported smoke exhibits higher observed NH_4^+ than simulated, pointing to incomplete representation of biomass burning emissions and aging pathways.

In Chapter 5, we evaluate the effects of the record-breaking 2023 Canadian wildfire season on NH_3 concentration and NH_4^+ deposition across the Upper Midwest. This study integrates satellite observations, ground-based data, and in situ aircraft measurements. In May - June 2023, NH_3 concentrations increased at 83% of ground sites, and NH_4^+ deposition flux rose at 100% of ground sites in the Upper Midwest. Satellite data showed significantly higher column-averaged NH_3 in 47% of grid cells in the Upper Midwest. On 1 August, a smoke plume over the Midwest corresponded with an AEROMMA flight observing enhanced NH_3, NH_4^+, carbon monoxide, and acetonitrile. These findings highlight the substantial impact of wildfire smoke on NH_3 and NH_4^+ at regional scales, with implications for nitrogen cycling, air quality, and atmospheric modeling.

ACKNOWLEDGEMENTS

A huge thank you to my advisor, Dr. Emily Fischer, who has been a mentor to me since my sophomore year of undergrad. You not only been pivotal in my development as a scientist, but also in developing my confidence in myself as a woman in science. I can't imagine where I would be without your mentorship these past seven years! Thank you to my committee, Dr. Jeff Pierce, Dr. Jeff Collett, and Dr. Shantanu Jathar. You all have been so helpful throughout this process and my Ph.D. I truly appreciate all of your insights and ideas; they pushed me and this dissertation to be the best possible. A special thank you to Dr. Ilana Pollack for teaching me the ways of aircraft field deployments. All of the skills you taught me during AEROMMA will benefit me beyond the field, no matter where life takes me.

I also want to thank all my friends that have supported me along the way. To my friends at CSU that have made my grad school experience unforgettable, Olivia Sablan, Ivy Glade, Madison Shogrin, Tyler Barbaro, En Li, Andrey Marsavin, the Fischer Group, and so many others, I couldn't have done it without you! To The Shack, Natalie Davic, Jenna Foust, Anna Prior, Gabi Winter, and Maya Zvavitch, you all are the best friends a girl could ask for! Your FaceTimes and support have meant so much. A massive thank you to my partner, Peter, who has supported me endlessness and has always been there to make me smile.

A huge thank you to my family who has encouraged and supported me throughout my life to go out and pursue my dreams. Thank you for always fostering my love of science. I would not be where I am today without you.

This dissertation would not have been possible without the combined efforts of the entire AEROMMA science team and the NASA Earth Science Project Office (ESPO) supporting the

field deployment. The funding for this work was provided by the U.S. National Oceanic and Atmospheric Administration (NOAA AC4 award #: NA21OAR4310127). The following table also acknowledges the specific contributions of various people to this dissertation.

Contribution	**Person/People**
AMS NH_4^+	Ann M. Middlebrook, Allison Piasecki
PILS NH_4^+	Amy Sullivan
LGR CO	Nell Schafer, Jeff Peischl
iWAS C_2H_2	Jessica B. Gilman, Victoria Treadaway, Morgan Selby
PTR-ToF-MS CH_3CN and Toluene	Chelsea E. Stockwell, Matthew M. Coggon, Kelvin H. Bates, Carsten Warneke
LIF NOx/y	Andrew Rollins, Eleanor M. Waxman, Kristen Zuraski
CIT-CIMS HNO3	John Crounse, Paul Wennberg, Katherine Ball
GEOS-Chem Model Output	En Li

TABLE OF CONTENTS

CHAPTER 1

INTRODUCTION[1]

Ammonia (NH_3) is the most abundant form of reduced nitrogen (N) in the atmosphere (Heald et al., 2012). Emissions of NH_3 worldwide are dominated by anthropogenic sources such as agriculture, industry, and biomass burning (Behera et al., 2013; Zeng et al., 2018). NH_3 contributes to the formation of fine particulate matter ($PM_{2.5}$), which negatively impacts human health, lessens air quality, reduces visibility, and impacts Earth's radiative balance (Bauer et al., 2007; Pope et al., 2009). NH_3 can also alter the global nitrogen cycle through both dry and wet deposition (Fowler et al., 2013). N cycling is necessary for many biological and chemical processes on Earth. There has been a doubling of anthropogenic N emissions since the Industrial Revolution, leading to an imbalance in the N cycle, which has caused an accumulation of N in bodies of water, soil, and, temporarily, in the atmosphere (Fenn et al., 1998; Fowler et al., 2013; Galloway et al., 2003). The environmental consequences of increasing N emissions, deposition, and accumulation include water eutrophication, soil acidification, and air pollution (Baron et al., 2000; Lieb et al., 2011; Wolfe et al., 2001, 2003; Wyer et al., 2022; Zhan et al., 2017).

N deposition in the United States (US) was previously dominated by oxidized N, but now is dominated by reduced N ($NH_x = NH_3 + NH_4^+$) (Li et al., 2016). This transition reflects the combined effects of substantial reductions in nitrogen oxides (NO_x) emissions following the Clean Air Act, which led to large declines in nitrate (NO_3^-) deposition, alongside increasing and largely unregulated NH_3 emissions from agricultural and other sources (Du et al., 2014; Liu et al., 2016; Pinder et al., 2008; Tong et al., 2015). Observational and modeling studies show that reduced

[1] Adapted from the introductions from Lill et al. (2025) and Lill et al. (submitted).

nitrogen now contributes roughly 60 - 65% of total inorganic nitrogen deposition nationally, with dry deposition of NH_3 playing a particularly important role (Li et al., 2016; Nopmongcol et al., 2019). Long-term records further demonstrate that this shift has occurred across much of the US, including the Upper Midwest, Northern Rockies, and other agricultural regions, where increasing NH_x deposition trends are often masked by more rapidly declining oxidized N deposition (Benish et al., 2022; Zhang et al., 2018). Signals of this compositional shift are also evident in watersheds, indicating that reduced N now represents the dominant or co-dominant form of atmospheric N deposition influencing many US ecosystems (Lassiter et al., 2023).

NH_3 emissions have increased worldwide over recent decades due to increasing livestock production and fertilizer use, rising temperatures, expanding industrial activity, and intensifying wildfire activity (Bray et al., 2021; Liu et al., 2022; Ma et al., 2025; Mgelwa et al., 2024; Yao & Zhang, 2016). Fertilizer application and livestock operations dominate emissions in many regions, while urban emissions have also contributed to localized increases in NH_3 (Li et al., 2017; Reche et al., 2022). These trends have not only led to elevated atmospheric NH_3 worldwide, but increasing NH_3 emissions have also altered N deposition patterns and exacerbated air quality issues in both rural and urban environments (Fenn et al., 2018; M. Liu et al., 2019; Luo et al., 2025; Zou et al., 2024). Despite the global increase, regional contributions vary substantially depending on population density, agricultural intensity, and regulatory controls, highlighting the need for targeted measurement and modeling efforts to capture both persistent sources and episodic events, such as wildfire emissions (Liu et al., 2022; Saylor et al., 2015; Tang et al., 2018; Wen et al., 2024).

Progress in quantifying NH_3 emissions and understanding its atmospheric behavior has been hindered by longstanding measurement challenges. NH_3 is highly reactive and adsorbs to

instrument surfaces, leading to sampling artifacts that complicate observations (von Bobrutzki et al., 2010). In addition, NH_3 participates in complex, bidirectional exchanges with terrestrial surfaces, which may act as either net sources or sinks depending on environmental conditions (Sutton et al., 1998). Emissions from soils and vegetation are influenced by factors such as land cover, soil and plant nitrogen content, temperature, and humidity, resulting in highly dynamic NH_3 fluxes at short temporal and spatial scales (Pleim et al., 2019). The direction and magnitude of NH_3 exchange are governed by the relationship between ambient NH_3 concentrations and the surface compensation point (χ) (Flechard et al., 2010; Langford et al., 1992; Nemitz et al., 2001; Wichink Kruit et al., 2007). Specifically, if the concentration of NH_3 is higher than χ, NH_3 deposition will occur. If the concentration of NH_3 is lower than χ, NH_3 will be emitted from the surface. If the concentration of NH_3 is close to χ, the direction of the NH_3 flux will change on brief timescales in response to changing micrometeorological conditions.

Recent advances in NH_3 measurement techniques, including high-time-resolution in situ instruments (Ellis et al., 2010; Pollack et al., 2019; Roscioli et al., 2016) and satellite retrievals (Shephard & Cady-Pereira, 2015; Van Damme et al., 2018), have substantially improved observational coverage. These observations have facilitated improved representation of NH_3 emissions in chemical transport models and exposed systematic underestimates in existing emission inventories at both regional and global scales (Heald et al., 2012; Nowak et al., 2012; Zhu et al., 2015). While substantial nitrogen deposition associated with NH_3 has been identified as a major threat to sensitive ecosystems in the United States and worldwide (Benedict et al., 2013; Liu et al., 2022), the atmospheric fate of NH_3 and its impacts on downwind environments remain incompletely understood. As NH_3 emissions continue to increase globally, high-quality

measurements are critical for constraining emissions, improving model performance, and assessing environmental impacts.

Based on current emission inventories, the fractional contribution of various sectors to overall annual NH_3 emissions varies by city within the U.S. (US EPA, 2023b). Figure 1.1 shows the fractional contribution of various sectors to the 2022 NEI annual estimate of NH_3 emissions in June – August for Chicago, New York City (NYC), and Los Angeles (LA), cities that will be further highlighted in this dissertation. These are the three most populated cities in the US. In the 2020 NEI, NH_3 emissions from agriculture contribute ~36% of estimated emissions in LA, ~39% in Chicago, and 33% in NYC, suggesting that nonagricultural sources of NH_3 are dominant in urban areas. In each city, on-road vehicles are the largest contributor to NH_3 emissions in the 2022 June - August NEI. However, the NEI may be missing some sources of NH_3, such as green spaces (Teng et al., 2017). It is also important to note that the NEI is based on estimates of emissions for various sectors, not measurements taken in each specific city. For example, the annual emissions estimates of NH_3 from residential combustion were taken from a 1985 report, and therefore, likely not representative of what modern residential equipment emits (Geadah, 1985; US EPA, 2004, 2023a, 2023b).

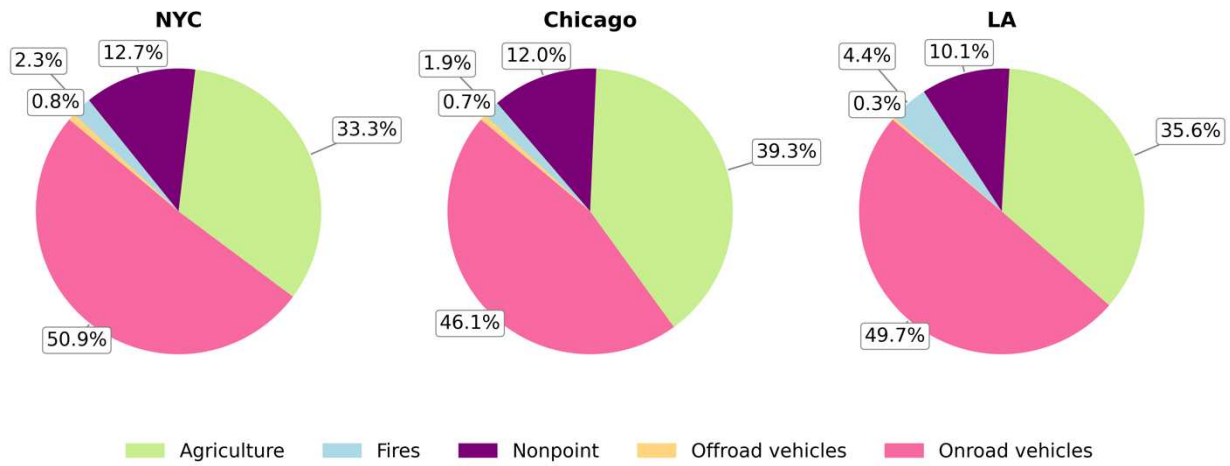

Figure 1.1: 2022 US EPA NEI estimated NH_3 emissions by sector for NYC (40.4 – 41.2°N, -74.5 – -73.5°E), Chicago (41.4 – 42.3°N, -88.3 – -87.2°E), and LA (33.7 – 34.4°N, -118.7 – -117.6°E) in June - August. Corresponding pie charts for CO can be found in Figure A1.

In U.S. urban areas, vehicles have been shown to be significant contributors to NH_3 emissions (Nowak et al., 2012; Sun et al., 2014; Toro et al., 2024). Urban NH_3 emissions are co-located with other aerosol precursors (e.g., NO_x and SO_x providing them with a differential opportunity to form fine particulate matter as opposed to rural areas (Duan et al., 2021; Yu et al., 2023). Urban areas are also densely populated, thus urban NH_3 emissions likely impact more people. NH_3 is not a direct combustion byproduct in vehicles. In gasoline vehicles, NH_3 is formed as a byproduct of nitric oxide (NO) reduction in three-way catalysts (Bishop & Stedman, 2015). Diesel vehicles newer than the 2010 model year use selective catalytic reduction systems to reduce nitrogen oxide (NO_X = NO + NO_2) emissions by injecting urea into the after-treatment system, which then decomposes to NH_3 (Toro et al., 2024). Unreacted NH_3 leaves the after-treatment system and is emitted into the atmosphere. However, modern diesel vehicles have NH_3 oxidation catalysts to remove excess NH_3 (Khalek et al., 2015).

Urban measurements of NH_3 are quite rare within North America (Bishop et al., 2010; Li et al., 2006; Nowak et al., 2012; Sun et al., 2014; Zhou et al., 2019). However, in the U.S., a growing body of evidence suggests that mobile NH_3 emissions have been underestimated in

emission inventories. Sun et al. (2017) found that vehicle emissions in the U.S. in 2013–2014 were more than twice those estimated in the 2011 National Emissions Inventory (NEI). Previous work has been done to characterize fuel-based NH_3 emissions from vehicles over time and found that reactive nitrogen emissions from newer vehicles are dominated by NH_3 (Bishop et al., 2010; Bishop & Stedman, 2015). Livingston et al. (2009) found that NH_3 emission rates from vehicles are highest from medium-duty vehicles, vehicles with odometer readings from 50,000–200,000 km, vehicles driven aggressively, and vehicles with high CO emissions. Walters et al. (2020, 2022) used nitrogen isotopes to identify a vehicle signature and used the vehicle signature to determine that ~47% of the annual urban background level of NH_x in Providence, Rhode Island can be attributed to vehicles. Cao et al. (2022) used changes in NH_3 and NO_2 observed from satellites during the COVID-19 lockdowns and determined that vehicle emissions in western L.A. account for 60%–95% of total NH_3 emissions. There are also a number of recent studies focused on Europe and China (Reche et al., 2012; Teng et al., 2017; Zhang et al., 2020). Within those studies, there is disagreement on whether traffic is (e.g., Reche et al., 2012; Zhang et al., 2020) or is not (e.g., Teng et al., 2017) an important source of urban NH_3.

Wildfires are the second largest source of atmospheric NH_3 in the US, with emissions expected to increase as the number and severity of wildfires grow due to climate change (Bray et al., 2018, 2021). Aircraft measurements from the Western Wildfire Experiment for Cloud Chemistry, Aerosol Absorption and Nitrogen (WE-CAN) field campaign demonstrated that wildfires can emit large quantities of reduced nitrogen, which can influence air quality and nitrogen cycling downwind (Calahorrano et al., 2021; Lindaas et al., 2021a; Lindaas et al., 2021b). Excess nitrogen from wildfires can also lead to the nitrogen critical load being exceeded in forests, which has adverse effects on vegetation (Campbell et al., 2022; Koplitz et al., 2021). Previous studies

have observed local enhancements of NH_3 and NH_x (NH_3 + ammonium (NH_4^+)) during fire events (Chen et al., 2014; Saylor et al., 2015); however, the broader spatial and temporal impact of wildfires on NH_3 concentration and NH_4^+ deposition across the United States remains poorly quantified.

Chemical transport models (CTMs) utilize inventories to estimate atmospheric NH_3 (Nair & Yu, 2020). Therefore, when inventories misrepresent NH_3 emissions, the misrepresentations propagate into the CTM predictions. GEOS-Chem is widely used to investigate these processes because it couples atmospheric chemistry with meteorology and community-developed emission inventories, making it a standard framework for evaluating NH_3 sources, chemistry, and deposition (Marais et al., 2021; Salcedo et al., 2025; Zhu et al., 2013). Beyond challenges with estimating emissions, NH_3 undergoes partitioning between the gas and particle phases through reactions with H_2SO_4 and HNO_3, which must also be represented in models. This chemistry and thermodynamics is commonly represented using thermodynamic equilibrium schemes such as ISORROPIA II (Fountoukis & Nenes, 2007). ISORROPIA II is optimized for computational efficiency and is the most used thermodynamic equilibrium module within GEOS-Chem. However, the assumption of equilibrium may not be correct under all conditions, which then require mass transfer dynamical schemes for gas-particle partitioning.

Another challenge for CTMs is capturing the deposition and bi-directional exchange of NH_3. The representation of deposition in models is difficult as deposition is dependent on a multitude of factors, including the concentration of NH_3 above the specific surface, the equilibrium of NH_3 over the surface determining whether emission or deposition occurs, meteorological conditions, and the type of vegetation/surface (Behera et al., 2013; Massad et al., 2010; Zhang et al., 2010). Although incorporating bidirectional NH_3 exchange in GEOS-Chem improved the

representation of surface-atmosphere exchange and diurnal variability of NH_3, it did not resolve the persistent low bias in modeled NH_3 concentrations, highlighting that emission inventory uncertainties, rather than exchange processes alone, dominate model-observation discrepancies (Zhu et al., 2015). Currently, GEOS-Chem does not natively include an operational bidirectional NH_3 exchange scheme. Finally, model evaluation is hindered by the limited spatial and temporal coverage of NH_3 observations. Previous work suggests that GEOS-Chem underestimates NH_3 when compared to both satellite and in-situ observations (Heald et al., 2012; Walker et al., 2012; Zhang et al., 2012).

Here, I investigate atmospheric NH_3 from two increasingly important and understudied sources in the US: urban regions and extreme wildfire events. Urban regions are characterized by dense populations, complex emissions, and strong coupling between NH_3 and acidic aerosol precursors, making them critical environments for evaluating NH_3 impacts on air quality and human exposure. The record-breaking 2023 Canadian wildfire season provides a unique natural experiment to examine the regional-scale influence of episodic NH_3 emissions and their transport into the Upper Midwestern United States. Recent observational studies suggest that NH_3 emissions from mobile sources in urban environments are underestimated in emission inventories, with implications for CTM performance and predictions of particulate matter formation. At the same time, wildfires represent the second largest source of atmospheric NH_3, yet their contribution to downwind NH_3 concentrations and NH_4^+ deposition remains poorly constrained, particularly during extreme fire seasons. Together, these sources challenge existing modeling frameworks due to uncertainties in emissions, chemical partitioning, transport, and deposition processes.

Overview of dissertation chapters and goals

This dissertation provides new observational constraints on atmospheric NH_3 from vehicular and wildfire sources and evaluates their representation in the GEOS-Chem chemical transport model. This analysis centers on aircraft measurements from the Atmospheric Emissions and Reactions Observed from Megacities to Marine Areas (AEROMMA) field campaign taken over NYC, Chicago, and Los Angeles (LA). The AEROMMA field campaign occurred in summer 2023, coinciding with the extreme Canadian wildfire season, and is further discussed in Chapter 2. I also integrate surface NH_3 observations from the Ammonia Monitoring Network (AMoN), NH_4^+ deposition flux data from the Clean Air Status and Trends Network (CASTNET), and satellite-derived, column average NH_3 from the Cross-track Infrared Sounder (CrIS) to assess both persistent urban emissions and episodic wildfire-driven enhancements, and examines how urban emissions are represented in models. This work focuses on 1) identifying sources and quantifying NH_3 emissions in major U.S. metropolitan areas using airborne observations and evaluating their representation in emission inventories; 2) assessing the ability of GEOS-Chem to reproduce observed NH_3, NH_4^+, and NH_x distributions in urban environments, with a focus on vertical structure, gas-particle partitioning, and source attribution; and 3) characterizing the magnitude, transport, and air quality impacts of NH_3 emitted during the 2023 Canadian wildfires as smoke was transported into the Upper Midwestern US. Together, these analyses provide a comprehensive observationally constrained picture of urban and wildfire NH_3 emissions, their chemical evolution, and their regional-scale impacts. Chapter 2 outlines the common methodology employed in this research.

Chapter 3 contains the results of a paper published in the *Journal of Geophysical Research* (JGR) in 2025 (Lill et al., 2025). Using airborne observations collected during the AEROMMA

field campaign over NYC, Chicago, and LA, this chapter characterizes NH_3 emissions from mobile sources in urban environments. Specifically, this work reports a) observed relationships between NH_3 and mobile-source tracers across different urban regions and meteorological conditions, b) constraints on the magnitude of vehicular NH_3 emissions relative to existing bottom-up inventories, and c) evidence for systematic underestimation of mobile-source NH_3 emissions in current emissions inventories. Together, these analyses demonstrate that vehicular emissions are a major and under constrained contributor to urban reduced nitrogen.

In Chapter 4, I assess the GEOS-Chem representation of reduced nitrogen in NYC and Chicago using observations from AEROMMA. By comparing model output sampled directly along aircraft flight tracks, I evaluate the model's ability to simulate the vertical distribution, temporal variability, and partitioning of reduced nitrogen. Specifically, this work a) identifies systematic model underestimations of high-concentration urban plumes, particularly those linked to mobile-source tracers, b) reveals deficiencies in the representation of sub-daily emission variability, and c) demonstrates that inaccuracies in simulated HNO_3 drive biases in ammonium nitrate (NH_4NO_3) formation. These results provide an evaluation of GEOS-Chem estimations of reduced nitrogen in urban environments, highlighting where current bottom-up inventories and chemical mechanisms fail to capture the intensity and timing of localized reduced nitrogen enhancements.

Chapter 5 has been submitted for publication to *Geophysical Research Letters* (GRL) (Lill et al., submitted). Using a combination of satellite-derived NH_3 columns, surface concentration and deposition measurements, and AEROMMA aircraft observations of a transported smoke plume, this chapter presents a detailed analysis of wildfire-driven enhancements in reduced nitrogen. Specifically, this work a) documents large-scale NH_3 enhancements associated with

long-range transport of wildfire smoke; and b) quantifies the influence of these events on surface NH_3 concentrations and NH_4^+ deposition. These results highlight extreme wildfire seasons as consequential sources of atmospheric NH_3 far downwind of emission regions.

Finally, Chapter 6 summarizes the findings in this dissertation and explores future research pathways.

CHAPTER 2

METHODS

2.1 AEROMMA CAMPAIGN OVERVIEW AND FLIGHT SEGMENTS

The summer 2023 AEROMMA field campaign deployed the NASA DC-8 with the goal of understanding air pollution in North American megacities in a changing climate. The DC-8 was stationed in Palmdale, CA from 16–28 June to 19–26 August 2023 and Dayton, OH between 26 July and 16 August 2023. During the Palmdale deployments, the DC-8 sampled the LA, CA metropolitan areas, whereas Dayton deployments sampled Chicago, IL, NYC, NY, and Toronto (Ontario, Canada). The flight dates and times used in Chapter 3 are LA (8/23, 8/25, 8/26; with times varying between 10:50 a.m. and 7:19 p.m. PDT), Chicago (8/1, 8/2, 8/8, 8/12, 8/15; with times varying between 10:57 a.m. and 3:47 p.m. CDT), NYC (7/28, 8/9, 8/16; with times varying between 9:49 a.m. and 7:08 p.m. EDT), and Toronto (8/4, 8/5; with times varying between 9:40 a.m. and 5:40 p.m. EDT). Flight plans varied between cities, and example flight tracks are shown in Figure 2.1. NYC, LA, and Toronto flights utilized a similar sampling strategy where the flight patterns were fixed regardless of wind direction due to air traffic control constraints, whereas flight patterns in the Chicago area were adjusted to accommodate changing wind patterns. Flight segments used for this analysis were chosen by selecting the urban and immediate surrounding areas below 2,000 ft above ground level (AGL), which was typically well within the boundary layer during the time of the flights. The AEROMMA field campaign also conducted flights over LA on 6/27 and 6/28, but observations from these flights were not included in this study because data was missing for some of the species used in this analysis. Further information can be found on the AEROMMA project site (https://csl.noaa.gov/projects/aeromma/).

Figure 2.1: Maps of example low/no smoke flight tracks <2,000 ft AGL in LA (26 August 2023): (33.7–34.2°N); (241.7–242.8°W), NYC (16 August 2023): (40.2–41.6°N); (285.8–287.0°W), and Chicago (12 August 2023): (41.3–43.1°N); (271.4–273.3°W colored by NH3 mixing ratios. Wind roses for each flight are included on the map. The corresponding time series for the data presented in maps can be found in Figure B2 of Supporting Information. The color scales used in this Figure for each city are different but kept consistent throughout this study to differentiate between cities.

2.2 Smoke Impact Designation for AEROMMA Flights

Canada was impacted by unprecedented wildfires during summer 2023, and the smoke impacted much of the midwestern and northeastern U.S. (Cooper et al., 2024; Wang et al., 2024). Due to the impact of these wildfires on the AEROMMA dataset, we separated observations from research flights into two categories: smoke-impacted and low/no smoke. We classify observations from an entire research flight as smoke-impacted if the mean acetonitrile (CH_3CN) for the flight is > 200 parts per trillion (ppt) below 2000 ft AGL, which was typically well within the boundary layer during the time of the flights or if there is a medium to heavy NOAA Hazard Mapping System (HMS) smoke plume overlapping the flight area. NOAA HMS smoke plumes are generated daily by trained satellite analysts and they provide information on where smoke is located in that atmospheric column over North America (Brey et al., 2018; Ruminski et al., 2006). We classify a flight as low/no smoke if it does not meet either criterion. Table A1 includes mean CH_3CN and HMS plume information for each flight. CH_3CN is a commonly used tracer of smoke; its dominant source is biomass burning and it has a long (i.e., months to years) atmospheric lifetime (de Gouw et al., 2003). Previous studies (Lill et al., 2022; O'Dell et al., 2020) have also used the designation

of CH_3CN > 200 ppt to identify smoke-impacted conditions. There are no significant sources of CH_3CN in urban environments (de Gouw et al., 2003; Holzinger et al., 2001; Wang et al., 2024). HMS smoke plumes were also used to confirm smoke-impacted conditions given variability in the amount of CH_3CN present and several flights were characterized by average CH_3CN values near the 200 ppt threshold. The approximate smoke age was calculated with NOAA HYSPLIT back trajectories. Back trajectories were run on flight days with starting locations over the sampled city using Global Data Assimilation System **(**GDAS) meteorology.

2.3 Calculation of Enhancement Ratios Using Reduced Major Axis Regression

We use the slope calculated from a reduced major axis (RMA) regression of NH_3 versus various co-emitted species in the boundary layer of each of the studied cities. The calculated slopes from the RMA regression are presented in this study as enhancement ratios which can be used as a proxy for emission ratios when they are collected near a source (Nowak et al., 2012). The calculated enhancement ratios represent $\Delta NH_3/\Delta$tracer, thus this is the ratio of the species above the relative background values for each species. We used RMA regression because it accounts for errors in both the x and y variables and minimizes orthogonal distances between points and the regression line (Harper, 2016). To calculate the uncertainty in the slope, we applied bootstrapping by adding random noise based on the measurement errors. We then recalculated the slope using the bootstrapped samples and computed the error as the standard deviation of the bootstrapped slopes. Multivariate linear regression (MLR) was also used for select flights to estimate the relative contribution of emission sources. This approach has been used in previous studies to separate different sources of a single species (Gilman et al., 2013; Kille et al., 2019; Pollack et al., 2022).

2.4 U.S. EPA National Emissions Inventory

We use data from the U.S. Environmental Protection Agency's National Emissions Inventory (US EPA, 2023) to estimate on-road emission ratios. This dataset provides estimates for various pollutants across multiple source categories. For this study, we use NH_3 and CO emissions estimates from on-road mobile sources to calculate estimated on-road ΔNH_3:ΔCO emissions ratios for each city. NEI on-road vehicle emissions are estimated using the Motor Vehicle Emission Simulator (MOVES) for all states with the exception of California, which are estimated using the EMission FACtor (EMFAC) model (Toro et al., 2024).

2.5 Measurement Techniques

2.5.1 Gas-Phase NH_3

NH_3 was measured using a commercial, single-channel, quantum-cascade tunable infrared laser direct absorption spectrometer (Aerodyne Research, Inc. QC-TILDAS) which is described in detail in previous literature (Ellis et al., 2010; McManus et al., 1995, 2010; Zahniser et al., 1997). Briefly, the NH_3 QC-TILDAS operates at 967 cm^{-1} with an effective path length of 76 m and uses a high sample flow rate (>10 SLPM) and a direct absorption technique to attain an NH_3 mixing ratio collection frequency of up to 10 Hz (averaged to 1 Hz for the AEROMMA dataset). For AEROMMA, the NH_3 QC-TILDAS used an inertial inlet located upstream of the spectrometer inside an enclosure maintained at 40°C to separate particles > 300 nm in diameter from the sample stream without the use of a filter (Ellis et al., 2010; Ferrara et al., 2012). Ellis et al. (2010) reported that the inertial inlet, which acts like a form of virtual impactor, removes more than 50 % of particles larger than 300 nm. This implies that if there were high concentrations of NH_4^+, NH_3 measurements would be biased high. For example, if the instrument sampled 2 ppb of NH_3 and 0.5 ppb of NH_4^+ and 50% of the NH_4^+ passed through the inertial inlet, the measurement would be

biased high by 12.5%. Instrument sampling surfaces were continuously passivated with 1H,1H-perflurooctylamine ($C_8H_4F_{15}N$, CAS number: 307-29-9) vapor, injected approximately 9 cm downstream of the inlet tip to improve response time (Pollack et al., 2019; Roscioli et al., 2016). The NH_3 QC-TILDAS was mounted on a vibration isolation plate and had a continuous high-frequency vibration applied to the laser objective to wash out etalon fringe motion from aircraft acceleration to reduce the impact of motion sensitivity on the instrument (Pollack et al., 2019). The instrument was calibrated on the ground with a known concentration of NH_3 from a temperature-controlled permeation tube. The calibration gas was injected into the sample stream approximately 10 cm downstream of the inlet tip. The permeation tube's emission rate was calibrated both before and after the AEROMMA field campaign by the NOAA ultraviolet (UV) optical absorption system (Neuman et al., 2003). The NH_3 QC-TILDAS was zeroed in flight and on the ground by overflowing the inlet tip with NH_3-free air from either a bottled source of ultrapure synthetic zero air (UZA; AIRGAS) or a commercial zero air generator (ZAG) (Teledyne, model 701H). Both sources of zero air provided a consistent zero signal level. Following the procedure for calculating overall uncertainty in Pollack et al. (2019), individual uncertainties were added in quadrature, resulting in a combined uncertainty of ±12% of the measured mixing ratio, with a 200 pptv limit of detection.

2.5.2 AMS Particle-Phase NH_4

Non-refractory particulate mass was obtained with an Aerodyne High-Resolution, Time-of-Flight Aerosol Mass Spectrometer (HR-AMS) using a PM_1 inlet (DeCarlo et al., 2006). Aerosols were sampled using the NSF/NCAR High-performance Instrumented Airborne Platform for Environmental Research (HIAPER) modular inlet (HIMIL) that was previously characterized for the DC-8 aircraft (Guo et al., 2021). A constant mass flow rate into the HR-AMS as the aircraft

changed altitude was maintained with a pressure-controlled inlet (Bahreini et al., 2008). Data were typically obtained at 1 Hz, in cycles of 6 s for background correction, 46 s for sampling unsized, total aerosol mass, and 8 s for sampling total aerosol mass distributions as a function of size. The AMS was calibrated periodically with NH_4NO_3 particles using the internal sizing to obtain both the ionization efficiency for NO_3^- and the relative ionization efficiency for NH_4^+. For the final HR-AMS data, the detection limit for NH_4^+ is between 0.01 and 0.02 μg m^{-3} for individual flights and its overall uncertainty is ±34% (Bahreini et al., 2009).

2.5.3 PILS Particle-Phase NH_4

NH_4^+ was measured using a Particle-into-Liquid Sampler (PILS) coupled with a fraction collector. After particles are grown inside the body of the PILS by mixing cool air with hot steam, the particles are collected by an impactor, and then washed off by a continuous flow of liquid water passed over the impactor, providing a liquid sample with the aerosol particles dissolved in it (Orsini et al., 2003). The PILS sampled from the LARGE aerosol inlet. The PILS size-cut was provided by a non-rotating MOUDI impactor stage with a 50% transmission efficiency at 1 atm ambient pressure of 1 μm (PM_1) (Marple et al., 1991). The flow rate for the PILS was 15 LPM sampling from one of the LARGE aerosol inlet lines. Sodium carbonate- and phosphorous acid-coated denuders were placed upstream of the PILS to remove gaseous interferences. A valve upstream of the PILS was manually closed for 10 min, forcing the airflow through a HEPA filter to obtain a measurement of the background in near real-time.

The liquid sample from the PILS was sent to a Brechtel Fraction Collector to collect samples for offline analysis (Sorooshian et al., 2006). The PILS liquid flow rates were set to continuously collect ~1.2 mL of liquid sample every 2 min (Juncosa Calahorrano et al., 2023; E. Li et al., 2024; Sullivan et al., 2022). Pre-loaded carousels were manually switched during flight.

After each flight, the vials were unloaded, recapped with solid caps, and shipped back to CSU in coolers with ice packs to be stored in a 2°C cold room until analyzed by ion chromatography.

NH_4^+ was determined using a Dionex ICS-3000 ion chromatography with a pump, conductivity detector, and self-regenerating cation suppressor. A Dionex IonPac CS12A-5 μm analytical column (3 × 150 mm) using an eluent of 20 mM methanesulfonic acid at a flow rate of 0.5 mL/min was used for the separation. The injection volume and analysis time were 190 μL and 17 min, respectively. The NH_4^+ uncertainty is ±10%.

2.5.4 Carbon monoxide

Carbon monoxide (CO) was measured using a modified commercial Los Gatos Research instrument (model no. F-N_2O/CO-23r) which uses off-axis integrated cavity output spectroscopy. Ambient air was sampled through a pressure-building inlet and 6.4 mm OD (¼") stainless steel tubing at approximately 3 slpm (Bourgeois et al., 2022). The instrument was calibrated using high and low-standard tanks calibrated to the WMO X2014A scale. The precision for 1-Hz data is estimated to be ±0.2 parts per billion (ppb), and overall uncertainty is estimated to be ±2% for CO. Data are reported as dry air mole fractions.

2.5.5 Ethyne

Ethyne was measured using whole air samples (WAS) collected onboard the DC-8 and analyzed offline via a custom-built dual-column gas chromatography-mass spectrometry (GC-MS) instrument described in Lerner et al., 2017. For AEROMMA, up to 144 WAS were filled during each flight. The mean sample fill time was 5.4 seconds, and the mean final fill pressure was 52 psia. Each WAS was then analyzed on the GC-MS system, typically within 6 days of collection. Ethyne was calibrated using a 56 hydrocarbon mix (Ozone Precursor Mix/PAMS, Restek #26368).

The overall uncertainty for ethyne is ±15%. The 1-Hz NH_3 data was averaged over the linear canister fill times.

2.5.6 Acetonitrile and Toluene

Acetonitrile and toluene were measured onboard the DC-8 by a Vocus proton-transfer-reaction time-of-flight mass spectrometer (PTR-ToF-MS). Air was sampled at 0.1–2 L min^{-1} through a 1 m Teflon inlet. The Vocus drift tube was operated with a reduced electric field (E/N) of ~140 Td and the sensitivities to acetonitrile, toluene, and many other VOCs were determined using gravimetrically prepared gas standards (Apel-Riemer Environmental, Inc.) or by liquid calibrations. Mixing ratios for calibrated species have uncertainties of ~30%. Data were recorded at 5 Hz but reported as 1s averages (Coggon et al., 2024).

2.5.7 NO_x/NO_y

NO_x and NO_y were measured using the NOAA Laser-Induced Fluorescence (LIF) instrument (Rollins et al., 2020). Briefly, NO is excited at 215 nm using a custom-built laser and the fluorescence is measured at red-shifted wavelengths between about 255 and 267 nm. During AEROMMA, the instrument operated with three channels to enable measurements of NO, NO_x, and NO_y separately. Each channel had its own inlet to convert, if necessary, oxidized nitrogen species to NO. The NO_x inlet had a quartz photolysis tube illuminated by an LED centered at 295 nm to photolyze NO_2 to NO with a photolysis efficiency of 40±1%. The NO_y inlet contained a heated Teflon inlet connected immediately to a 30 cm gold catalytic converter heated to 300°C which quantitatively converts NO_y species to NO (Ryerson et al., 1999). The conversion efficiency was calibrated using both NO_2 and HNO_3 and the conversion efficiencies for these species was unity within the uncertainty of the measurements. Standard addition of NO to each channel provided concentration calibrations in flight. During AEROMMA, calibration uncertainties were

±6% for NO, ±9% for NO_2, and ±10% for NO_y. Zero uncertainties, determined by overflowing the inlets with zero air in-flight, were 3 ppt for NO, >5 ppt for NO_2, and 100 ppt for NO_y. The LIF precision during AEROMMA in the boundary layer was nominally 2 ppt for NO, 10 ppt for NO_2, and 10 ppt for NO_y.

2.5.8 Nitric Acid

Nitric acid (HNO_3) was measured with the California Institute of Technology Chemical Ionization Mass Spectrometers (CIT-CIMS), that combines a compact Time-of-Flight mass spectrometer (C-ToF, Tofwerk/Caltech) with a triple quadrupole mass spectrometer (Varian/Caltech) (Allen et al., 2022). Both instruments use a soft chemical ionization technique to detect oxygenated compounds. C-ToF data was used to report ambient mixing ratios at a 1 Hz frequency for HNO_3 (m/z = 82). HNO_3 uncertainty was ±20% of measurement value + 25 pptv.

2.5.9 Ground-Based NH_3 Concentration

We use data from the National Atmospheric Deposition Program (NADP) Ammonia Monitoring Network (AMoN), which provides bi-weekly NH_3 concentration data (Puchalski et al., 2015). AMoN uses Radiello® passive samplers, which absorb NH_3 onto an inner cartridge coated with phosphoric acid, inside of a porous outer body. The NH_3 is then extracted from the cartridge as NH_4^+ and analyzed by Flow Injection Analysis (FIA). The bi-weekly limit of detection is ~0.078 μg NH_3 m^{-3} (https://nadp.slh.wisc.edu/networks/ammonia-monitoring-network/).

2.5.10 Ground-Based NH_4^+ Deposition Flux

We use NH_4^+ deposition flux data from the Clean Air Status and Trends Network (CASTNET), which provides weekly estimates of NH_4^+ dry deposition fluxes (Clarke et al., 1997; US EPA, 2009). CASTNET uses a 3-stage filter pack where NH_4^+ is captured on the first stage (Teflon filter). NH_4^+ dry deposition flux is then calculated as the product of NH_4^+ concentration

and the modeled deposition velocity computed using the Multi-Layer Model (MLM). The MLM accounts for the atmospheric and surface resistances at the site.

2.5.11 Satellite-based NH_3

We use daytime satellite observations of NH_3 from the Cross-track Infrared Sounder (CrIS) instrument on the Suomi-National Polar-orbiting Partnership (S-NPP) satellite, which flies in a sun-synchronous polar orbit with 13:30 local time overpass time. We use data sets produced under the NASA Tropospheric Ozone and Precursors from Earth System Sounding (TROPESS) project (Bowman, 2021). Information on the CrIS NH_3 retrieval algorithm can be found in Shephard & Cady-Pereira (2015). CrIS is most sensitive to NH_3 around 850-750 hPa and has on average 1 Degree of Freedom (DOF) for signal, meaning the product lacks information about the vertical distribution of NH_3 in the atmosphere (Shephard & Cady-Pereira, 2015). The thermal infrared radiances measured by CrIS are more sensitive to changes in atmospheric NH_3 aloft than they are to similar changes at the surface, so the standard CrIS TROPESS NH_3 measurements reported here likely represent an overestimate of NH_3 in lofted smoke. Recent work has used co-measured CO to correct this overestimate and we estimate the correction is approximately 50-80%. We utilize CrIS column average NH_3 on a 1.5° grid for our analysis.

2.6 Smoke Impact Designation for Ground-Based Sites

NOAA Hazard Mapping System (HMS) plumes were used to determine if an AMoN or NTN site was situated under a smoke plume, which we classify as potentially smoke-impacted in the Upper Midwest. For this study, we define the Upper Midwest as Minnesota, Wisconsin, Michigan, and the northern portion of Indiana and Illinois (above 41.5°N). NOAA HMS smoke plumes are generated daily by trained satellite analysts and provide information on where smoke is located in an atmospheric column during daylight hours only (Brey & Fischer, 2016; Ruminski

et al., 2006). We utilize HMS data from 01 January 2011 to 31 December 2024. We classify an AMON sample as having a high probability of smoke-impact if there was an HMS plume overhead of the measurement site for >50% of the days within its 2-week sampling period, a low/medium probably of smoke-impact if there was an HMS plume overhead of the measurement site for >0% & <50% of its 2-week sampling period, and likely smoke-free if there was an HMS plume overhead for 0% of the 2-week sampling period.

2.7 Model Description

We use the GEOS-Chem chemical transport model version 14.3.0. Simulations are performed globally at a 4˚x5˚ (lat x lon) resolution and a nested grid over North America at a 0.25° x 0.3125° (lat x lon) resolution. The vertical domain is resolved into 47 hybrid-sigma layers extending from the surface to ~80 km altitude. The simulation is driven by the MERRA-2 assimilated meteorological data product from the NASA Goddard Global Modeling and Assimilation Office (GMAO), and the nested simulation is driven by the GEOS-FP meteorology product. Time steps are 60 min for chemistry and 30 min for transport for the global simulations and 5 min for chemistry and 10 min for transport for the nested simulations.

GEOS-Chem simulates detailed gas-phase chemistry coupled to the sulfate (SO_4^{2-}) -NO_3^--NH_4^+ aerosol system (Park et al., 2004; Pye et al., 2009), incorporating updated treatments of HO_2 uptake (Mao et al., 2013) and the reactive uptake of NO_2, NO, and N_2O_5 by aerosols and clouds (Holmes et al., 2019; McDuffie et al., 2018). Dust and sea salt aerosols are represented using discrete size bins, with four bins for dust (0.1–1.0 μm, 1.0–1.8 μm, 1.8–3.0 μm, and 3.0–6.0 μm) and two bins for sea salt (0.01–0.5 μm and 0.5–8 μm). Sodium is diagnosed as a fixed fraction of fine sea salt aerosol, corresponding to 39.7 % by mass. Aerosol size distributions are described using a bulk scheme with fixed log-normal modes (Martin et al., 2003). Dry deposition of gases is

treated using a resistors-in-series framework (Wang et al., 1998; Wesely, 1989), while aerosol dry deposition is size dependent (Emerson et al., 2020; Zhang et al., 2001). Wet deposition includes rainout, washout, and scavenging within moist convective updrafts for both gases and aerosols (Amos et al., 2012; Liu et al., 2001; Wang et al., 2011, 2014). Gas-particle partitioning is calculated using the ISORROPIA II thermodynamic equilibrium model (Fountoukis & Nenes, 2007; Pye et al., 2009), run in the default metastable mode, which assumes inorganic aerosols remain on the upper branch of the hygroscopic hysteresis curve.

GEOS-Chem simulations were matched to corresponding AEROMMA flights. Analysis was restricted to flights sampling the Toronto, Chicago, and New York City metropolitan regions, excluding west coast deployments. Only measurements in the planetary boundary layer (PBL) were retained. Boundary layer points were identified using a campaign-provided boundary layer classification flag. Each aircraft observation was mapped to the nearest GEOS-Chem grid cell in space, time, and pressure using archived GEOS-Chem meteorological output. Temporal indices were assigned by identifying the closest model time step to each observation. Horizontal indices were determined by locating the nearest and second-nearest latitude and longitude grid centers to allow for bilinear interpolation. Vertical indices were assigned using model mid-level pressures. For each observation pressure, the nearest model level was identified in log-pressure space, and a fractional weighting between adjacent vertical levels was computed to enable linear interpolation in log-pressure coordinates. This approach ensured consistency between model vertical structure and aircraft sampling altitude, as well as smoothed discontinuities as between discrete model grid boxes that better reflect the continuous nature of the atmosphere. Anthropogenic emissions for the United States are from the 2016 EPA NEI (US EPA, 2019). This is year-specific to 2023, which is based on annual-scale factors derived from emissions trends from 2016–2023. For other global

emissions, the model also includes anthropogenic (including shipping) emissions from CEDS v2 (Hoesly et al., 2018), biomass burning emissions from QFED2 (Darmenov, 2015) , lightning NO_x emissions (Murray et al., 2012), offline dust emissions (Meng et al., 2021), offline soil NO_x emissions (Hudman et al., 2012), dimethyl sulfide (DMS) emissions (Breider et al., 2017; Lana et al., 2011), aircraft emissions from AEIC 2019 (Eastham & Fritz, 2022), and natural NH_3 emissions from soils, oceans, vegetation, and wild animals based on the GEIA inventory (Bouwman et al., 1997).

CHAPTER 3

AMMONIA OBSERVATIONS OVER LARGE NORTH AMERICAN CITIES

3.1 ABUNDANCE OF NH_3 AND PHASE OF NH_X ($NH_3 + NH_4^+$)

Figure 2.1 displays NH_3 mixing ratios along the flight tracks for each sampled city, which includes all low/no smoke flight segments for the example/representative flights. Over LA, during low/no smoke conditions the highest NH_3 mixing ratios were usually observed east of the city, while the lowest mixing ratios were observed in the westernmost region of the city, closest to the ocean. Winds during this flight segment were from the west and west-southwest, thus the westernmost flight segments in the figure represent on-shore flow and the easternmost portions of this flight were collected downwind of the urban emissions. Over NYC under low/no smoke conditions, the highest NH_3 mixing ratios were observed over the city proper, while the lowest mixing ratios were observed over Long Island Sound. Winds over NYC during the flights were southeasterly (0.1 – 9.1 m s^{-1}) on 16 August. In Chicago, on 12 August, under low/no smoke conditions, the highest NH_3 was observed immediately downwind (i.e., south) of the city. Toronto was also a focus city of the AEROMMA field campaign, however, both Toronto flights (4 and 5 August) were smoke-impacted and therefore not utilized for further analysis. An example flight track for Toronto can be found in Figure B1.

Figure 3.1 displays boxplots of NH_3 mixing ratios in the boundary layer for flight segments over and downwind of each urban area for each individual flight. The regions included in these plots are shown in Figure 2.1. Under low/no smoke conditions the highest average NH_3 mixing ratio was observed over LA (4.7 ± 3.7 ppb) on 23 August, while the lowest average mixing ratio was observed in NYC (0.8 ± 0.4/0.5 ppb) on 09 and 16 August. There is no significant difference

between average smoke-impacted and low/no smoke NH_3 mixing ratios in NYC and Chicago (Figure B3).

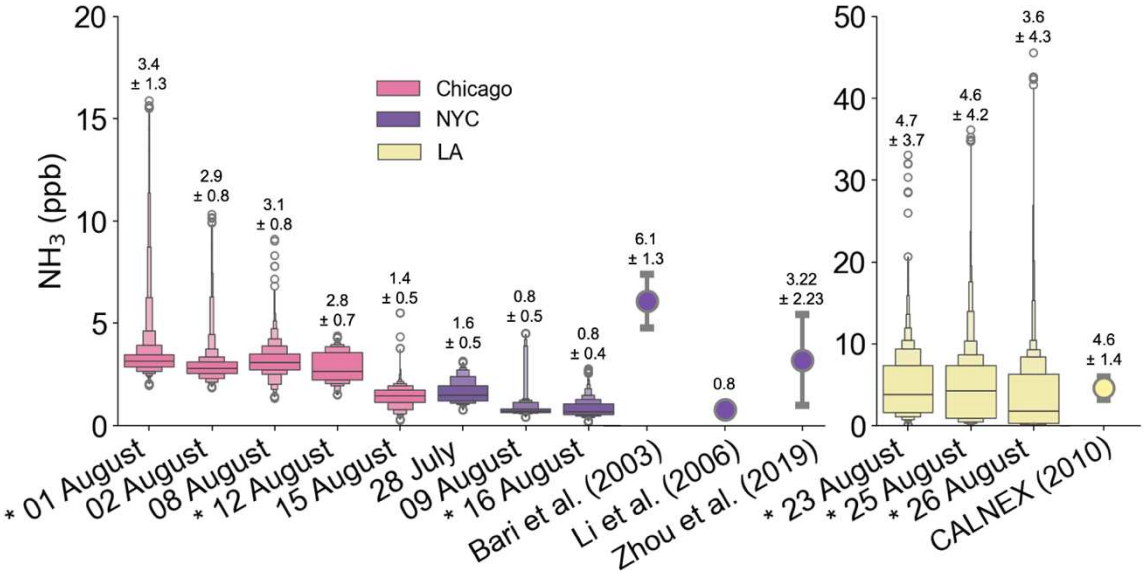

Figure 3.1: Boxplots of NH_3 observed over LA, NYC, and Chicago. Each boxplot includes data from one flight, segmented as described in Section 2.1. The large box in the center of each boxplot represents the median (middle line) and the fourths on each side of the median. The following smaller boxes represent eighths, sixteenths, etc. The numbers above each boxplot represent the mean NH_3 mixing ratio and the 1-sigma standard deviation. Dates with an asterisk indicate that this study uses the flight for further analysis. Singular points represent previous studies with their presented variability.

Wildfires have been shown to be a significant source of NH_3 (Bouwman et al., 1997; Paulot et al., 2014). However, NH_3 mixing ratios have been shown to decrease as smoke plumes age (median e-folding loss with respect to particle-phase partitioning = 55 min) through both dilution and chemistry (Lindaas et al., 2021). The smoke impacting Chicago and NYC was hundreds of miles from the respective source fires and > 2 days old based on NOAA HYSPLIT back trajectories (Figure B4) (Stein et al., 2015). Due to the smoke being aged, there was likely a relatively low amount of remaining gas phase NH_3 (likely due to partitioning to the aerosol phase), explaining

why we did not observe a significant increase in average NH_3 over Chicago and NYC under smoke-impacted conditions compared to low/no smoke conditions.

Urban NH_3 measurements are relatively rare in North America, though there are a few field measurements to compare to (Figure 3.1). We acknowledge that previously reported measurements were taken in different seasons and time periods, so they may not be a direct comparison. Also, the AEROMMA measurements represent a shorter measurement period (i.e., a few days of flights) versus longer term observations at the ground. Generally, we observed lower or equivalent average mixing ratios during AEROMMA. NH_3 was measured on the NOAA WP-3D aircraft during the CalNex 2010 field campaign from May–June 2010 in the California South Coast Air Basin. Average NH_3 mixing ratios from the urban LA region during CalNex were 4.6 ± 1.4 ppb (Nowak et al., 2012). Zhou et al. (2019) measured NH_3 at Queens College in NYC from April 2016–October 2017 and found the average NH_3 concentration to be 3.2 ± 2.2 ppb. Bari et al. (2003) measured NH_3 in Manhattan between July and September 1999 and observed an average NH_3 mixing ratio of 6.1 ± 1.3 ppb. Li et al. (2006) found that the average NH_3 was 0.8 ppb at Queens College during winter 2004. Average NH_x mixing ratios for each AEROMMA flight calculated with the PILS NH_4^+ ranged from 1.4 ± 0.14 - 3.4 ± 0.34 in Chicago, 0.87 ± 0.09 - 1.9 ± 0.19 in NYC, and 4.2 ± 0.42 ppb - 5.7 ± 0.57 ppb in LA. Average NH_x mixing ratios for each AEROMMA flight calculated with the AMS NH_4^+ ranged from 2.1 ± 0.82 - 5.0 ± 1.7 in Chicago, 1.4 ± 0.48 - 2.5 ± 0.85 in NYC, and 5.3 ± 1.8 - 11.2 ± 3.8 in LA.

The NH_3 mixing ratios observed during AEROMMA in NYC are lower than previously reported values. There are several likely explanations. 1) The AEROMMA measurements were airborne and thus collected farther (both vertically and horizontally) from surface sources. 2) AEROMMA measurements were collected during the summertime under well-developed

boundary layers, thus they represent periods with more vertical mixing than observations that were collected during other seasons. 3) AEROMMA conducted research flights during the day, largely in the afternoon, and in the PBL (i.e., below 2000 ft). 4) The sampling windows are also much shorter than other studies and thus only represent snapshots of each urban area. This is consistent with the AEROMMA LA averages, which agrees with the CalNex LA average, which were also aircraft observations.

Figure 3.2 shows boxplots of the NH_3:NH_x ratio, demonstrating the fraction of total NH_3 in the gas-phase, for all low/no smoke flights and the 01 August smoke-impacted flight over Chicago. The fraction of NH_x in the gas phase differed if the particulate NH_4^+ was quantified with the AMS (uncertainty = ± 34%) versus the PILS (uncertainty = ± 10%). Overall, the AMS reported higher concentrations of NH_4^+ than the PILS. However, we are not certain as to why the two measurements do not agree and present both to represent the full range of possible partitioning. While the magnitudes of the measurements are different measurements usually track well and tend to capture similar features (Figure B5). During all flights, NH_x was in both the gas and particle phases. For the flights over Chicago and LA, both the PILS and AMS NH_4^+ data indicate that most of the observed NH_x was in the gas-phase. The PILS data collected over NYC also indicates that most of the observed NH_x was in the gas-phase. However, the AMS data indicates substantially more NH_x in the particle phase. Both the AMS and PILS data for the 16 August flight in NYC show relatively more NH_x in the particle-phase compared to the other flights. This may be due to the 16 August flight having higher relative humidity (74–100%) and slightly colder temperatures (17–22°C) compared to the other flights (RH ranging from 3–80% & temperature ranging from 18–30°C) (Figure B6). There was no clear relationship between smoke-impact and the NH_3:NH_x ratio (Figure B7). Due to the overall favoring of gas-phase NH_x during the relatively warm daytime

conditions (i.e., temperatures >17°C) characterized by the AEROMMA sampling periods, the discrepancy between the PILS and AMS, and the common use of NH_3 in prior studies of urban roadside measurements, we first present NH_3 when examining NH_3 with respect to other species. Then all analysis is repeated for NH_x calculated with both the PILS and AMS measurements to present the range of possible partitioning. These latter values are presented throughout the main text and also summarized in Table B1.

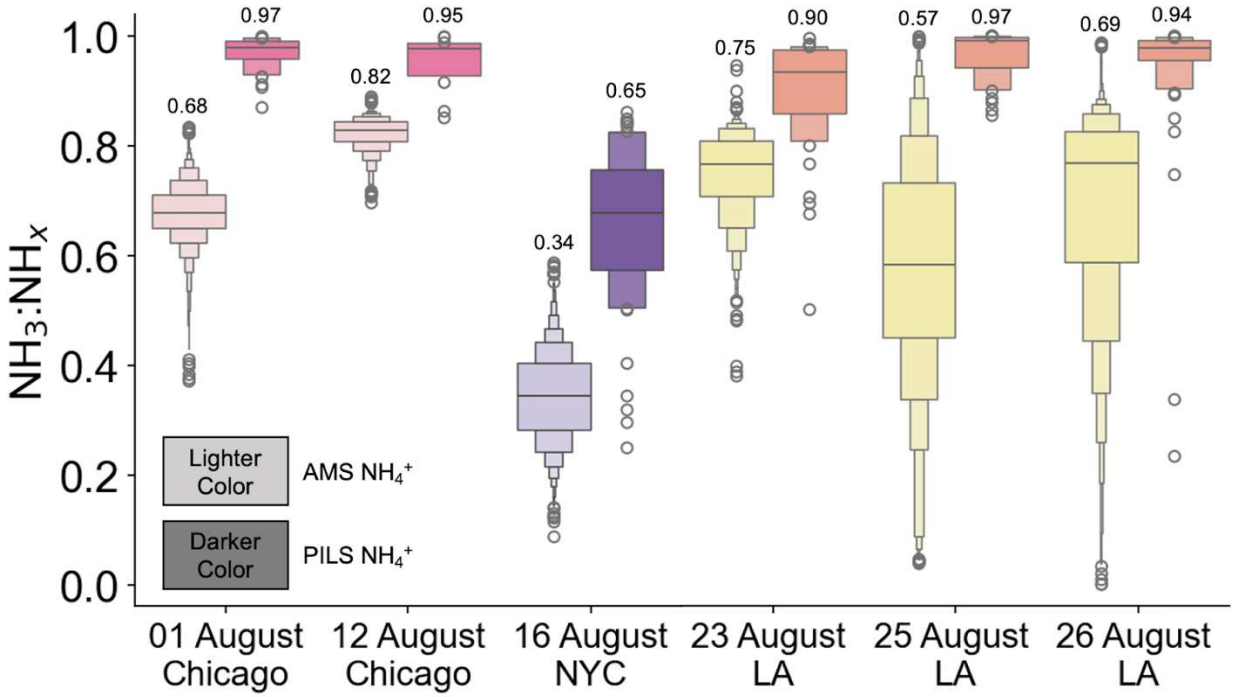

Figure 3.2: Boxplots of the boundary layer NH_3:NH_x ratio for LA, NYC, and Chicago flights used for this analysis. The lighter color boxplots in each pair (left) represent NH_4^+ data from the AMS and the darker color boxplots in each pair (right) represent NH_4^+ data from the PILS. The numbers above each boxplot represent the mean NH_3:NH_x ratio. A NH_3:NH_x ratio close to zero indicates that a majority of the NH_x is in the particle-phase (NH_4), while a NH_3:NH_x ratio close to one indicates that a majority of the NH_x is in the gas-phase (NH_3).

3.2 Urban Tracer Ratios and Source Attribution

Here, we utilize enhancement ratios of NH_3 to various urban tracers to constrain NH_3 to co-located pollutants. CO, NO_x, NO_y, toluene, and ethyne are effective tracers for constraining

urban NH_3 emissions from vehicles because they are primarily emitted from combustion and fuel-related processes, making them strong indicators of vehicular activity (Bishop et al., 2010; Boynard et al., 2014; Sun et al., 2014). By leveraging these tracers, we can better isolate vehicular NH_3 emissions from other sources, such as agriculture. We also report more conserved NH_x enhancement ratios to account for differences in mixing and partitioning between flights and cities. We also compare our calculated enhancement ratios to previously reported ratios. For this analysis, we focus on low/no smoke flights (to mitigate the impact of smoke on all analyzed species) as well as flight segments with high NH_3 for attribution.

3.2.1 New York City

Figure 3.2 shows (a) NH_3 versus CO colored by toluene, (b) NH_3 versus ethyne, (c) NH_3 versus NO_x, and (d) NO_y for the 16 August 2023 flight over NYC (Figure 2.1 flight track). This was the only flight over NYC that was classified as low/no smoke and was chosen for this analysis in order to investigate urban NH_3 abundances relative to other urban tracers. NH_3 is strongly correlated with CO ($r^2 = 0.83$), and ethyne ($r^2 = 0.93$) in NYC under low/no smoke conditions. Thus, NH_3 is correlated with tracers frequently associated with vehicle emissions (Brito et al., 2018). Observations collected immediately downwind of the Northport Power Station (40.92278°N 73.34278°W), which burns both natural gas and conventional oil, have been removed from these figures and this facility is not a strong source of NH_3 (mixing ratios of ~2 ppb were observed) but is a strong source of CO (mixing ratios of up to ~10 ppm were observed) (Figure B8). In the NYC region, there are two observed NH_3:NO_x and NH_3:NO_y relationships. The lower ratio being directly overhead of the city and the higher ratio being north of the city (Figure B9). The NH_3 to NO_y correlations reflect both emissions, thermodynamics, and the high uncertainty regarding sampling particulate NO_3^- in the NO_y instrument. The corresponding ΔNH_x:Δtracer

ratios are ΔNH_x:ΔCO (PILS: 0.020 ± 0.004; r^2 = 0.65, AMS: 0.043 ± 0.001; r^2 = 0.92), ΔNH_x:ΔNO_x (PILS: 0.257 ± 0.075; r^2 = 0.66, AMS: 0.472 ± 0.143; r^2 = 0.85), and ΔNH_x:ΔNO_y (PILS: 0.115 ± 0.024; r^2 = 0.76, AMS: 0.269 ± 0.006; r^2 = 0.92).

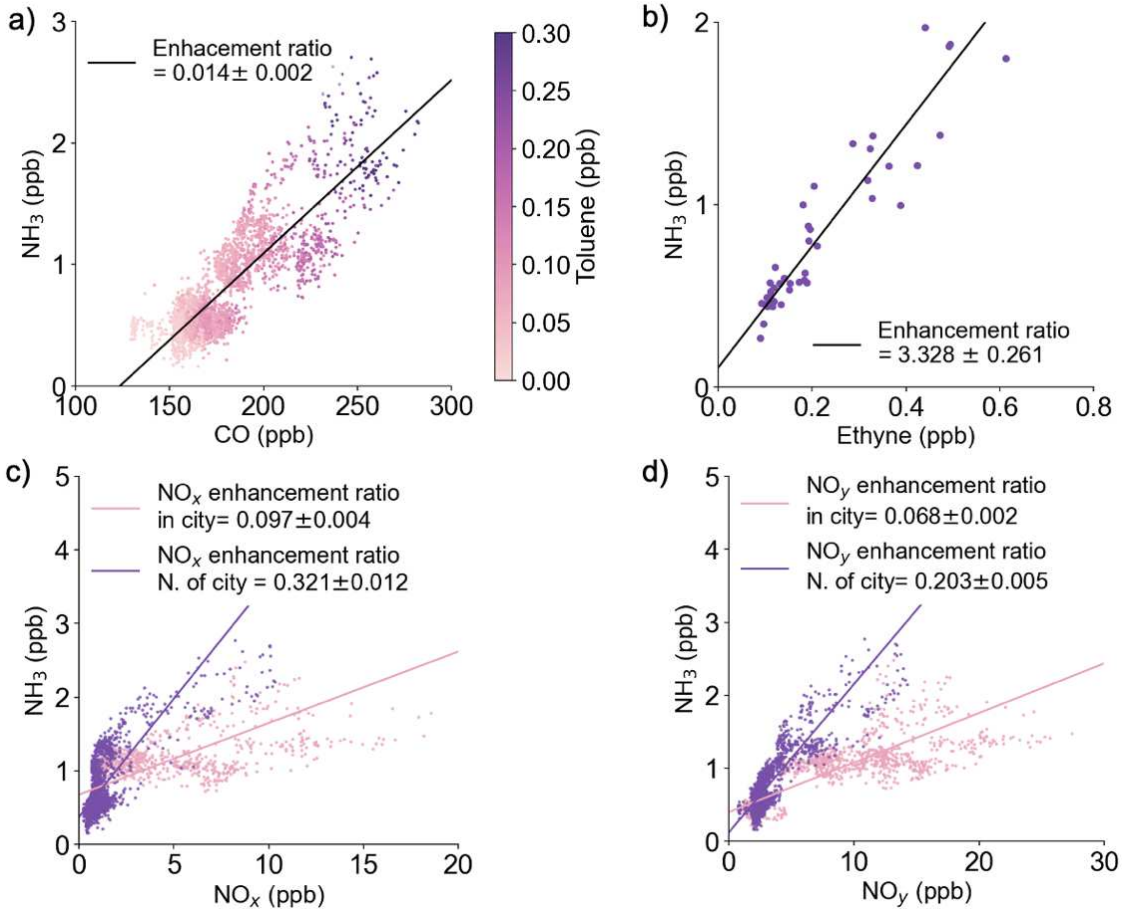

Figure 3.3: Scatter plots of NH_3 versus a) CO, b) ethyne, c) NO_x, and b) NO_y for NYC on 16 August 2023 with the best-fit line. NH_3:tracer ratios were calculated using RMA regression.

3.2.2 Los Angeles

A strong relationship between NH_3 and CO was consistently observed across all the AEROMMA flights over LA (Figure 3.4). Figure 3.4 shows the ΔNH_3:ΔCO, ΔNH_3:Δethyne, ΔNH_3:ΔNO_x, and ΔNH_3:ΔNO_y ratios for each of the three LA flights produced using RMA regression. NH_3 is strongly correlated with CO (r^2 = 0.90–0.97) and ethyne (r^2 = 0.74–0.94) over

LA during all three flights. The strong relationships between NH_3, CO, and ethyne again demonstrate that NH_3 is correlated with tracers frequently associated with vehicle emissions (Brito et al., 2016). NH_3 is also strongly correlated with NO_x (r^2 = 0.75–0.80) within the datasets from each research flight. The corresponding ΔNH_x:Δtracer ratios for the average of the three LA flights are ΔNH_x:ΔCO (PILS: 0.038 ± 0.002; r^2 = 0.93, AMS: 0.046 ± 0.001; r^2 = 0.85), ΔNH_x:ΔNO_x (PILS: 0.936 ± 0.172; r^2 = 0.77, AMS: 1.19 ± 0.030; r^2 = 0.67), and ΔNH_x:ΔNO_y (PILS: 0.51 ± 0.084; r^2 = 0.81, AMS: 0.687 ± 0.011; r^2 =0.86).

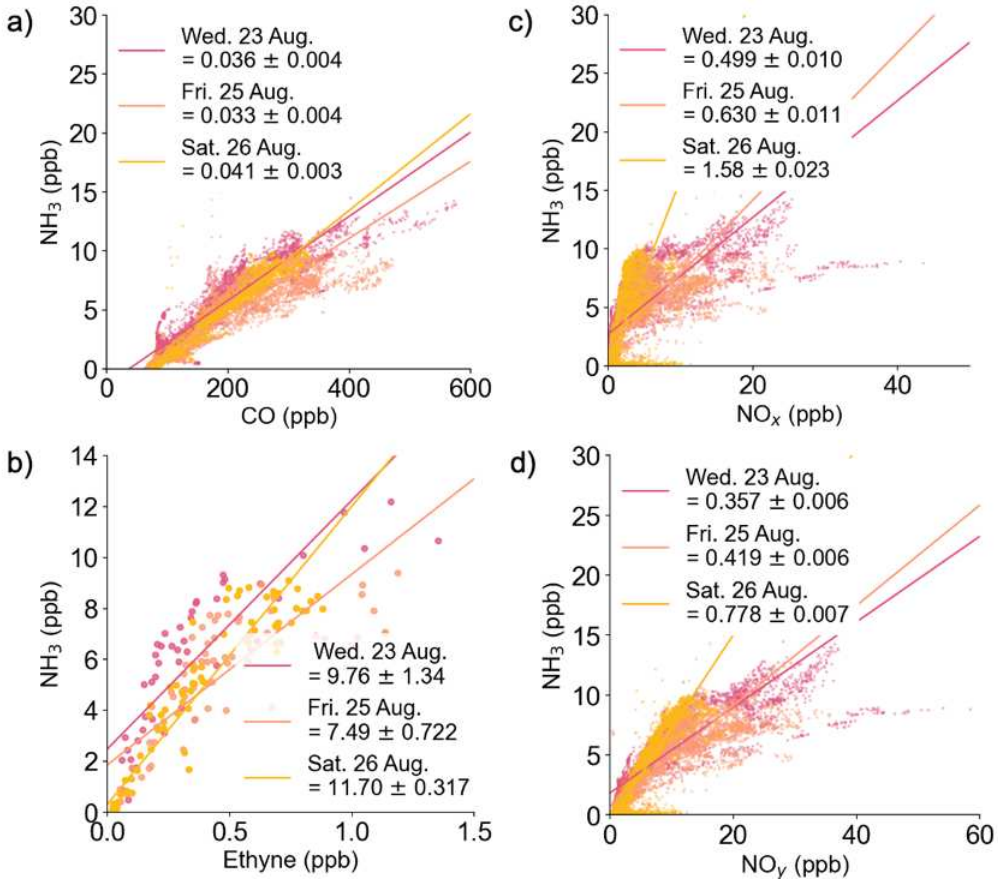

Figure 3.4: Scatter plots of NH_3 versus a) CO, b) ethyne, c) NO_x, and d) NO_y colored by each LA flight with the RMA best-fit line for each of the three LA flights (23 August: Pink, 25 August: Orange, and 26 August: Yellow).

ΔNH_3:ΔNO_x increased between 2008 and 2018 based on roadside measurements beside a highway on-ramp LA (Bishop, 2019). While the Bishop (2019) dataset observed decreasing mixing ratios of roadside NH_3, (18% decrease from 2008 to 2018), NO_x was observed to have a larger decrease in roadside mixing ratios (57% decrease from 2008 to 2018), explaining the increasing trend in ΔNH_3:ΔNO_x over time. The AEROMMA ΔNH_3:ΔNO_x is consistent with this trend (Figure B10). We acknowledge that roadside measurements are different from aircraft measurements since there is no aging/little partitioning of NH_3 to the particle-phase. The PILS (0.936 ± 0.172) and AMS (1.19 ± 0.030) ΔNH_x:ΔNO_x ratios are also consistent with the increasing trend observed in Bishop (2019). However, the flight on 26 August encountered higher ΔNH_3:ΔCO, $\Delta NO_{x/y}$, and Δethyne ratios compared to the flights on 23 August and 25 August. This flight was hotter and drier than the other two flights (Figure B6), suggesting that NH_4NO_3 formation may have been less favorable on 26 August compared to the other two flights (Bassett & Seinfeld, 1983; Kim et al., 1993; Russell et al., 1983). The 26 August flight was also a weekend flight (Saturday) (i.e., less traffic) while the 23 August (Wednesday) and 25 August (Friday) flights were weekday flights. All three flights occurred during the afternoon/evening and under westerly wind conditions (0.1–9.8 m s^{-1}). The westerly wind conditions facilitated the sampling of urban air while avoiding the sampling of agriculturally influenced air masses from the dairies east of LA (Nowak et al., 2012).

Multivariate linear regression (MLR) also confirms that NH_3 was primarily associated with CO (i.e, combustion source; average fractional contribution 57 - 86%) opposed to CH_4 (i.e., agriculture source; average fractional contribution 0 - 17%) during each LA flight (Figure B11). However, there was still an urban signature (average fractional contribution ranging from 1 - 26%) present that was not associated with CO or CH_4. During the 23 and 25 August flights, there was a

large spike in NH_3 not associated with CO or CH_4 in the MLR near a natural gas-fired power plant and a river that was associated with a spike in NO_y. During the 26 August flights, there was a large spike in NH_3 not associated with CO or CH_4 in the MLR near an industrial complex that was associated with a spike in NO_y and N_2O.

3.2.3 CHICAGO

We use two different flights over Chicago to investigate the relationship between NH_3 and urban tracers. The first flight on 01 August was chosen for analysis despite being classified as smoke-impacted because there was a very dilute, well-mixed plume where the urban enhancement was clearly separable. The southwesterly winds (4.5 m/s on average) facilitated sampling urban outflow over Lake Michigan with the AEROMMA flight pattern. NH_3 had no correlation with CH_3CN throughout the flight as the smoke was well mixed and aged (Figure B12). A strong relationship between NH_3 and CO was only observed when the aircraft was positioned downwind of the urban area; thus, the aged smoke was not a large source of NH_3. Figure 3.5 shows a map of Chicago with flight transects defined as upwind of the city, directly over the city, and downwind of the city). The strongest correlations between NH_3 and CO ($r^2 = 0.69$), NH_3 and NO_x ($r^2 = 0.60$), and NH_3 and NO_y ($r^2 = 0.63$) were observed in the downwind leg when the urban plume would have been ~ 3 hours old based on the wind speed. We acknowledge that NH_3 may have been lost over the lake due to both partitioning and dry deposition processes. The higher relative humidity over the lake (65% compared to 60% over land) could have enhanced partitioning to the particle phase (Bassett & Seinfeld, 1983; Kim et al., 1993). Additionally, the lower surface resistance over water could have facilitated dry deposition (Ma & Daggupaty, 2000; Williams, 1982). Together, these processes may have reduced NH_3 concentrations and lowered the ΔNH_3:Δtracer enhancement ratios observed on the downwind leg. The highest NH_3 mixing ratios were observed

over the city of Chicago in two distinct locations. The first section of the flight with high NH_3 mixing ratios also had low CO mixing ratios (points in the black circle in Figure 3.5c–e). The source of the high NH_3 mixing ratios in this section of the flight is unknown. The second section of the flight with elevated NH_3 mixing ratios was correlated with higher CO and was over a highway (points in the grey circle in Figure 3.5c–-e). The ΔNH_3:ΔCO ratio for this segment is 0.153 ± 0.001. The corresponding ΔNH_x:Δtracer ratios for the downwind leg are ΔNH_x:ΔCO (AMS: 0.069 ± 0.002; r^2 = 0.75), ΔNH_x:ΔNO_x (AMS: 0.357 ± 0.028; r^2 = 0.57), and ΔNH_x:ΔNO_y (AMS: 0.297 ± 0.158; r^2 = 0.65). Note there are no ratios available with the PILS data in this case as there were too few data points.

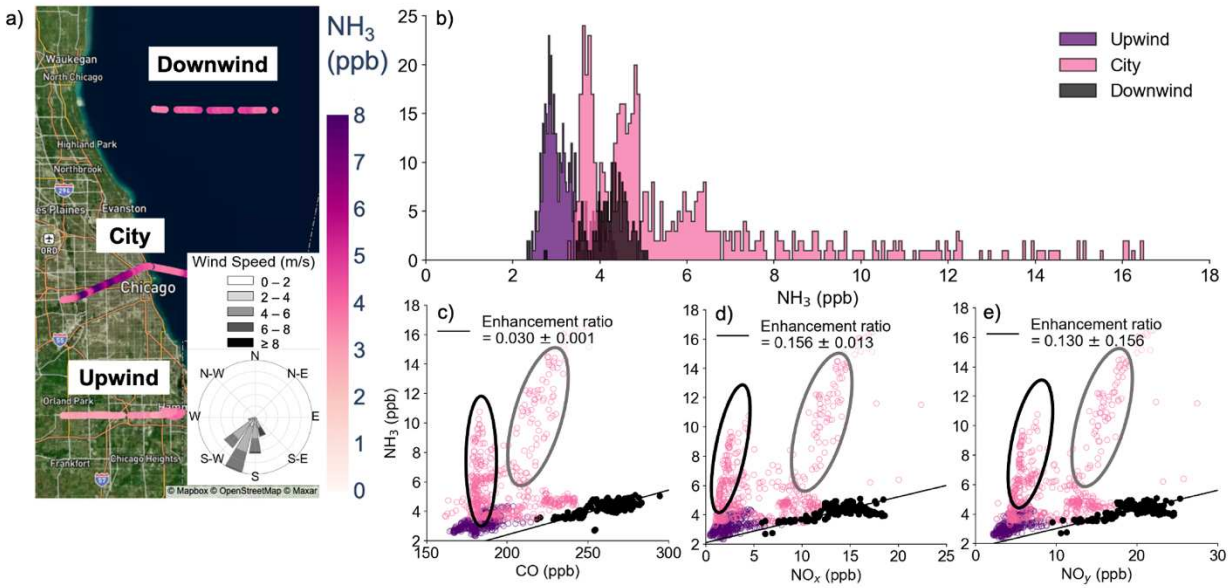

Figure 3.5: Data for the 01 August 2023 Chicago flight. a) Map of the location of upwind, city, and downwind legs of the flight, colored by NH_3, b) histograms of NH_3 colored by legs, c) scatter plot of NH_3 v. CO, d) scatter plot of NH_3 v. NO_x, e) scatter plot of NH_3 v. NO_y colored by sector. (c-e) The black circle represents points downwind of a golf course and the grey circle represents points downwind of a highway (blue bar in Figure 3.7).

A relationship between NH_3 and urban tracers was observed during the 12 August AEROMMA low/no smoke flight. This flight was less optimal than the 01 August flight for

examining the urban outflow as the northerly winds (5.2 m/s on average) did not facilitate the sampling of a clear urban plume as the sampled plume was not the direct outflow from the urban area and instead traveled over other industries south of Chicago (e.g., steel mills, agriculture) before it was sampled. Figure 3.6 shows a map of Chicago with flight transects defined as upwind of the city, directly over the city, immediately downwind of the city (downwind leg 1), and further downwind of the city (downwind leg 2). The highest average NH_3 was observed during the first downwind leg. However, despite the high NH_3 plume in the downwind leg 1 transect, the ΔNH_3:Δtracer correlations were weak throughout this leg (ΔNH_3:ΔCO; $r^2 = 0.24$, ΔNH_3:ΔNO_x; $r^2 = 0.44$, ΔNH_3:ΔNO_y; $r^2 = 0.39$) and the strongest correlations between NH_3 and CO ($r^2 = 0.83$), NH_3 and NO_x ($r^2 = 0.73$), and NH_3 and NO_y ($r^2 = 0.82$) were observed in the second downwind leg when the urban plume would have been transported ~4 hrs from the city center. There was also a strong correlation ($r^2 = 0.92$) between NH_3 and CH_4 in the second downwind leg, indicating that this leg may not be an urban plume. The corresponding ΔNH_x:Δtracer ratios for the downwind leg 2 are ΔNH_x:ΔCO (AMS: 0.030 ± 0.004; $r^2 = 0.94$), ΔNH_x:ΔNO_x (AMS: 0.774 ± 0.094; $r^2 = 0.89$), and ΔNH_x:ΔNO_y (AMS: 0.188 ± 0.028; $r^2 = 0.95$). Note there are no PILS ratios as there were too few data points. Compared to LA and NYC, both Chicago flights have a higher background NH_3 mixing ratio (~2 ppb compared to ~0 ppb in LA and ~0.5 ppb in NYC). This may be due to agricultural regions surrounding the city of Chicago and therefore, being located upwind of Chicago during both the 01 August and 12 August flights.

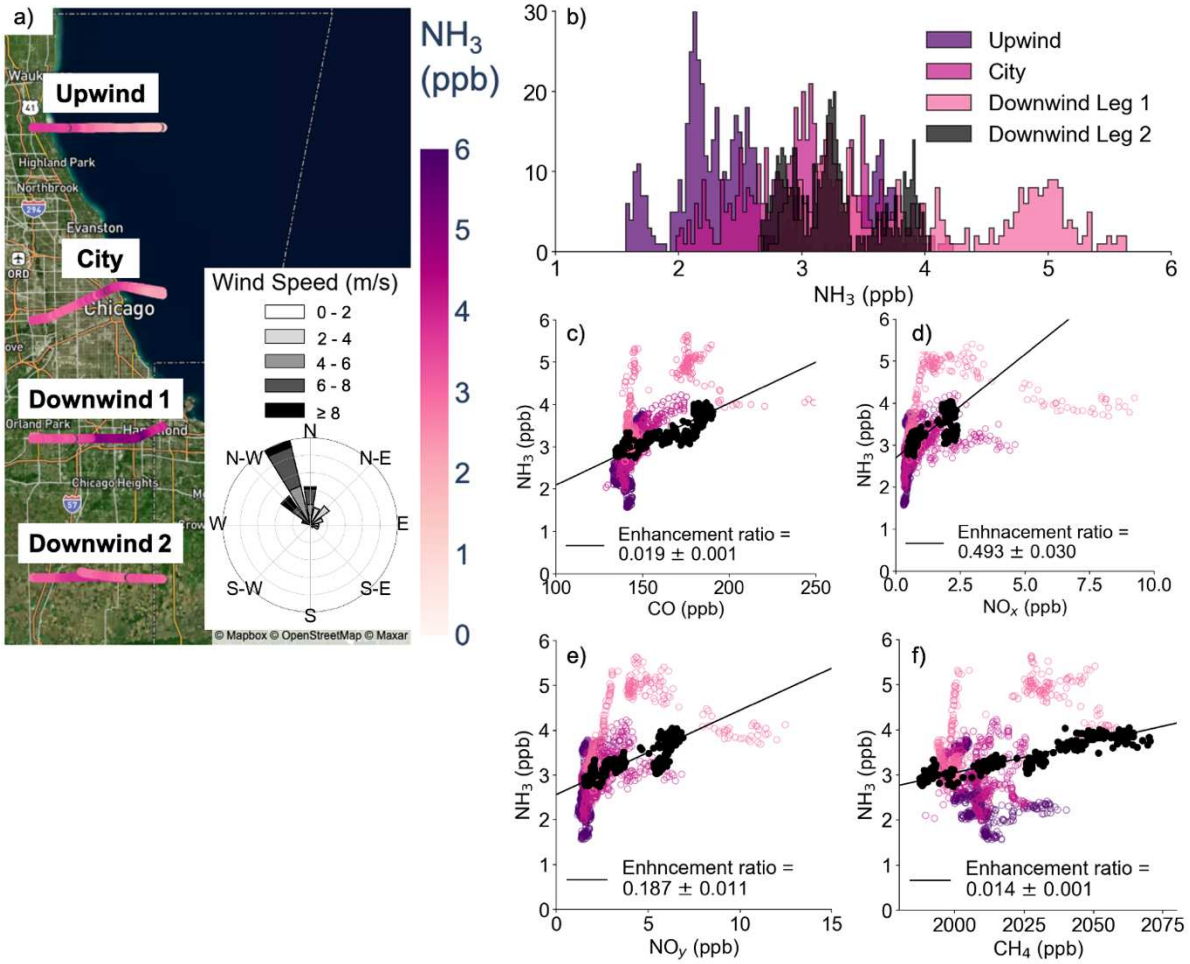

Figure 3.6: Data for the 12 August 2023 Chicago flight. a) Map of the location of upwind, city, and downwind legs of the flight, colored by NH_3, b) histograms of NH_3 colored by legs, c) scatter plot of NH_3 v. CO, d) scatter plot of NH_3 v.NO_x, e) scatter plot of NH_3 v. NO_y colored by sector, and f) NH_3 v. CH_4 colored by sector. Fits are to the correlations from the Downwind Leg 2 segment.

3.3 Comparison to Previous Studies

Figure 3.7 summarizes $\Delta NH_{3/x}$:ΔCO ratios from this study, previous observational studies, and inventories for each of the sampled cities in order to facilitate comparison between the various locations and studies. Studies and inventories that are included in Figure 3.7 are those that reported both NH_3 and CO measurements in the cities studied in this analysis. Figure 3.7 shows that AEROMMA ΔNH_3:ΔCO ratios are both higher and lower than previously reported ratios. In Chicago and LA, the AEROMMA ΔNH_3:ΔCO is higher than the EPA NEI on-road vehicle

estimate (i.e., the NEI estimate is below the confidence interval), whereas the AEROMMA ratio in NYC is consistent with the EPA NEI on-road vehicle estimate. However, the NEI estimated ΔNH_3:ΔCO is lower than the more conservative AEROMMA ΔNH_x:ΔCO ratios for all three cities. This indicates that NH_3 emissions are likely underestimated in the NEI as the 2020 NEI utilized an older version of the Motor Vehicle Emission Simulator (MOVES) model that underestimated NH_3 emissions from vehicles (Toro et al., 2024). We acknowledge that other combustion sources in urban areas co-emit NH_3 and CO. However, since the AEROMMA NH_3 observations are strongly correlated with vehicular emissions tracers, we compare the AEROMMA $\Delta NH_{3/x}$:ΔCO ratios to the NEI estimated ΔNH_3:ΔCO ratio for on-road vehicles. In Chicago and LA, the AEROMMA ΔNH_3:ΔCO and ΔNH_x:ΔCO ratios are lower than the Fuel Efficiency Automobile Test (FEAT) ratios from each respective city (Bishop, 2010, 2019, 2021; Bishop & Stedman, 2015). The FEAT measurements were all on-road studies and closer to vehicular NH_3 sources than AEROMMA, which may have led to higher NH_3 values than observed during AEROMMA. However, the AEROMMA ratio observed over the highway on 01 August is higher than all the FEAT ratios from Chicago. The LA AEROMMA ΔNH_3:ΔCO ratio is consistent with the ratios found in Nowak et al. (2012) and Sun et al. (2014). The measurements from Nowak et al. (2012) were collected during the 2010 CalNex airborne field campaign while Sun et al. (2014) was a roadside study. AEROMMA ΔNH_x:ΔCO ratios in NYC and Chicago were higher than the AEROMMA ΔNH_3:ΔCO ratios, while in LA, the AEROMMA ΔNH_x:ΔCO ratios were consistent with the AEROMMA ΔNH_3:ΔCO ratio. This is consistent with NYC and Chicago having a larger fraction of NH_x in the particle phase (Figure 3.2). Trends observed in $\Delta NH_{3/x}$:ΔNO_x ratios from AEROMMA, NEI vehicle estimates, and FEAT measurements are generally consistent and agree with the trends observed in ΔNH_x:ΔCO ratios (Figure B13). Overall, the NEI is lower than both

the AEROMMA and FEAT $\Delta NH_{3/x}$:ΔNO_x ratios, once again indicating the NEI is likely underestimating NH_3. The AEROMMA $\Delta NH_{3/x}$:ΔNO_x ratios are also generally lower than the FEAT ratios, as the FEAT measurements were roadside studies.

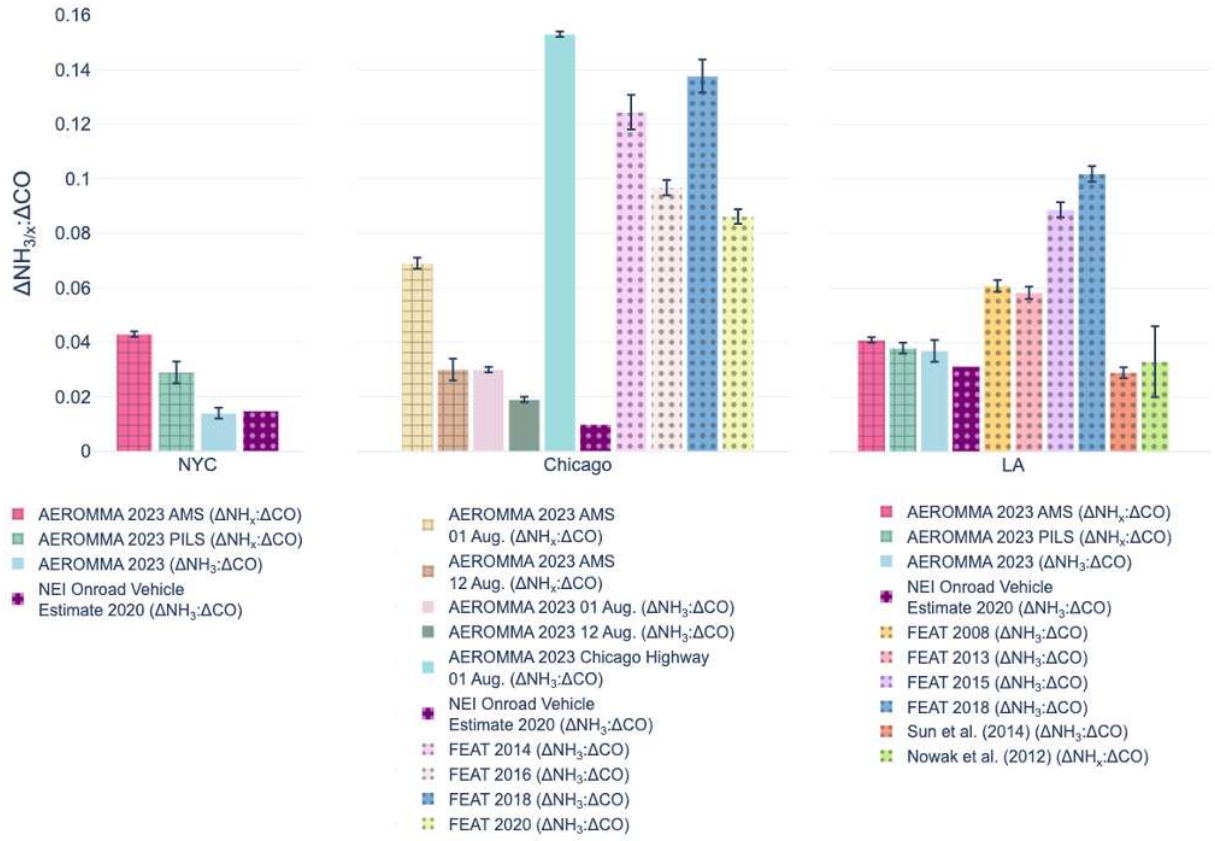

Figure 3.7: Bar chart of various $\Delta NH_{3/x}$:ΔCO ratios. AEROMMA NH_x ratios are denoted by hatched bars, AEROMMA NH_3 ratios are denoted by solid bars, and non-AEROMMA ratios are denoted by dotted bars. Note that the AEROMMA ratios for Chicago were taken from the downwind leg on the 01 August flight and the second downwind leg on the 12 August flight. The AEROMMA 2023 ratios in LA are an average of the three flights.

In LA, previous studies have found vehicles to be a significant source of NH_3. Bishop et al. (2010), a roadside study, found that average NH_3 emissions in LA were 0.79 ± 0.02 g NH_3/kg fuel and accounted for 27% of the molar fixed nitrogen emissions. The most recent FEAT emission factor measurements, measured in 2018, observed that the LA NH_3 emission factor was 0.68 g/kg of fuel (Bishop, 2020). Nowak et al. (2012), an airborne study, estimated that vehicles in the

California South Coast Air Basin (SoCAB) emit 62 ± 24 metric tons of NH_3 per day, similar to that of dairy facilities. Sun et al. (2014) found that the on-road average emission factor in LA was 0.49 ± 0.06 g NH_3/kg fuel and that the emission factor increased in stop-and-go traffic. Using FEAT 2018 LA CO emission factor of 11.0 g CO/kg of fuel and our average LA ΔNH_3:ΔCO ratio of 0.037 ± 0.004, we calculated a NH_3 emission factor 0.24 ± 0.03 g NH_3/kg of fuel burned. Using the more conservative ΔNH_x:ΔCO ratios of 0.038 ± 0.002 (PILS) and 0.046 ± 0.001 (AMS), the calculated NH_x emission factor would be 0.25 ± 0.02 (PILS) and 0.31 ± 0.01 (AMS). Both the calculated NH_3 and NH_x emission factors are lower than the FEAT 2018 measured emission factor for NH_3, likely due to loss of NH_3 due to deposition as the aircraft was sampling at altitude opposed to next to the highway. Cao et al. (2022) used satellite data before and during the COVID-19 lockdown and determined that vehicle NH_3 emissions account for 60–95% of NH_3 emissions in western LA. Following the methods of calculating SoCAB vehicular emissions of NH_3 presented in Nowak et al. (2012), we use the estimated total 2023 CO emissions (1642 metric tons day^{-1}) from the SoCAB as estimated by the California Air Resources Board (CARB) (CARB, 2023) multiplied by the average ΔNH_3:ΔCO ratio from AEROMMA (0.037 ± 0.004) to estimate the automobile NH_3 emissions to be 61 ± 7 metric tons day^{-1}, which is not significantly different from the emission estimate from Nowak et al. (2012).

In Chicago, the FEAT 2020 NH_3 emission factor is 0.57 g/kg fuel burned (G. Bishop, 2021). Using the FEAT 2020 CO emission factor of 10.9 g/kg of fuel burned and the AEROMMA ΔNH_3:ΔCO ratios in Chicago 0.03 ± 0.001 (Downwind on 01 August), 0.019 ± 0.001 (Downwind 2 on 12 August), and 0.153 ± 0.001 (Over the highway on 01 August), we calculated NH_3 emission factors of 0.20 ± 0.01 g/kg of fuel (Downwind on 01 August), 0.13 ± 0.01 g/kg of fuel (Downwind 2 on 12 August), and 1.01 ± 0.01 g/kg of fuel (Over the highway on 01 August). Using the AMS

ΔNH_x:ΔCO ratios for the two downwind segments, we calculated NH_x emission factors of 0.45 ± 0.02 g/kg of fuel (Downwind on 01 August), and 0.20 ± 0.02 g/kg of fuel (Downwind 2 on 12 August). The NH_3 and NH_x emission factors for both the downwind legs were lower than the FEAT 2020 measured emission factors, likely due to the aircraft sampling at altitude. The NH_3 emission factor over the highway was higher than the measured emission factor, indicating that while NH_3 was well correlated with CO during this segment, the NH_3 source may not be only vehicles.

In NYC, previous studies have concluded that NH_3 is likely from traffic sources. Li et al. (2006) measured NH_3 at Queens College in NYC, near two busy highways, and found that spikes in NH_3 were correlated with spikes in CO_2 and often occurred during rush hour, suggesting that traffic exhaust could be a source of NH_3 in NYC. During AEROMMA, NH_3 was well correlated with CO_2 ($r^2 = 0.61$) under low/no smoke conditions. However, we chose to use CO opposed to CO_2 for our enhancement ratios as CO_2 concentrations are relatively high and well-mixed in the atmosphere, which can mask small enhancements near emission sources. In contrast, CO typically shows more distinct enhancements near fresh emissions, allowing for clearer source attribution (Nathan et al., 2018). Zhou et al. (2019) also measured NH_3 at Queens College and found that variations in NH_3 coincided with traffic patterns, as opposed to their finding at rural sites where the NH_3 concentration was related to temperature. While there are no measured FEAT emission rates for NYC, both the LA (11.0 g CO/kg of fuel) and Chicago (10.9 g CO/kg of fuel) FEAT CO emission rates are quite similar, suggesting that this rate may be similar among cities. Because of this, we use a CO emission rate of 11.0 g CO/kg of fuel burned along with the AEROMMA ΔNH_3:ΔCO ratio from NYC (0.014 ± 0.002) to calculate a NH_3 emission rate of 0.09 ± 0.02 g/kg fuel. Using the ΔNH_x:ΔCO ratios of 0.029 ± 0.004 (PILS) and 0.043 ± 0.001 (AMS), the calculated

NH_x emission factor would be 0.19 ± 0.03 (PILS) and 0.28 ± 0.01 (AMS). These numbers are likely an underestimation of the true roadside NH_3 emission factor as the plane was sampling at altitude and the AEROMMA NH_3 emission factors in Chicago and LA were both underestimations of what was measured at roadside.

Outside of the cities included in this study, measurements indicate that vehicle-related NH_3 is a major source in other urban environments worldwide. Reche et al. (2012) found that NH_3 concentrations decreased with increasing distance from highways in Barcelona, Spain. Sun et al. (2017) found that Beijing, China had a comparable vehicular NH_3:CO_2 emission ratio to U.S. cities, while less developed Chinese cities had higher vehicular NH_3:CO_2 emission ratios. Phillips et al. (2019) found that traffic NH_3:CO ratios in Sidney, Australia ranged from 0.018 – 0.022, consistent with what we calculated for NYC and Chicago on 12 August. They also found that inventories underestimated their calculated ratios. These results are consistent with the strong correlations observed during AEROMMA between NH_3 and vehicular emission tracers.

Unlike ground-based roadside studies, the AEROMMA measurements integrate over a wide footprint and sample air masses influenced by multiple sources. CO, while an effective tracer for combustion, can also originate from non-vehicular sources (e.g., power plants, biomass burning), and NH_3 itself may have contributions from non-traffic urban sources (e.g., agriculture, wastewater, and green spaces). Additionally, NH_3 is semi-volatile and subject to rapid gas-particle partitioning, deposition, and dilution, which can lower enhancement ratios compared to near-source values. Despite these limitations, the strong correlations of NH_3 with CO, $NO_{x/y}$, toluene, and ethyne indicate that vehicles are likely the dominant source of NH_3 in the sampled urban environments during summer. The use of additional tracers on board (CH_3CN to identify biomass burning and CH_4 to identify agricultural influence) allows us to minimize the confounding impacts

of non-vehicular sources. While the airborne-derived ratios should not be viewed as standalone emission factors, they provide a robust, independent check on inventory estimates by capturing integrated urban outflow and revealing where inventories may systematically underestimate NH_3 relative to CO. These data complement, rather than replace, surface-based observations by providing a top-down constraint across spatial scales inaccessible to ground networks, especially when multiple tracers are leveraged to separate sources.

3.4 CONCLUSIONS

Here we report on airborne measurements of NH_3 collected as part of the AEROMMA field campaign during summer 2023 over NYC, Chicago, and LA. This is the first-time airborne measurements of NH_3 have been reported over NYC and Chicago. The AEROMMA field campaign occurred during a period with significant wildfire smoke present over North America. We focused on the urban attribution of NH_3 by comparing NH_3 to other urban tracers. We find that:

- During the AEROMMA field campaign, average NH_3 mixing ratios varied between cities. The lowest average NH_3 was observed over NYC (0.8 ± 0.4 ppb), and the highest average NH_3 mixing ratio was observed over LA (4.73 ± 3.74 ppb).
- In NYC and LA, NH_3 was well correlated with CO, $NO_{x/y}$, and ethyne, suggesting that vehicles are the dominant source of NH_3 during the summer months in these locations.
- Within plumes in the urban area and downwind of Chicago, NH_3 was well correlated with CO and $NO_{x/y}$, however, this relationship is not present in the urban area as a whole, unlike NYC and LA.
- In NYC the AEROMMA ΔNH_3:ΔCO ratio is lower than the observed ratios in Chicago and LA and is consistent with the NEI on-road vehicle estimate.

- The observed ΔNH_3:ΔCO and ΔNH_x:ΔCO ratios in Chicago and LA are significantly (94 - 206% for ΔNH_3:ΔCO and 171 - 604% for ΔNH_x:ΔCO) higher than the NEI estimated on-road vehicle ΔNH_3:ΔCO ratio while upwind of known agricultural sources, however, MLR suggests that there is a small agricultural component in LA as well as an unidentified urban source of NH_3.
- Total NH_x partitioning depends on the city and sampling conditions and varies from primarily gas phase to primarily particle phase.

The AEROMMA field campaign considerably increased the amount of NH_3 measurements across urban areas in North America. The AEROMMA dataset allowed for the opportunity to compare NH_3 to various urban tracers. These data were collected under summertime conditions and future work should be done to quantify these relationships in other seasons. Future work should also focus on understanding gas/aerosol partitioning in each city as well as the factors that drive the partitioning.

CHAPTER 4

ASSESSMENT OF GEOS-CHEM REPRESENTATION OF AMMONIA IN NYC AND CHICAGO

4.1 STUDY AREA

Figure 4.1 presents maps of the individual 2023 AEROMMA research flight tracks over a) Chicago and b) New York City, with flight paths colored by date. We ran GEOS-Chem for the time period of these flights and extracted output data along the flight tracks. For the Chicago flights (altitude range: 232 - 2596 m), the flight tracks are variable, as flights were adapted to daily meteorological conditions, particularly prevailing wind direction, in order to sample urban outflow. As a result, Chicago flights collected observations in multiple directions downwind of the city and provided broad horizontal coverage of the metropolitan region and its plume. In contrast, flight tracks over New York City (altitude range: 164 - 3080 m) are similar across dates due to Air Traffic Control (ATC) constraints, resulting in a consistent sampling strategy largely independent of wind direction. Each NYC flight included repeated transects along the Hudson River, and a vertical profile over Trenton, New Jersey, providing systematic sampling of both horizontal and vertical structure. For both cities, GEOS-Chem output was sampled directly along the aircraft flight paths and limited to boundary layer conditions, as identified using the AEROMMA boundary layer flag.

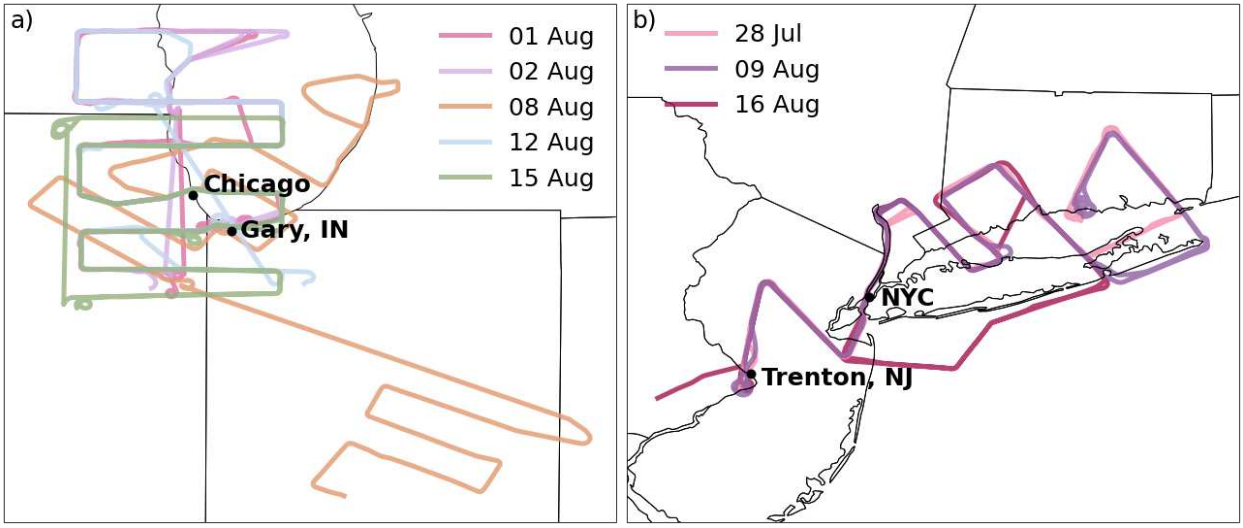

Figure 4.1: Maps of individual 2023 AEROMMA a) Chicago (altitude: 232 - 2596 m) and b) NYC (altitude: 164 - 3080 m) flight tracks colored by date. Wind roses for individual Chicago flights can be found in Figure C1 and wind roses for individual NYC flights can be found in Figure C2. Maps displaying the modeled to observed ratio for various species along the flight tracks can be found in Figure C3 for NYC flights and Figure C4 for Chicago flights.

4.2 AEROMMA OBSERVATIONS INDICATE MISSING EMISSION SOURCES IN NYC REGION

Figure 4.2 shows vertical profiles of observed (black) and GEOS-Chem predicted (colored) NH_3 (a, d, g), NH_4^+ (b, e, h), and NH_x (c, f, i), for the 28 July, 09 August, and 16 August 2023 AEROMMA flights over New York City. Note for this chapter, we present AMS NH_4^+ data as the higher measurement frequency enables us to capture smaller-scale features. We acknowledge that there were discrepancies between the magnitudes of the AMS NH_4^+ and PILS NH_4^+ measurements during AEROMMA (Lill et al., 2025) and that these discrepancies may impact our results. Profiles shown in Figure 4.2 are constructed along the entire flight track displayed in Figure 4.1, with grey shading indicating flights impacted by wildfire smoke, as identified in Chapter 3. Overall, the model reproduces the vertical structure and variability of observed NH_3, NH_4^+, and NH_x reasonably well across all three flights; The 10th - 90th percentile ranges of the model-to-observation ratio are 0.53 - 1.47 for NH_3, 0.21 - 1.31 for NH_4, and 0.44 - 1.25 for NH_x. The

predicted profiles generally capture the presence and altitude of plumes, but often underestimate the magnitudes of the largest observed plumes. Notable discrepancies occur for discrete plumes over Trenton, NJ on 28 July and 09 August (circled in orange), where the model under-predicts observed NH_x enhancements by approximately 5 ppb and 2 ppb, respectively. An even larger underprediction is evident on 16 August, when the model fails to fully reproduce a strong NH_x plume intercepted over downtown NYC (circled in yellow), underestimating observed concentrations by up to 6 ppb. These results indicate that while GEOS-Chem captures the general vertical distribution of reduced nitrogen during NYC flights, it systematically underestimates the intensity of localized urban plumes.

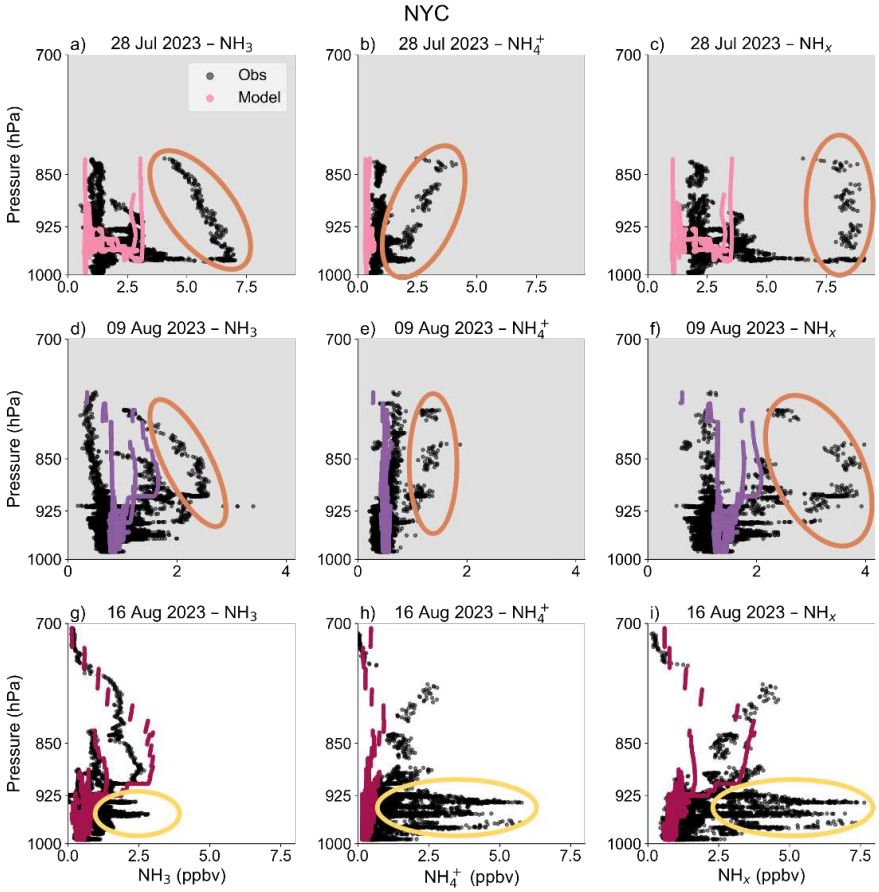

Figure 4.2: Vertical profiles of simulated (colored) and observed (black) NH_3 (a, d, g), NH_4^+ (b, e, h), and NH_x (c, f, i) for the 28 July, 09 August, and 16 August NYC flights. The grey shading indicates a smoke-impacted flight as determined in Chapter 3. Intercepted plumes over Trenton, NJ are circled in orange and an intercepted plume over NYC is circled in yellow. Corresponding time series for each day and species can be found in Figure C5.

Figure 4.3 further investigates the large NH_x enhancement over New York City on 16 August that was substantially under-predicted by GEOS-Chem (circled in yellow in Figure 4.2i). Panel (a) shows the geographic distribution of points included in this missed plume, which are concentrated over and immediately downwind of the NYC urban core. The size of this plume was larger than two GEOS-Chem nested simulation grid boxes. Strong positive correlations are observed between NH_x and CO ($r^2 = 0.81$), as well as between NH_x and key mobile-source tracers including ethyne ($r^2 = 0.78$), NO_x ($r^2 = 0.62$), and toluene ($r^2 = 0.82$). The consistency of these relationships across multiple independent traffic-related tracers indicates that the plume is likely dominated by vehicular emissions. Modeled NH_x is also well correlated with CO ($r^2 = 0.94$), ethyne ($r^2 = 0.92$), NO_x ($r^2 = 0.91$), and toluene ($r^2 = 0.93$). These results are consistent with the conclusions of Chapter 3, which identified traffic as a major contributor to urban NH_3 in NYC during summer conditions. Taken together with the model underestimation shown in Figure 4.2, the strong tracer correlations in Figure 4.3 suggest that mobile-source NH_3 emissions in GEOS-Chem are underestimated, contributing to the model's failure to reproduce the magnitude of this particular urban plume.

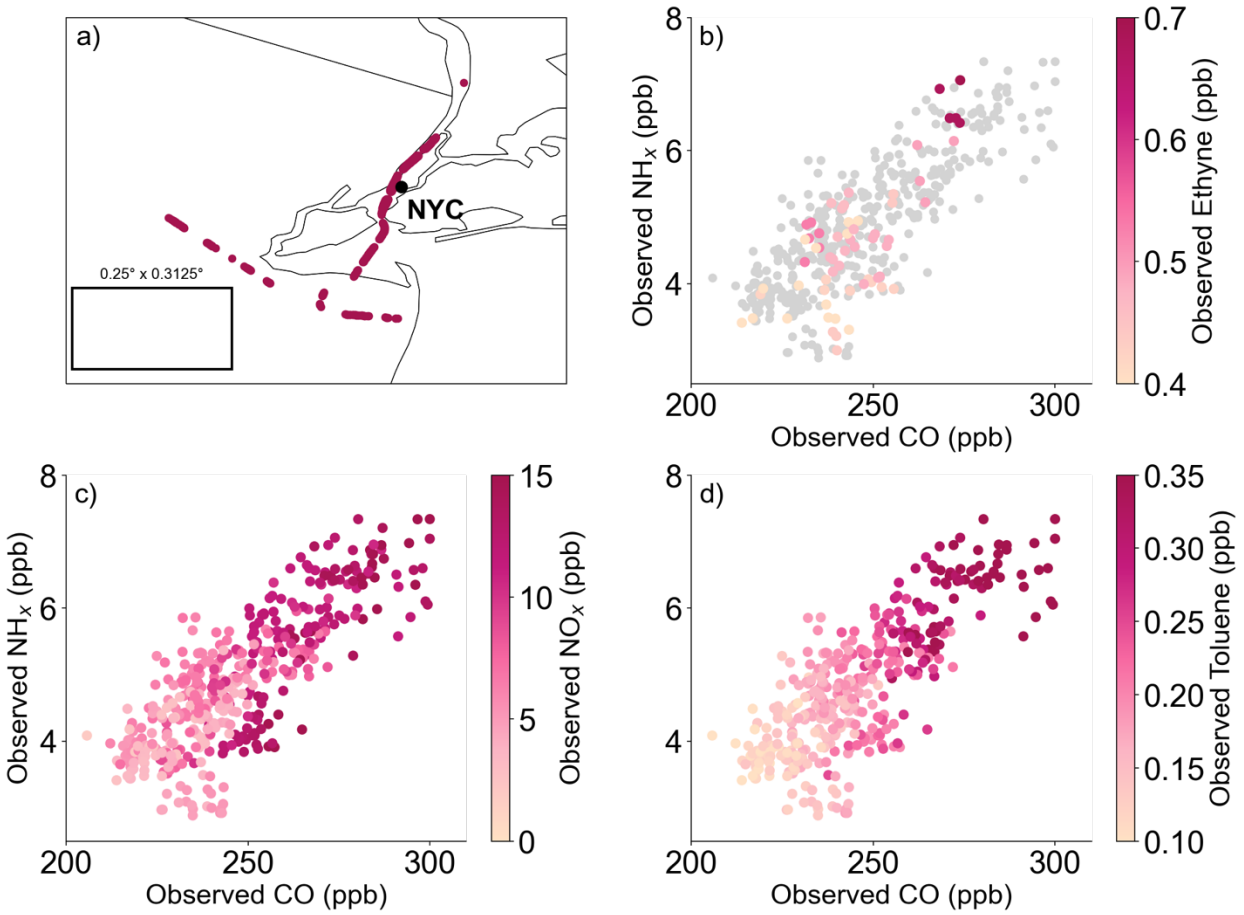

Figure 4.3: a) Map of points included in the missed GEOS-Chem plume circled in yellow in Figure 4.2i with the size of a nested simulation grid box in the bottom left corner. Observed NH_x versus CO on 16 August, colored by observed b) ethyne, c) NO_x, and d) toluene for the points in a).

Figure 4.4 presents vertical profiles from spirals over Trenton, New Jersey on 28 July and 09 August, corresponding to the NH_x plumes highlighted in orange in Figure 4.2. A spiral was also performed over Trenton, NJ on 16 August; however, the winds on 16 August were from the east while the winds on 28 July and 09 August were from the west (Figure C2). This profile can be found in Figure C6 but due to the differing wind direction, is excluded from this comparison. On both days, the observations suggest temporal variability or changing dynamics, with observed NH_x mixing ratios in the late-afternoon profiles approximately 5 ppb higher on 28 July and 1.5 ppb higher on 09 August than those observed earlier in the day throughout much of the boundary layer.

GEOS-Chem fails to reproduce the magnitude of these afternoon enhancements, often predicting profiles that closely resemble the earlier profiles and showing little sensitivity to time of day. The difference between observed and simulated temporal evolution suggests that emissions influencing NH_3 and NH_x near Trenton may increase over the course of the day, or alternatively, they become more efficiently mixed into the boundary layer, processes that are not fully captured in the model. CO is also not well represented in these profiles. While CO does not exhibit the same magnitude of diurnal variability as NH_x, the model generally underestimates observed CO mixing ratios and fails to capture the vertical structure and variability evident in the measurements. The inability of GEOS-Chem to accurately simulate CO alongside NH_x further emphasizes broader limitations in the representation of boundary layer processes and emissions in GEOS-Chem. These results point to limitations in the representation of NH_3 emissions in GEOS-Chem, particularly for mobile or other short-timescale sources that can vary strongly on sub-daily timescales.

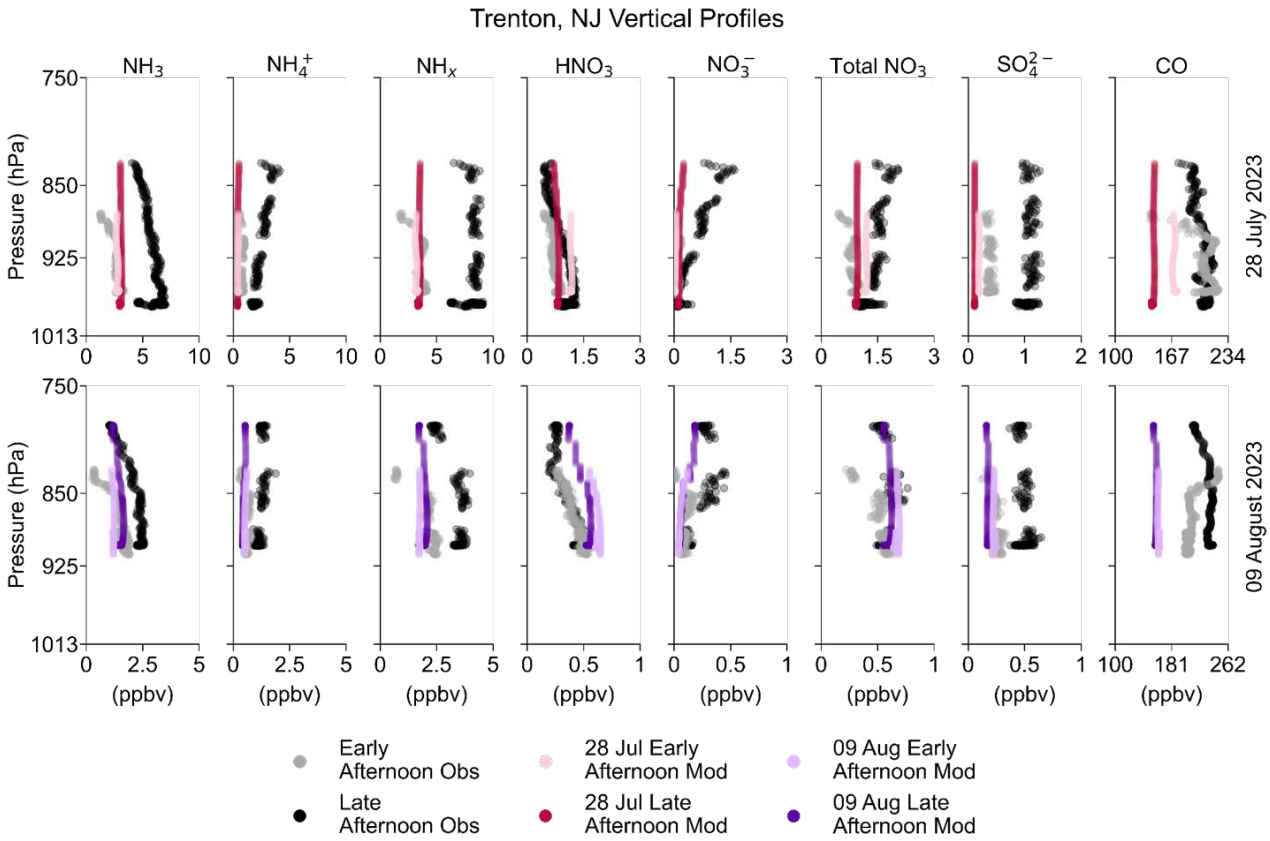

Figure 4.4: Vertical profiles of the spiral over Trenton, NJ on 28 July and 09 August with the first profile of the day plotted in a lighter color (28 July: 13:12 – 13:16 EST & 09 August: 14:56 – 15:00 EST) and the second profile plotted using a darker color (28 July: 16:54 – 16:59 EST & 09 August: 18:47 – 18:52 EST). Observations are in black and model output is colored. These plumes are circled in orange in Figure 4.2. Note that the x-axis is different for the same species on different days.

4.3 AEROMMA OBSERVATIONS INDICATE MISSING EMISSION SOURCES IN CHICAGO REGION

Figure 4.5 shows that the model reproduces the overall vertical structure of observed NH_3, NH_4^+, and NH_x observed during the five Chicago flights, with reasonable agreement in both profile shape and variability. Across all flights, the model performed reasonably well with 10^{th} – 90^{th} percentile model-to-observation ratios of 0.43 – 1.82 for NH_3, 0.40 – 1.35 for NH_4^+, and 0.49 – 1.49 for NH_x. While the model generally captures the observed profile shapes, it frequently underestimates the magnitude of the strongest NH_3 plumes by more than 5 ppb. Several distinct plumes evident in the observations are not reproduced by the model, including an NH_3 plume

downwind of a highway on 01 August (yellow circle) that was previously discussed in Chapter 3.2.3, a plume on 02 August (orange circles) that was in the same location as the plume on 01 August, and a plume on 12 August (red circle) that was a part of the "Downwind 1" segment discussed in Chapter 3.2.2 that had weak relationships with other urban tracers. These missed features demonstrate that the model does not fully represent localized plumes, particularly for sharp, high-concentration NH_3 enhancements.

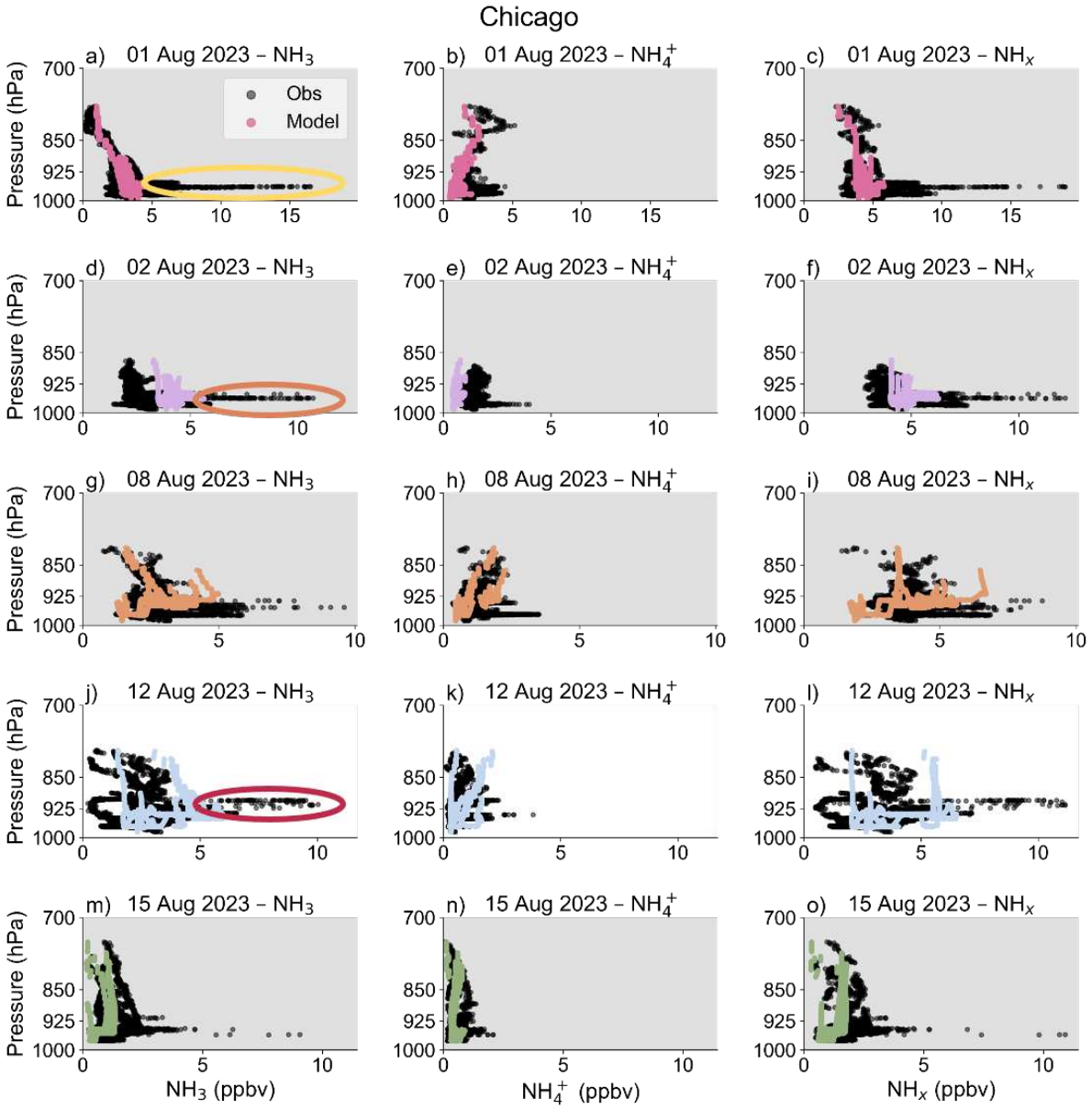

Figure 4.5: Vertical profiles of simulated (colored) and observed (black) NH_3 (a, d, g, j, m), NH_4^+ (b, e, h, k, n), and NH_x (c, f, I, l, o) for the 01 August, 02 August, 08 August, 12 August, and 15 August Chicago flights. The grey shading indicates a smoke-impacted flight as designated in Chapter 3. The yellow circled plume in a) is the elevated NH_3 plume downwind of a highway discussed in Chapter 3.2.2. The orange circled plume in d) is the elevated NH_3 plume discussed in Chapter 3.2.3 is correlated with CO and NO_x. The red circled plume in j) is a section of the downwind 1 plume from Chapter 3.2.3 that has weak relationships with other urban tracers. Corresponding time series for each day and species can be found in Figure C7.

Figure 4.6 presents vertical profiles from the spiral downwind of Gary, IN, on 01 August, which intercepts the lower portion of a smoke plume above ~800 hPa that is further discussed in Chapter 5. Other vertical profiles were conducted near Gary, IN on 02 August, 08 August, and 12 August; however, these profiles were not downwind of Gary, IN due to flight restrictions and differing wind directions (Figure C8). The model reproduces the overall NH_x structure well, with model-observation differences ranging from -2.5 to 1.3 ppb, indicating generally good agreement throughout most of the profile. A notable exception occurs above 850 hPa within the smoke-influenced layer, where the model underestimates NH_4^+ by approximately 3 ppb. This bias is consistent with broader model underestimation of other species in the same layer, including SO_4^{2-} (underestimated by ~4 ppb) and CO (underestimated by ~150 ppb). Together, these discrepancies suggest that the model does not fully capture the chemical or transport characteristics of the intercepted smoke plume, a topic examined in more detail in Chapter 5.

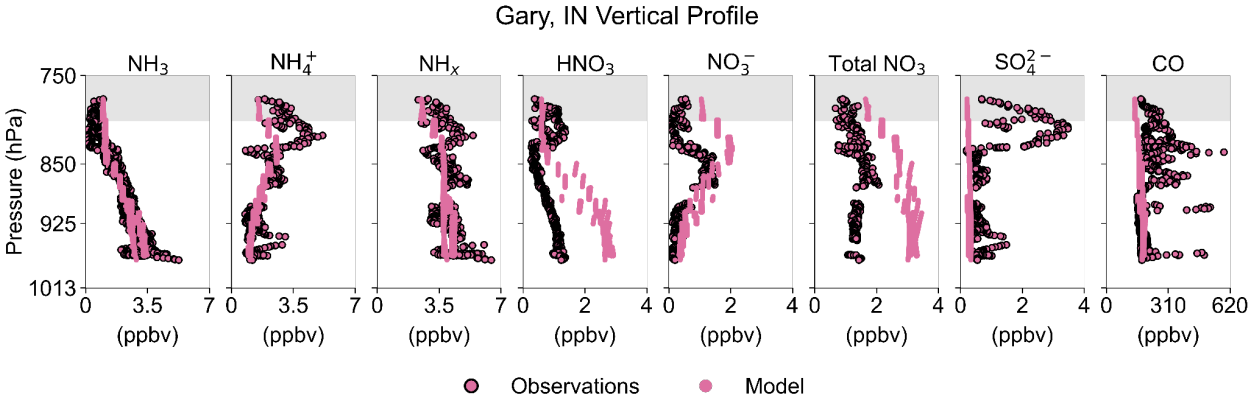

Figure 4.6: Vertical profiles of the spiral downwind of Gary, IN, on 01 August. Observations are plotted with a black circle around the point, while model output is plotted without an outline. The grey shading indicates the bottom of a smoke plume that is further discussed in Chapter 5.

4.5 OBSERVED AND MODELED RELATIONSHIPS BETWEEN MAJOR IONIC SPECIES

Figure 4.7 shows that the model reproduces the overall structure of aerosol partitioning for the NYC flights, but with a systematic low bias in inorganic aerosol, particularly NH_4NO_3. The model does well predicting temperature, suggesting that the underestimation of NH_4NO_3 is not a result of incorrect predictions of temperature (Figure C3). This plotting framework is useful because the axes correspond to aerosol neutralization. SO_4^{2-} requires two NH_4^+ to be fully neutralized, so the 2:1 line represents complete conversion to $(NH_4)_2SO_4$, while points above this line indicate excess NH_4^+ available to form NH_4NO_3. In Figures 4.7 d-f, showing NH_4^+ vs. $(2 \cdot SO_4^{2-} + NO_3^-)$, the 1:1 line represents full charge balance between ammonium and inorganic anions. This allows model-observation differences to be interpreted in terms of aerosol neutralization rather than concentration bias alone. Across all three flights, the model underpredicts NH_4^+ by up to ~ 5 ppb (3.6 μg m^{-3}), SO_4^{2-} by up to ~1 ppb (3.5 μg m^{-3}) and total anions $(2 \cdot SO_4^{2-} + NO_3^-)$ by up to ~5 ppb (14.4 μg m^{-3}). The deviation above the 2:1 line in panel c, which indicates NH_4NO_3 formation in the observations, is also present in the model, suggesting that the simulated thermodynamic partitioning behaves similarly to the atmosphere, although the magnitude is low by ~5 ppb NH_4^+. In panels d–- f, the modeled points lie along the 1:1 line, indicating that SO_4^{2-} is fully neutralized and that sufficient NH_3 is available in the simulation to balance the modeled anions.

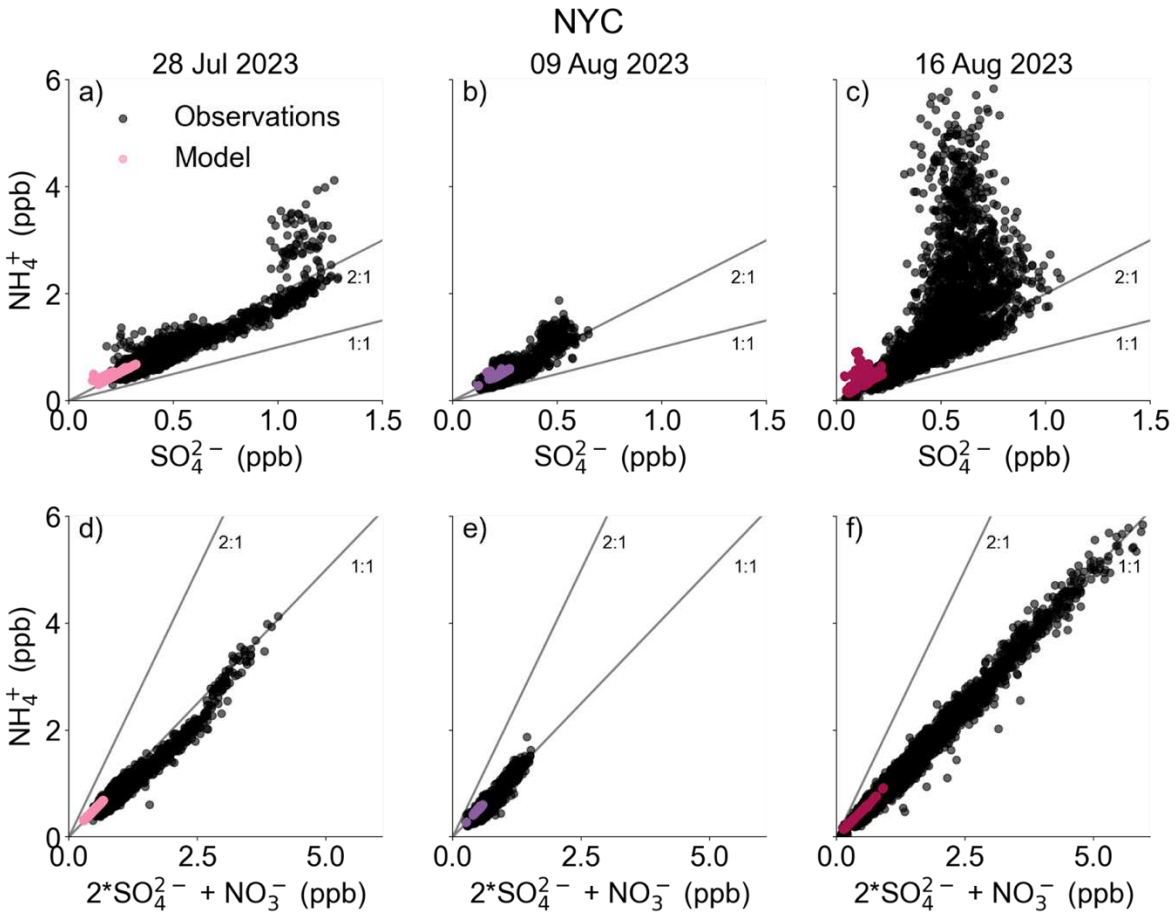

Figure 4.7: Scatter plots of simulated (color) and observed (black) NH_4^+ versus SO_4^{2-} (a–- c) and b) NH_4^+ versus $2*SO_4^{2-} + NO_3^-$ (d–- f), with the 2:1 and 1:1 lines plotted, for the 28 July, 09 August, and 16 August NYC flights.

Across all Chicago flights, the model systematically underpredicts SO_4^{2-}, with biases of up to ~3 ppb for NH_4^+ (2.2 μg m^{-3}), ~3 ppb for SO_4^{2-} (10.1 μg m^{-3}), and total anions ($2 \cdot SO_4^{2-} + NO_3^-$) by up to ~4.5 ppb (16.6 μg m^{-3}) (Figure 4.8). In the NH_4^+-SO_4^{2-} relationships (panels a–- e), the model frequently predicts NH_4NO_3 formation, with many modeled points approaching or exceeding the 2:1 line, whereas the observations span both $(NH_4)_2SO_4$ and NH_4NO_3 dominated regimes. This indicates that the model partitions a larger fraction of NH_4^+ to NO_3^- relative to the measurements for these cases. For the NH_4^+ versus $2*SO_4^{2-} + NO_3^-$ comparisons (panels f–- j), the modeled points consistently lie along the 1:1 line, indicating that sufficient NH_3 is always available in the model to fully neutralize SO_4^2. Although the simulation predicts more NO_3^- over Chicago

than NYC, the model still does not consistently reproduce the total observed inorganic aerosol mass.

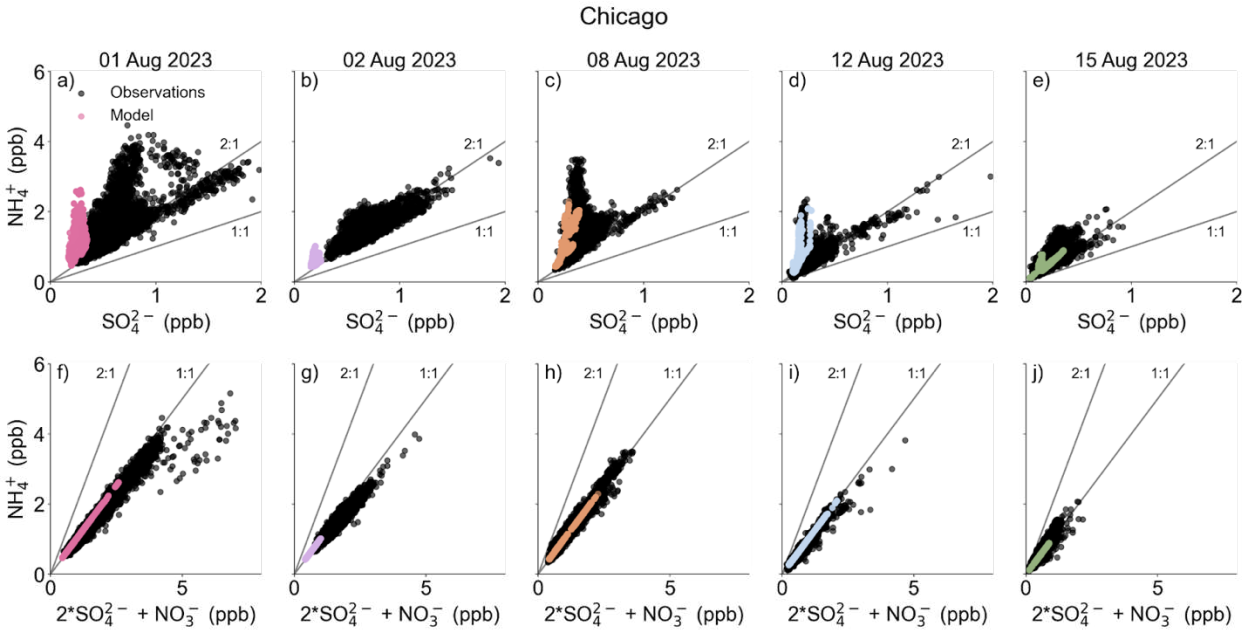

Figure 4.8: Scatter plots of modeled (color) observed (black) NH_4^+ v. SO_4^{2-} (a–- e) and b) NH_4^+ v. $2*SO_4^{2-} + NO_3^-$ (f–- j), with the 2:1 and 1:1 lines plotted, for the 01 August, 02 August, 08 August, 12 August, and 15 August Chicago flights.

Figures 4.9 and 4.10 show the spatial relationship between NH_4^+ partitioning and HNO_3 along the flight tracks for NYC and Chicago. Locations where NH_4^+:SO_4^{2-} > 3:1, indicative of NH_4NO_3 formation, consistently coincide with regions of elevated HNO_3 concentrations in both the observations and the model, demonstrating that NH_4NO_3 production is closely linked to the availability of HNO_3. For the 16 August NYC flight (Figure 4.9), observed NH_4NO_3 formation aligns with localized HNO_3 enhancements along the flight path; however, the model fails to reproduce both the elevated HNO_3 and the associated NH_4NO_3 formation, leading to a clear underprediction of NO_3^- production. On 01 August (Figure 4.10 a, d, g, j), the model overestimates both the magnitude and spatial extent of elevated HNO_3 and correspondingly overpredicts the spatial coverage of NH_4NO_3 formation. On 08 August (Figure 4.10 b, e, h, k), the model misplaces

the regions of enhanced HNO_3, failing to capture where elevated HNO_3 occurs and therefore missing the locations of NH_4NO_3 formation. On 12 August (Figure 4.10 c, f, i, l), the model again over predicts the magnitude and extent of HNO_3, resulting in an overly broad region of predicted NH_4NO_3 formation compared to observations. Across both NYC and Chicago, NH_4NO_3 formation consistently occurs in regions of elevated HNO_3, and model biases in the magnitude, spatial extent, or location of HNO_3 translate into corresponding errors in the prediction of NH_4NO_3 formation. Because HNO_3 is the final oxidation product of NO_x, inaccuracies in precursor NO_x concentrations could impact both the production rate and spatial distribution of HNO_3 and, therefore, NH_4NO_3 formation. Comparisons of modeled and observed NO_x in Figure C3 and Figure C4 indicate that the model both under- and overestimates NO_x concentrations along the flight tracks, which may influence estimates of HNO_3 concentration and NH_4NO_3 formation. In addition, uncertainties in NO_x oxidation and HNO_3 deposition could further impact inaccuracies in the model estimates of HNO_3. These results highlight that accurate simulation of HNO_3 distributions is critical for correctly representing NH_4NO_3 partitioning and total inorganic aerosol mass.

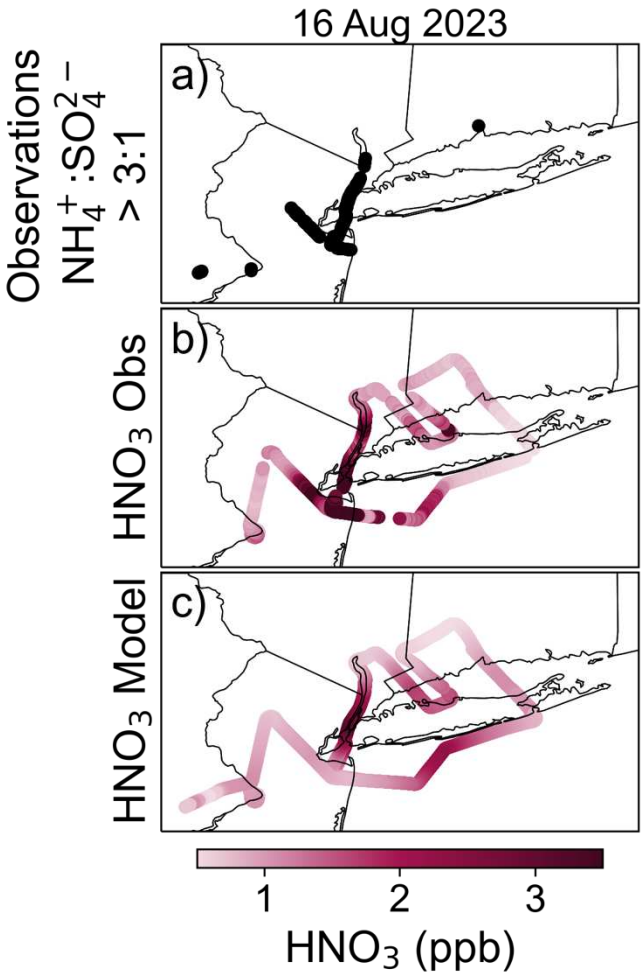

Figure 4.9: The locations of a) observations and flight tracks colored by b) observed (uncertainty = ±20% of measurement value + 25 pptv) and c) modeled HNO_3. Only NYC flights that had observed or modeled NH_4^+:SO_4^{2-} > 3:1 are shown.

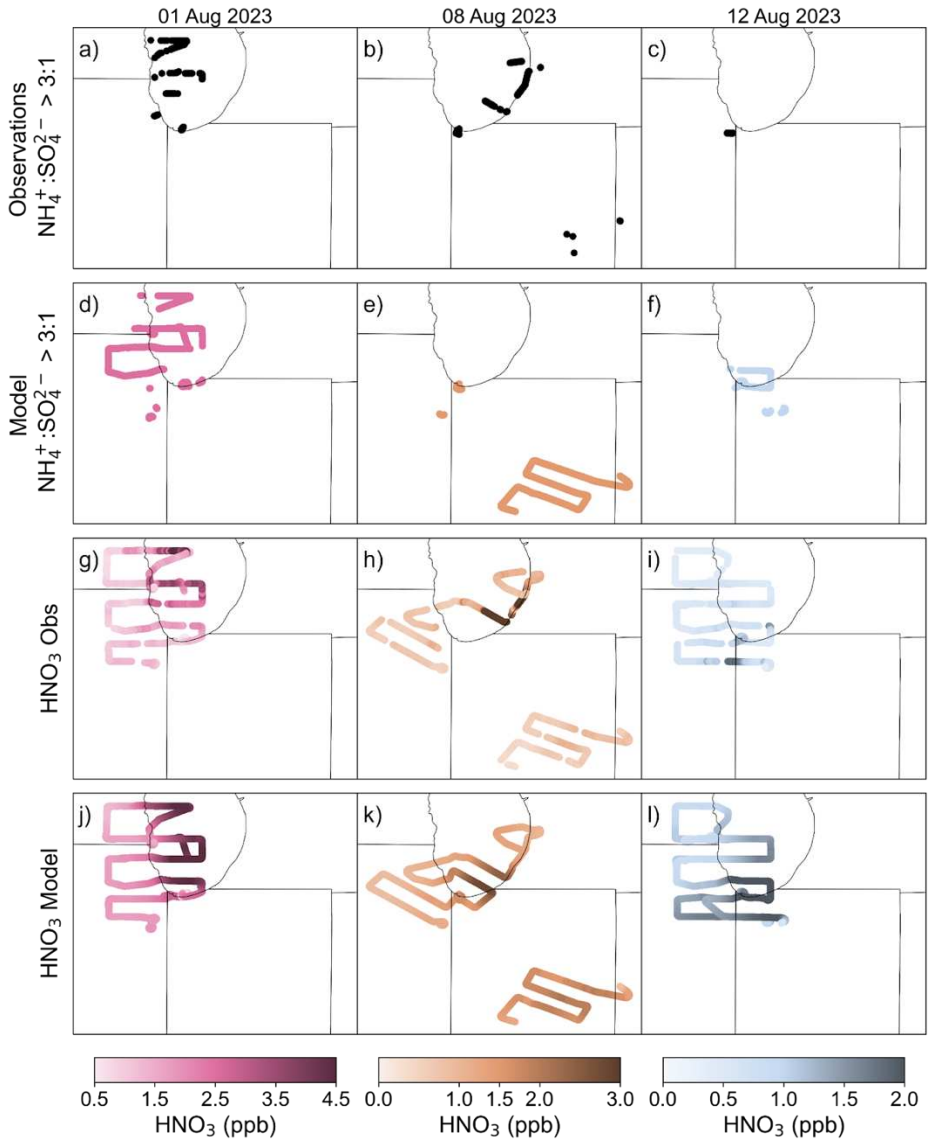

Figure 4.10: The locations of (a-c) observations and (d-f) modeled points where $NH_4^+:SO_4^{2-}$ > 3:1. Flight tracks colored by (g-i) observed and (j-l) modeled HNO_3. Only Chicago flights that had observed or modeled $NH_4^+:SO_4^{2-}$ > 3:1 are shown.

4.6 Discussion and Conclusions

This analysis provides a unique in situ evaluation of GEOS-Chem's ability to predict reduced nitrogen during the 2023 AEROMMA aircraft campaign over NYC and Chicago. Across both cities, the model captures the broad vertical structure and general variability of NH_x within the boundary layer, indicating that the large-scale distribution is reasonably represented.

However, aircraft observations reveal clear shortcomings in the model's ability to predict the magnitude, spatial localization, and temporal evolution of high-concentration urban plumes. While numerous studies have evaluated GEOS-Chem NH_3 estimations using satellite retrievals or long-term surface monitoring networks (Heald et al., 2012; L. Liu et al., 2019; Marais et al., 2021; Nair et al., 2019), direct comparisons against high-resolution in situ measurements remain extremely limited (Norman et al., 2025). Most previous work has focused on regional emissions or multi-year mean biases, leaving short-timescale urban plume behavior largely understudied. Our study evaluates the model at the spatial and temporal scales where emission inventories and chemical processes are most uncertain.

A consistent finding across both cities is that GEOS-Chem underestimates the strongest observed NH_x enhancements. Low biases have also been found in satellite and surface comparisons, which suggest that bottom-up inventories underestimate NH_3 emissions (Marais et al., 2021; Nair & Yu, 2020; Zhu et al., 2013). The aircraft observations show that this underestimation is particularly strong for localized urban plumes. In NYC, the missed plume over the urban core on 16 August is strongly linked to mobile-source tracers, suggesting that traffic-related ammonia emissions are underestimated in the model. The model resolution (0.25° x 0.3125°) is finer than the resolution of this plume (0.7272° x 0.5775°), indicating that the model resolution was not too coarse to resolve this plume. However, the model could be diluting the initial emission at the source over the grid, instead of predicting a concentrated plume, which is consistent with the underprediction of CO in the spiral over Trenton, NJ. Comparable behavior is seen in the comparison between the model output and observations near In Chicago, where sharp NH_3 plumes downwind of highways and within urban areas are absent or lessened in the

simulation. However, the model resolution is coarser than these plumes, so it is likely unable to resolve these hot spots.

The Trenton, NJ spirals suggest that temporal emission variability or boundary layer dynamics are not adequately captured. Observed late-afternoon enhancements indicate strong diurnal evolution in NH_x that is largely absent in the model. Prior model-observation comparisons have noted persistent seasonal and magnitude biases (Nair et al., 2019), but to our knowledge, no other studies have examined sub-daily variability in NH_x using vertically resolved in situ data. The disagreement observed here suggests that emission timing or boundary layer mixing processes are insufficiently represented. Urban NH_3 emissions from traffic, industrial activity, and temperature-dependent volatilization can vary throughout the day, and the lack of corresponding variability in GEOS-Chem points to limitations in temporal emission scaling that are not easily diagnosed from satellite or surface datasets alone.

Beyond individual plumes, the model exhibits a broader tendency towards a low bias in inorganic aerosol mass in both cities. While GEOS-Chem reproduces the qualitative structure of aerosol thermodynamic partitioning, it systematically underpredicts NH_4^+, SO_4^{2-}, and NO_3^-. We find that errors in HNO_3 drive many of the NO_3^- discrepancies. Spatial analyses demonstrate that NH_4NO_3 formation is tightly coupled to elevated HNO_3 in both observations and the model, but the simulation frequently misrepresents the magnitude or location of HNO_3 enhancements. As a result, the model either fails to produce NH_4NO_3 where it is observed or generates NH_4NO_3 over too broad a region. This behavior is consistent with previous findings that errors in precursors, rather than thermodynamic equilibrium itself, dominate inorganic aerosol biases (Heald et al., 2012), and highlights the importance of accurately representing HNO_3 production, transport, and loss in urban environments.

We also find that smoke may influence model performance. Within an intercepted wildfire plume over Gary, IN, the model underestimates NH_4^+ alongside SO_4^{2-} and CO, suggesting deficiencies in smoke chemistry or long-range transport. Our results suggest that reduced nitrogen biases are not confined to local urban emissions but extend to regional background and transported pollution.

These results suggest that GEOS-Chem captures the general structure of urban NH_x but can misses high concentration plumes that are larger than the model's resolution (i.e., NH_x plume in downtown NYC). Underestimation of mobile-source NH_3, insufficient sub-daily variability, and misrepresentation of HNO_3 collectively lead to a low bias in peak NH_x and inorganic aerosol mass. Because NH_4NO_3 is a major component of fine particulate matter in many cities, these errors have direct implications for air quality forecasting, exposure assessment, and policy-relevant modeling. Improving model performance will likely require updated urban NH_3 emission inventories, and a better representation of traffic-related sources and HNO_3 sources and sinks. Higher-resolution simulations may also be necessary to resolve sharp urban plumes that are currently diluted at the model grid scale. The AEROMMA aircraft observations demonstrate the value of high-frequency in situ measurements for understanding model deficiencies and provide constraints that cannot be obtained from satellite or surface networks alone.

CHAPTER 5

CANADIAN WILDFIRE SMOKE IMPACTS ON REDUCED NITROGEN IN THE UPPER MIDWEST: INSIGHTS FROM THE 2023 FIRE SEASON

5.1 INTRODUCTION TO THE 2023 CANADIAN WILDFIRES

The summer of 2023 was the most severe Canadian wildfire season on record, with approximately 15.0 Mha burned, nearly seven times the long-term annual average (Byrne et al., 2024; Jain et al., 2024). The fires were primarily in western Canada and Quebec, accounting for nearly 90% of the total burned area (Chen et al., 2025). Persistent hot and dry conditions facilitated rapid fire spread and sustained emissions throughout the summer (Kirchmeier-Young et al., 2024). Smoke from these fires was efficiently transported southward and eastward by large-scale circulation patterns, resulting in widespread and episodic degradation of air quality across the midwestern and eastern United States (Chen et al., 2025; Cooper et al., 2024; Wang et al., 2024; Zhang et al., 2025). These long-range transport events produced extreme $PM_{2.5}$ concentrations, exposed hundreds of millions of people to elevated pollution levels, and led to measurable adverse health impacts in North America (Chen et al., 2025; Zhang et al., 2025). Together, the unprecedented scale and long-range transport of emissions during the 2023 Canadian wildfire season highlight the potential for wildfire-derived reduced nitrogen to substantially influence NH_3 concentrations and NH_4^+ deposition far downwind, underscoring the need to better quantify these impacts at regional to continental scales.

5.2 SATELLITE GROUND-BASED EVIDENCE OF WILDFIRE-DRIVEN NH_3 ENHANCEMENTS

During the summer of 2023, there were major wildfires throughout Canada, and the smoke impacted the midwestern and northeastern regions of the U.S. for a period of weeks

(Cooper et al., 2024; Z. Wang et al., 2024). We show an example of one day (01 August 2023) when HMS plumes indicated that smoke from Canadian wildfires extended over the Upper Midwestern and Northeastern U.S. (Figure 5.1a). CrIS also detected enhancements in column average NH_3 of ~2 - 7 ppbv co-located with the smoke plume over the Upper Midwest (Figure 5.1b). The highest observed column average NH_3 values (~7 ppbv) were co-located with the heavy HMS-indicated smoke plumes. 01 August was chosen for this specific case study as there was a coinciding AEROMMA flight over Chicago that sampled the edge of the high NH_3 plume observed by CrIS and the light/medium smoke HMS plumes (Figure 5.1c).

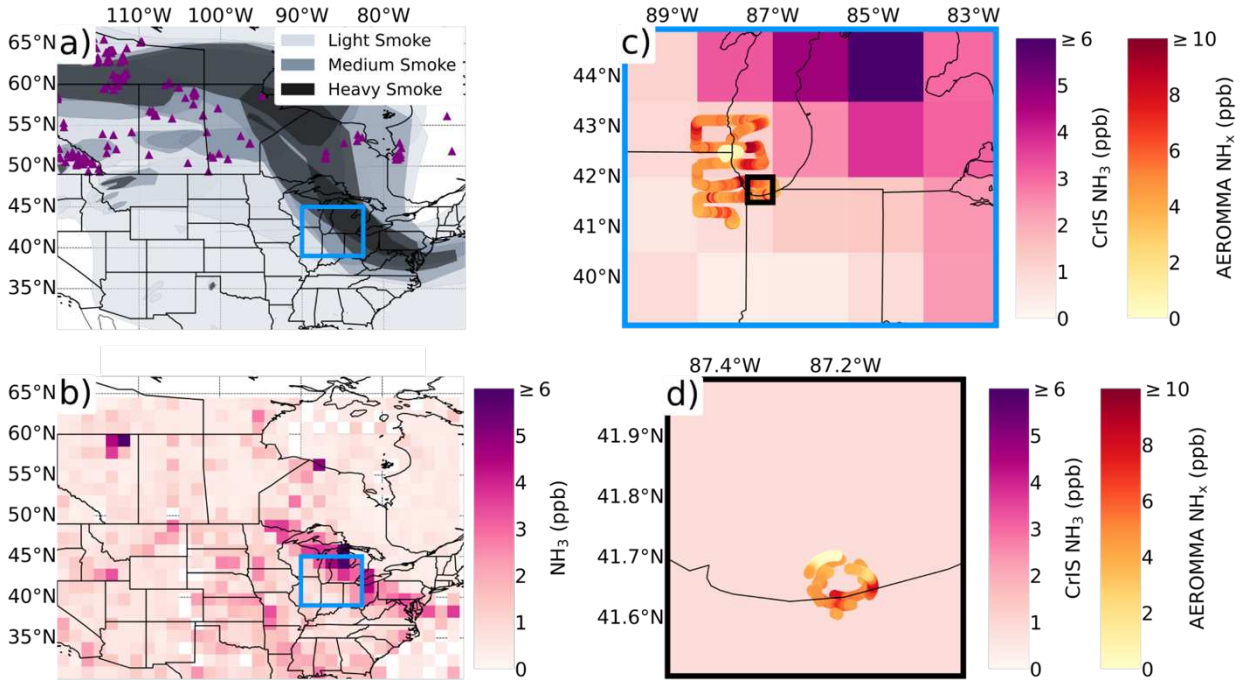

Figure 5.1: a) Map of HMS plumes (colored shading) and Canadian fire locations (purple triangles) on 01 August 2023. b) Map of CrIS column average NH_3 on a 1.5° grid on 01 August 2023. The blue box in a) and b) represents the extent of c), which shows CrIS column average NH_3 overlaid with the AEROMMA flight track (136 - 7143 m ASL) from 01 August 2023 colored by the AEROMMA observed NH_x mixing ratio. The black box in c) represents the extent of d), which shows CrIS column average NH_3 overlaid with the AEROMMA flight track of the spiral over Gary, Indiana on 01 August 2023 that was determined to be smoke-impacted and further discussed in Figure 5.3.

In 2023, there was a higher-than-average frequency of smoke overhead, as indicated by HMS plumes, across the eastern half of the US as compared to the previous decade (2013 - 2022) in May, June, July, and August (Figure D1). In May and June 2023, the Upper Midwestern region experienced ~70 - 100% of days with smoke overhead, compared to the 2013 – 2022 average, where ~0 - 50% of days had smoke overhead. Figure 5.2 shows average May-June NH_3 concentration and NH_4^+ deposition flux for 2023 and 2018 - 2022 throughout the U.S. The 2018 – 2023 time period was chosen as the number of AMON sites increased in 2018 (R. Wang et al., 2023). Across CONUS, there was an increase in average May – June NH_3 concentration in 2023 across 69% (50 out of 72) AMON stations, with 21% (15 out of 72) having a significant increase at 95% confidence compared to the 2018 - 2022 average. Differences between the two averages for individual sites ranged from -1.5 - 2.8 $\mu g\ m^{-3}$. There was an increase in average May-August NH_4^+ deposition flux in 2023 across 52% (42 out of 80) CASTNET stations, with 10% (8 out of 80) having a significant increase at 95% confidence compared to the 2018 - 2022 average. Differences between the two averages for individual sites ranged from -0.00075 - 0.0034 kg $NH_4^+\ ha^{-1}$. While NH_3 concentration, as observed by AMON stations, has been increasing over time, the year-to-year increases have not been statistically significant (95% confidence) (Butler et al., 2016). Vo & Christiansen (2024) found that AMON NH_3 concentrations had been increasing at 5 out of 10 AMON stations in the Midwest between 2014 – 2019, with one station having a significant increase. CASTNET NH_4^+ flux has been decreasing over time (Figure D2). Elemental carbon measured from the Interagency Monitoring of Protected Visual Environments (IMPROVE) network displayed increases in May – June elemental carbon concentrations in 2023 compared to the 2018 - 2022 average at 7 out of 8 stations in the Upper Midwest, with 2 stations having a significant increase (95% confidence) (Figure D3). This suggests that the

statistically significant NH_x increases observed in May – June 2023 are likely attributable to the wildfire smoke events rather than long-term trends or other factors. The Upper Midwest had a higher percentage of stations that observed an increase in NH_3 concentration (83%: 5 out of 6 stations, with 2 stations (33%) experiencing a significant increase at 95% confidence) and NH_4^+ deposition flux (100%: 5 out of 5 stations, with 3 stations (60%) having a significant increase at 95% confidence) than what was observed nationally on average from 2018 – 2022. May – June averaged CrIS column averaged NH_3 data also shows increases in NH_3 mixing ratios in 2023, compared to the 2021 – 2022 average. In the contiguous U.S., 21% (140 out of 663) of grid cells had significant increases (at 95% confidence) in column average NH_3 mixing ratios in 2023, and 47% (34 out of 73) grid cells in the Upper Midwest had significant increases (at 95% confidence) in column average NH_3 mixing ratios in 2023.

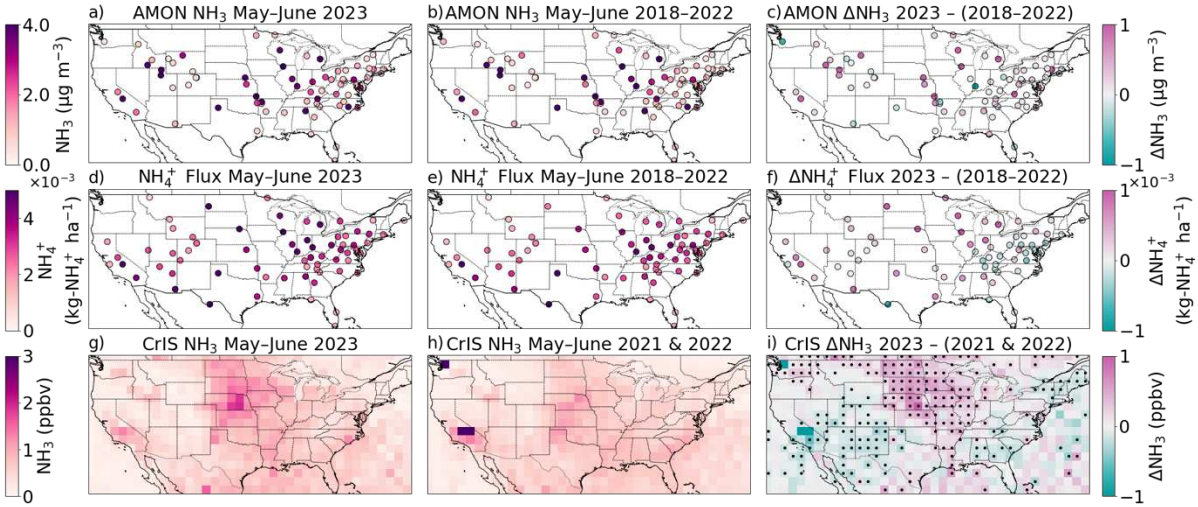

Figure 5.2: Maps of active AMON (a - c) and CASTNET (d - f) stations colored by average May – June concentrations of NH_3 concentration and NH_4^+ deposition flux respectively, in 2023 (a, d), average May – June in 2018 – 2022 (b, e), and the difference between the two averages (c, f). (g) Map of column average CrIS gridded NH_3 mixing ratio averaged from May – June 2023, (h) Map of column average CrIS gridded NH_3 mixing ratio averaged from May – June 2021 & 2022, and (i) the difference between the grid cell averages in (g) and (h) with grid cells where the difference is significant at the 95% confidence level indicated by a black dot (i).

5.3 Aircraft Evidence of Wildfire-Driven NH_3 Enhancements

During AEROMMA, the DC-8 flew through a smoke plume over Gary, IN on 01 August 2023 (Figure 5.1d). The plume originated in Canada five days earlier (Cooper et al., 2024). CrIS observed elevated NH_3 within the plume (Figure 5.1). The DC-8 flew vertical profiles over Gary, IN, through the plume and observed co-located enhancements of NH_x, CO, and CH_3CN between ~2.5 - 4 km (Figure 5.3). The NH_3 vertical profile follows a similar pattern to the NH_x profile, except for between ~3.25 - 4 km, where NH_3 is depleted but NH_x is enhanced and follows a similar pattern to CO and CH_3CN, suggesting that there is partitioning to the aerosol phase at higher altitudes with lower temperatures. Cooper et al. (2024) found that this plume had strong photochemical ozone (O_3) production in the free troposphere and was isolated from surface emissions. The ΔNH_3:ΔCO ratio in this plume, calculated using reduced major axis regression (RMA) as done in Lill et al. (in press), is 0.01, and the ΔNH_x:ΔCO ratio is 0.02. While these ratios are lower than those reported in Lindaas et al. (2021) for 4 hr old smoke plumes (ΔNH_3:ΔCO ratio: 0.02 - 0.03, ΔNH_x:ΔCO ratio: 0.03 - 0.04), they are not significantly different, suggesting that the NH_3 is moving long distances at altitude. Smoke-free ΔNH_3:ΔCO and ΔNH_x:ΔCO ratios from AEROMMA in LA, NYC, and Chicago that were associated with traffic were higher than the ratio in the smoke-impacted Gary plume and ranged from 0.014 - 0.041 (ΔNH_3:ΔCO) and 0.030 - 0.069 (ΔNH_x:ΔCO) (Lill et al., in press).

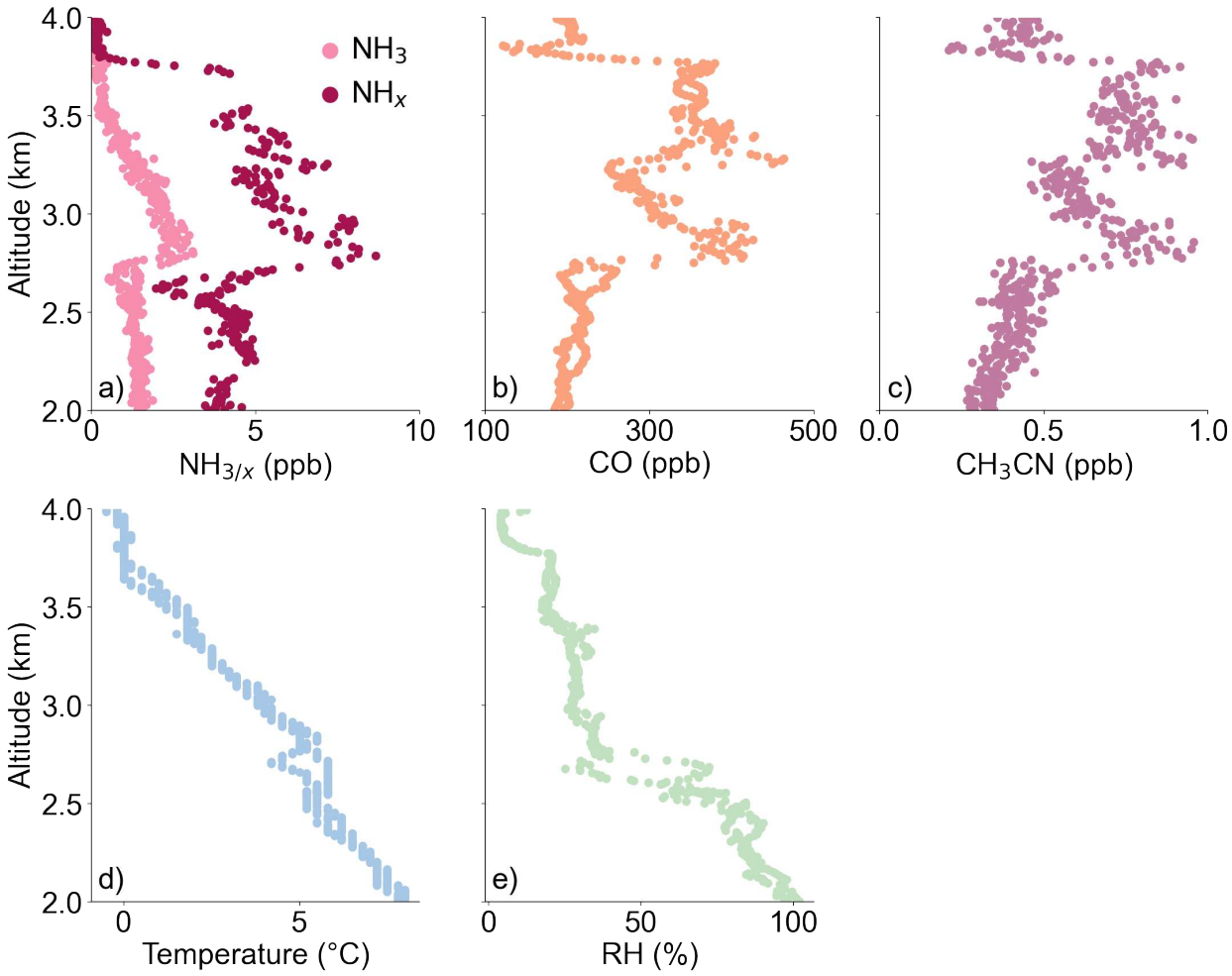

Figure 5.3: Profiles of a) NH_3 and NH_x, b) CO, c) CH_3CN, d) temperature, and e) relative humidity between 2 - 4 km during the smoke-impacted spiral over Gary, IN on 01 August 2023.

5.4 Observed Surface NH_3 Concentration and NH_4^+ Deposition Anomalies in 2023

In the Upper Midwest from 01 May - 01 August 2023, 7 out of 8 stations AMoN stations observed significant increases in bi-weekly average NH_3 concentration as compared to the bi-weekly average of the same measurement period in all years other than 2023 when the site was active (Figure 5.4). The only site that did not observe any periods of significant increases in NH_3 concentration was Odanah, WI. This site was also not operational until October 2018 so it has fewer non-2023 data points than all of the other sites with the exception of Madison, WI (Table

S1). All of the CASTNET stations observed significant increases in NH_4^+ deposition flux in 2023 as compared to the bi-weekly average of the same measurement period in all years other than 2023 when the site was active (Figure 5.4). Many of the sites observed a decrease in NH_3 concentration and NH_4^+ deposition flux in early to mid-June 2023 despite there being heavy smoke overhead. A similar pattern was also observed in elemental carbon concentrations measured by the IMPROVE network (Figure D4), suggesting that while there was smoke overhead during this period, it did not reach the ground.

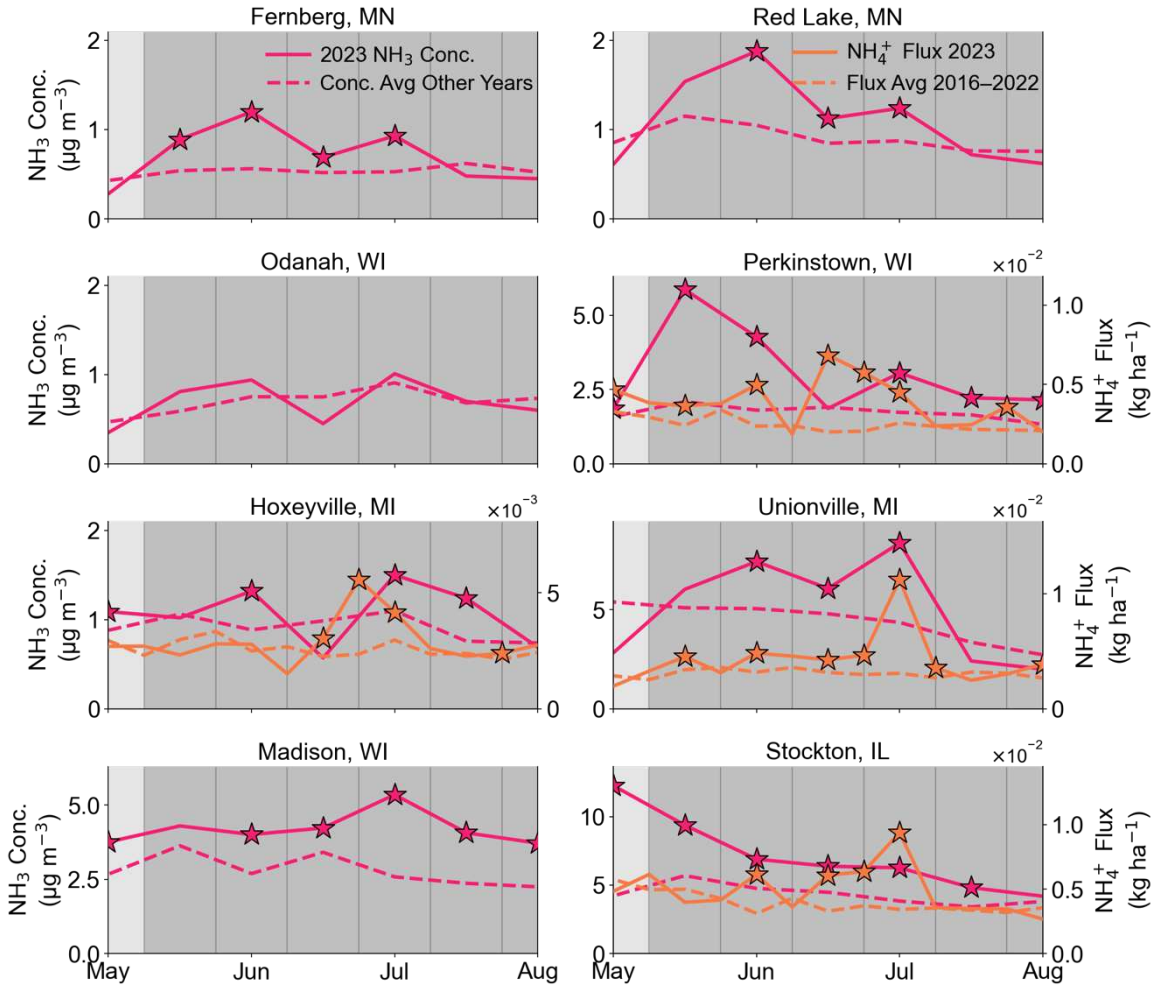

Figure 5.4: Time series of observed 01 May - 01 August AMoN NH_3 concentration in 2023 (solid line) and the average of previous years (dashed line) shown in pink, and the CASTNET NH_4^+ flux in 2023 (solid line) and the average of 2016 - 2022 (dashed line) shown in orange. Stars on the 2023 value indicate if that observation is significantly higher (95% confidence) than the previous year's average for that measurement period. The start and end dates for each station's NH_3 concentration and NH_4^+ flux measurement periods can be found in Table S1 and Table S2, respectively. Light grey shading indicates that there was light/medium smoke impact during the 2-week AMoN sampling period and dark grey shading indicates that there was heavy smoke impact during the 2-week AMoN sampling period. Sites are ordered from Northernmost at the top to Southernmost at the bottom. Figure S5 shows the variability of the values used for the other years' average.

5.5 Discussion and Implications

We found that wildfire smoke significantly increased NH_3 concentrations across large regions of the U.S., particularly in the Upper Midwest during the 2023 Canadian fire season. We also found that when smoke plumes pass over the Upper Midwest, there are significant increases

in measured NH_3 concentrations in the atmospheric column and at the surface. This demonstrates that wildfire emissions can influence atmospheric NH_3 far downwind from their source. Previous work utilizing passive monitoring of $NH_{3/x}$ found correlations between biomass burning events and elevated $NH_{3/x}$ concentration. Chen et al. (2014) found that measurement sites in the western U.S. observed elevated concentrations of NH_x occurring simultaneously with elevated levels of biomass burning tracers at the time of large fires nearby. Saylor et al. (2015) analyzed trends in NH_3 concentrations in the southeastern U.S. from 2004 to 2012 and found anomalously high NH_3 concentrations in 2007, correlated with a three-times increase in the number of acres burned by wildfire that year over 2005. Lutsch et al. (2019) observed 2 - 5 times higher NH_3 concentrations in the high Arctic in 2017 due to Canadian wildfires. Extreme boreal fires have also been associated with high NH_3 emissions, comparable to agricultural regions (Q. Chen et al., 2025). These results are consistent with our findings that 7 out of 8 passive NH_3 monitors in the Upper Midwest observed periods of significantly higher (95% confidence) NH_3 concentrations in 01 May - 01 August 2023 when there was heavy smoke impact.

We show that wildfire smoke in 2023 also led to increases in NH_4^+ deposition flux at all monitoring sites in the Upper Midwest. Previous work has also found that wildfires have led to increases in NH_4^+ deposition. Karlsson et al. (2013) found that high NH_4^+ dry deposition in a forest in Sweden was associated with a smoke plume from fires in Eastern Europe. Campbell et al. (2022) found that there was elevated NH_4^+ dry deposition in California during the August Complex fire in 2020.

These findings highlight the substantial impact of wildfire smoke on NH_3 and NH_4^+ at regional scales, with implications for nitrogen cycling, air quality, and atmospheric modeling. Although it has been shown that the relative contribution of wildfires to nitrogen deposition in

the Upper Midwest is low (Koplitz et al., 2021), we find that in extreme fire seasons like 2023, it can have statistically significant impacts on NH_3 concentrations and NH_4^+ deposition fluxes. Fire frequency and intensity are projected to increase under climate change. Thus, future work should evaluate how wildfire-driven NH_3 emissions compare to agricultural sources regionally, as the impact of wildfire smoke as a nitrogen source may be more pronounced in areas with lower background agricultural emissions. Additionally, improved modeling of NH_3 lifetime, transport, and partitioning during smoke events is necessary to better estimate dry and wet deposition fluxes and their environmental impacts. The integration of satellite, ground-based, and aircraft data will be essential to understanding the extent of wildfire contributions to reduced nitrogen cycling and informing air quality management strategies in a changing climate.

CHAPTER 6

SUMMARY, CONCLUSIONS, AND RECOMMENDATIONS FOR FUTURE RESEARCH

6.1 SUMMARY

This dissertation investigates the sources, abundance, partitioning, and transport of atmospheric reduced N in North American urban environments and during extreme wildfire events. It presents an analysis of observations from the Atmospheric Emissions and Reactions Observed from Megacities to Marine Areas (AEROMMA) airborne field campaign conducted during the summer of 2023 over LA, NYC, and Chicago, as well as complementary satellite, ground-based, and modeling datasets. This work is organized into three chapters. Chapter 3 quantifies boundary-layer NH_3 and NH_x mixing ratios over major U.S. cities and examines spatial variability, partitioning, and source influences using tracer–tracer relationships, identifying traffic as a dominant contributor to urban NH_3 during summer. Chapter 4 presents an assessment of the representation of NH_3 and NH_x in GEOS-Chem over NYC and Chicago, demonstrating that while the model captures the general vertical structure and partitioning of reduced N, it systematically underestimates the magnitude of localized urban plumes, likely due to underestimated mobile-source emissions, insufficient temporal variability, and model resolution. Chapter 5 explores the impacts of the 2023 Canadian wildfire season on reduced nitrogen across the Upper Midwest, combining aircraft, satellite, and surface observations to show that wildfire smoke significantly enhanced NH_3 concentrations and NH_4^+ deposition over regional scales.

6.2 CHAPTER 3 OVERVIEW

Using in situ NH_3 and NH_x observations from the 2023 AEROMMA field campaign, Chapter 3 characterizes the abundance, phase partitioning, and dominant sources of reduced N in the boundary layer over major North American cities, with a focus on LA, NYC, and Chicago.

The analysis shows that summertime urban NH_3 mixing ratios vary between cities, with the highest average NH_3 observed over Los Angeles and lowest average values over NYC. Boundary-layer NH_x partitioning also varies by city and meteorological conditions, ranging from predominantly gas-phase NH_3 in LA and Chicago, to cooler, more humid conditions in NYC where a substantial fraction of NH_x is in the particle phase as NH_4^+. This is characteristic of summertime conditions with more NH_4^+ expected in cooler times of the year. Relationships between NH_3 and co-emitted tracers including CO, ethyne, NO_x, and NO_y, imply that traffic-related emissions are a major contributor to urban $NH_{3/x}$ during summer. Observed ΔNH_3:ΔCO and ΔNH_x:ΔCO enhancement ratios are often larger than those predicted by the NEI for on-road vehicles, suggesting that mobile-source NH_3 emissions are underestimated. The results of Chapter 3 provide observational constraints on urban NH_3 abundances, phase partitioning, and source attribution, establishing a foundation for the model evaluation and wildfire analyses presented in subsequent chapters.

6.3 Chapter 4 Overview

Chapter 4 evaluates the ability of GEOS-Chem to represent reduced nitrogen in NYC and Chicago using observations from the 2023 AEROMMA field campaign. A comparison of observed and modeled vertical profiles of NH_3, NH_4^+, and NH_x sampled along the aircraft flight tracks within the boundary layer shows that GEOS-Chem reproduces the general vertical distribution and variability of reduced N across multiple flights; however, the model frequently underestimates the magnitude of the strongest observed NH_3 and NH_x enhancements, in some cases by > 5 - 6 ppb. Several urban plumes in the observations are either substantially underpredicted or absent in the model simulations. Analysis of a missed NH_x plume over NYC on 16 August reveals strong correlations between observed NH_x and multiple traffic-related tracers, including CO, ethyne, NO_x, and toluene, indicating that the plume is dominated by mobile-source emissions. Similar

discrepancies are identified in Chicago, where GEOS-Chem fails to reproduce sharp NH_3 plumes observed downwind of highways and within urban outflow. These plumes in Chicago were smaller than the model resolution, however, the high NH_x plume in NYC was larger than the model resolution. While GEOS-Chem captures the overall thermodynamic behavior of inorganic aerosol partitioning, it tends to exhibit a low bias in total inorganic aerosol mass. The findings in Chapter 4 demonstrate that although GEOS-Chem captures the broad structure of urban reduced nitrogen, deficiencies in emission inventories, temporal variability, and model resolution lead to persistent underestimation of peak NH_3 and NH_x concentrations, which has important implications for air quality modeling and exposure assessment.

6.4 Chapter 5 Overview

Chapter 5 investigates the impact of the 2023 Canadian wildfire season on NH_3 and NH_4^+ across the Upper Midwest, integrating aircraft observations from AEROMMA with satellite and ground-based measurements. On 01 August 2023, an HMS smoke plume was co-located with elevated column average NH_3 observed by CrIS (2 - 7 ppb), with the highest NH_3 enhancements co-located with heavy HMS plumes. On the same day, an AEROMMA research flight over Chicago sampled smoke-influenced air and observed elevated NH_3 coincident with enhancements in CH_3CN and CO, both smoke tracers. Surface monitoring data indicate that wildfire smoke during the 2023 fire season led to significant increases in NH_3 concentration and NH_4^+ deposition flux throughout the Upper Midwest. These results indicate that while wildfires are typically a minor contributor to reduced nitrogen deposition in this region, extreme fire seasons can produce measurable impacts on both atmospheric NH_3 concentrations and nitrogen deposition at regional scales.

6.5 Recommendations for Future Research

There are several major routes to extend this work, spanning seasonal observations, flight design, coordinated satellite-aircraft analyses, and continued model development. Some of these extensions build directly on the AEROMMA framework, while others require broader coordination across platforms and research communities. Additional field campaigns in other seasons are needed to place the summer observations presented here into a full annual context. Refined sampling strategies will allow for a better understanding of plume evolution and vertical structure. Satellite observations offer an opportunity to expand these analyses across longer timescales and larger spatial domains, particularly when paired with dedicated validation efforts. Finally, continued improvements to chemical transport models and emission inventories are needed for translating observations into predictive capability. In the following sections, I outline specific recommendations within each of these areas that would most directly advance understanding of urban reduced nitrogen.

6.5.1 Campaigns in Other Seasons

The AEROMMA observations analyzed in this dissertation were collected exclusively during summer 2023. Warm summertime temperatures favor gas-phase NH_3 and suppress NH_4NO_3 formation. Consequently, the partitioning behavior observed during this campaign likely represents only one end of the seasonal spectrum. In colder seasons, lower temperatures and higher relative humidity favor the formation of particulate NH_4NO_3, potentially shifting NH_x from a gas-dominated to particle-dominated regime. This raises several unanswered questions: 1) How does the seasonal cycle alter the gas-particle partitioning of reduced nitrogen in urban environments? 2) Does vehicular NH_3 remain the dominant urban source in winter, or do residential combustion and agricultural transport become more important? 3) Are model biases larger or smaller when

aerosol formation is thermodynamically favored? Winter and shoulder-season campaigns would also allow investigation of boundary layer structure and stagnation events, which are known to enhance $PM_{2.5}$. Cold-season inversions may trap NH_3 and HNO_3 near the surface, amplifying inorganic aerosol formation in ways not captured during summertime sampling.

If future campaigns are conducted, I recommend establishing at least one fixed urban supersite operating concurrently with aircraft measurements. This site should include continuous NH_3, aerosol composition, NO_x, CO, HNO_3, and meteorology measurements. Pairing aircraft spirals with ground supersites would allow for a better understanding of the vertical distribution of reduced nitrogen, how emission signatures evolve with altitude, and provide temporal context outside flight hours. Integration with low-cost PM sensors (e.g., PurpleAir networks) could help map the spatial footprint of NH_4NO_3 episodes and identify neighborhoods disproportionately impacted by wintertime aerosol formation.

6.5.2 Updated Sampling Strategy

While the AEROMMA sampling strategy successfully captured urban plumes, it was not optimized for repeated sampling of the same air mass. Aircraft traffic control restrictions played a significant role in shaping the flight paths during AEROMMA, particularly in NYC and LA. As a result, the ability to follow plumes downwind was limited, and we lack a complete picture of plume evolution. Future campaigns should incorporate pseudo-Lagrangian flight patterns designed to follow the same urban plume at multiple distances downwind. In cities with strict ATC restrictions, like NYC and LA, sampling over water when the urban outflow is directed offshore may offer greater flexibility, allowing more continuous plume tracking without compromising safety or regulatory compliance. Also, a smaller aircraft with reduced payload (i.e., NH_3, HNO_3, and PILS aerosol composition) could also offer more flexibility in a study specifically targeted at NH_3

emissions and evolution in these cities. I also suggest that this sampling strategy be repeated after the first pseudo-Lagrangian sampling in order to better our understanding of how emissions vary throughout the day. This strategy would enable direct estimation of chemical aging, dilution rates, and gas-particle partitioning timescales.

Dedicated emission-focused flights would also be valuable. Curtain transects perpendicular to highways or major traffic corridors, extending from low altitudes to the top of the boundary layer, would help to constrain vertical mixing and plume depth. Resolving this structure would be beneficial for interpreting emission ratios and for evaluating modeled dilution of plumes downwind from the emission source.

6.5.3 Coordinated Satellite and In-Situ Measurements

Satellite retrievals of NH_3 offer a powerful complement to aircraft observations but remain underutilized in urban studies. Instruments such as CrIS provide regional NH_3 distributions, yet its spatial resolution is coarse relative to individual city plumes. CrIS, in particular, has only a single degree of freedom, which limits its ability to resolve NH_3 profiles. As a result, the vertical placement of NH_3 in CrIS retrievals relies heavily on assumed atmospheric profiles and may not capture lofted plumes (e.g., from wildfires). Aircraft measurements are uniquely positioned to validate these assumptions. Coordinated overpasses in which aircraft sample along satellite paths, alongside sub-pixel sampling, would enable direct evaluation of column sensitivity and the vertical distribution of NH_3, providing a critical check on where CrIS places the ammonia.

Oversampling algorithms could then be applied to multi-year satellite datasets to derive climatological urban NH_3 enhancement patterns. Satellite analysis should not be viewed as a replacement for aircraft campaigns, but rather as a tool that extends aircraft-derived process understanding across seasons and years. Future campaigns should therefore explicitly include

validation objectives for satellite retrievals, leveraging aircraft measurements to refine vertical placement and improve confidence in urban NH_3 measurements.

6.5.4 Modeling and Chemical Mechanism Development

The assessment of GEOS-Chem estimates of NH_x in this dissertation reveal several systematic deficiencies that motivate targeted model development. One important area for development is improved representation of mobile-source NH_3 emissions. Current inventories appear to underestimate traffic-related NH_3 and updated emission factors derived from tunnel, roadside, and aircraft studies should be incorporated into future inventories. Chemical mechanism improvements are also needed. Errors in HNO_3 distributions directly translate into NH_4NO_3 biases. This suggests that chemistry and partitioning require further refinement. Smoke chemistry adds another layer of complexity. The underestimation of NH_4^+ within transported wildfire plumes indicates that biomass burning emissions and aging pathways are not fully captured.

REFERENCES

Allen, H. M., Crounse, J. D., Kim, M. J., Teng, A. P., Ray, E. A., McKain, K., Sweeney, C., & Wennberg, P. O. (2022). H2O2 and CH3OOH (MHP) in the Remote Atmosphere: 1. Global Distribution and Regional Influences. *Journal of Geophysical Research: Atmospheres*, *127*(6), e2021JD035701. https://doi.org/10.1029/2021JD035701

Amos, H. M., Jacob, D. J., Holmes, C. D., Fisher, J. A., Wang, Q., Yantosca, R. M., Corbitt, E. S., Galarneau, E., Rutter, A. P., Gustin, M. S., Steffen, A., Schauer, J. J., Graydon, J. A., Louis, V. L. S., Talbot, R. W., Edgerton, E. S., Zhang, Y., & Sunderland, E. M. (2012). Gas-particle partitioning of atmospheric Hg(II) and its effect on global mercury deposition. *Atmospheric Chemistry and Physics*, *12*(1), 591–603. https://doi.org/10.5194/acp-12-591-2012

Baron, J. S., Rueth, H. M., Wolfe, A. M., Nydick, K. R., Allstott, E. J., Minear, J. T., & Moraska, B. (2000). Ecosystem Responses to Nitrogen Deposition in the Colorado Front Range. *Ecosystems*, *3*(4), 352–368. https://doi.org/10.1007/s100210000032

Bauer, S. E., Koch, D., Unger, N., Metzger, S. M., Shindell, D. T., & Streets, D. G. (2007). Nitrate aerosols today and in 2030: A global simulation including aerosols and tropospheric ozone. *Atmospheric Chemistry and Physics*, *7*(19), 5043–5059. https://doi.org/10.5194/acp-7-5043-2007

Behera, S. N., Sharma, M., Aneja, V. P., & Balasubramanian, R. (2013). Ammonia in the atmosphere: A review on emission sources, atmospheric chemistry and deposition on terrestrial bodies. *Environmental Science and Pollution Research*, *20*(11), 8092–8131. https://doi.org/10.1007/s11356-013-2051-9

Benedict, K. B., Carrico, C. M., Kreidenweis, S. M., Schichtel, B., Malm, W. C., & Collett Jr., J. L. (2013). A seasonal nitrogen deposition budget for Rocky Mountain National Park. *Ecological Applications*, *23*(5), 1156–1169. https://doi.org/10.1890/12-1624.1

Benish, S. E., Bash, J. O., Foley, K. M., Appel, K. W., Hogrefe, C., Gilliam, R., & Pouliot, G. (2022). Long-term regional trends of nitrogen and sulfur deposition in the United States from 2002 to 2017. *Atmospheric Chemistry and Physics*, *22*(19), 12749–12767. https://doi.org/10.5194/acp-22-12749-2022

Bishop, G. A., Peddle, A. M., Stedman, D. H., & Zhan, T. (2010). On-Road Emission Measurements of Reactive Nitrogen Compounds from Three California Cities. *Environmental Science & Technology*, *44*(9), 3616–3620. https://doi.org/10.1021/es903722p

Bishop, G. A., & Stedman, D. H. (2015). Reactive Nitrogen Species Emission Trends in Three Light-/Medium-Duty United States Fleets. *Environmental Science & Technology*, *49*(18), 11234–11240. https://doi.org/10.1021/acs.est.5b02392

Bouwman, A. F., Lee, D. S., Asman, W. a. H., Dentener, F. J., Van Der Hoek, K. W., & Olivier, J. G. J. (1997). A global high-resolution emission inventory for ammonia. *Global Biogeochemical Cycles*, *11*(4), 561–587. https://doi.org/10.1029/97GB02266

Bray, C. D., Battye, W., Aneja, V. P., Tong, D. Q., Lee, P., & Tang, Y. (2018). Ammonia emissions from biomass burning in the continental United States. *Atmospheric Environment*, *187*, 50–61. https://doi.org/10.1016/j.atmosenv.2018.05.052

Bray, C. D., Battye, W. H., Aneja, V. P., & Schlesinger, W. H. (2021). Global emissions of NH3, NOx, and N2O from biomass burning and the impact of climate change. *Journal of the*

Air & Waste Management Association, *71*(1), 102–114. https://doi.org/10.1080/10962247.2020.1842822

Breider, T. J., Mickley, L. J., Jacob, D. J., Ge, C., Wang, J., Payer Sulprizio, M., Croft, B., Ridley, D. A., McConnell, J. R., Sharma, S., Husain, L., Dutkiewicz, V. A., Eleftheriadis, K., Skov, H., & Hopke, P. K. (2017). Multidecadal trends in aerosol radiative forcing over the Arctic: Contribution of changes in anthropogenic aerosol to Arctic warming since 1980. *Journal of Geophysical Research: Atmospheres*, *122*(6), 3573–3594. https://doi.org/10.1002/2016JD025321

Byrne, B., Liu, J., Bowman, K. W., Pascolini-Campbell, M., Chatterjee, A., Pandey, S., Miyazaki, K., van der Werf, G. R., Wunch, D., Wennberg, P. O., Roehl, C. M., & Sinha, S. (2024). Carbon emissions from the 2023 Canadian wildfires. *Nature*, *633*(8031), 835–839. https://doi.org/10.1038/s41586-024-07878-z

Calahorrano, J. F. J., Lindaas, J., O'Dell, K., Palm, B. B., Peng, Q., Flocke, F., Pollack, I. B., Garofalo, L. A., Farmer, D. K., Pierce, J. R., Collett, J. L., Weinheimer, A., Campos, T., Hornbrook, R. S., Hall, S. R., Ullmann, K., Pothier, M. A., Apel, E. C., Permar, W., … Fischer, E. V. (2021). Daytime Oxidized Reactive Nitrogen Partitioning in Western U.S. Wildfire Smoke Plumes. *Journal of Geophysical Research: Atmospheres*, *126*(4), e2020JD033484. https://doi.org/10.1029/2020JD033484

Campbell, P. C., Tong, D., Saylor, R., Li, Y., Ma, S., Zhang, X., Kondragunta, S., & Li, F. (2022). Pronounced increases in nitrogen emissions and deposition due to the historic 2020 wildfires in the western U.S. *Science of The Total Environment*, *839*, 156130. https://doi.org/10.1016/j.scitotenv.2022.156130

Cao, H., Henze, D. K., Cady-Pereira, K., McDonald, B. C., Harkins, C., Sun, K., Bowman, K. W., Fu, T.-M., & Nawaz, M. O. (2022). COVID-19 Lockdowns Afford the First Satellite-Based Confirmation That Vehicles Are an Under-recognized Source of Urban NH3 Pollution in Los Angeles. *Environmental Science & Technology Letters*, *9*(1), 3–9. https://doi.org/10.1021/acs.estlett.1c00730

Chen, H., Zhang, W., & Sheng, L. (2025). Canadian record-breaking wildfires in 2023 and their impact on US air quality. *Atmospheric Environment*, *342*, 120941. https://doi.org/10.1016/j.atmosenv.2024.120941

Chen, X., Day, D., Schichtel, B., Malm, W., Matzoll, A. K., Mojica, J., McDade, C. E., Hardison, E. D., Hardison, D. L., Walters, S., Van De Water, M., & Collett, J. L. (2014). Seasonal ambient ammonia and ammonium concentrations in a pilot IMPROVE NH*x* monitoring network in the western United States. *Atmospheric Environment*, *91*, 118–126. https://doi.org/10.1016/j.atmosenv.2014.03.058

Cooper, O. R., Chang, K.-L., Bates, K., Brown, S. S., Chace, W. S., Coggon, M. M., Gorchov Negron, A. M., Middlebrook, A. M., Peischl, J., Piasecki, A., Schafer, N., Stockwell, C. E., Wang, S., Warneke, C., Zuraski, K., Miyazaki, K., Payne, V. H., Pennington, E. A., Worden, J. R., … McDonald, B. C. (2024). Early Season 2023 Wildfires Generated Record-Breaking Surface Ozone Anomalies Across the U.S. Upper Midwest. *Geophysical Research Letters*, *51*(22), e2024GL111481. https://doi.org/10.1029/2024GL111481

Darmenov, A. S. (2015). *The Quick Fire Emissions Dataset (QFED): Documentation of Versions 2.1, 2.2 and 2.4: Technical Report Series on Global Modeling and Data*

Assimilation—Volume 38—NASA Technical Reports Server (NTRS). https://ntrs.nasa.gov/citations/20180005253

Du, E., de Vries, W., Galloway, J. N., Hu, X., & Fang, J. (2014). Changes in wet nitrogen deposition in the United States between 1985 and 2012. *Environmental Research Letters*, *9*(9), 095004. https://doi.org/10.1088/1748-9326/9/9/095004

Duan, X., Yan, Y., Peng, L., Xie, K., Hu, D., Li, R., & Wang, C. (2021). Role of ammonia in secondary inorganic aerosols formation at an ammonia-rich city in winter in north China: A comparative study among industry, urban, and rural sites. *Environmental Pollution*, *291*, 118151. https://doi.org/10.1016/j.envpol.2021.118151

Eastham, S., & Fritz, T. (2022). *Technical guidance for the AEIC 2019 aircraft emissions inventory*. http://wiki.seas.harvard.edu/geos-chem/index.php/Aircraft_emissions

Ellis, R. A., Murphy, J. G., Pattey, E., van Haarlem, R., O'Brien, J. M., & Herndon, S. C. (2010). Characterizing a Quantum Cascade Tunable Infrared Laser Differential Absorption Spectrometer (QC-TILDAS) for measurements of atmospheric ammonia. *Atmospheric Measurement Techniques*, *3*(2), 397–406. https://doi.org/10.5194/amt-3-397-2010

Emerson, E. W., Hodshire, A. L., DeBolt, H. M., Bilsback, K. R., Pierce, J. R., McMeeking, G. R., & Farmer, D. K. (2020). Revisiting particle dry deposition and its role in radiative effect estimates. *Proceedings of the National Academy of Sciences*, *117*(42), 26076–26082. https://doi.org/10.1073/pnas.2014761117

Fenn, M. E., Bytnerowicz, A., Schilling, S. L., Vallano, D. M., Zavaleta, E. S., Weiss, S. B., Morozumi, C., Geiser, L. H., & Hanks, K. (2018). On-road emissions of ammonia: An underappreciated source of atmospheric nitrogen deposition. *Science of The Total Environment*, *625*, 909–919. https://doi.org/10.1016/j.scitotenv.2017.12.313

Fenn, M. E., Poth, M. A., Aber, J. D., Baron, J. S., Bormann, B. T., Johnson, D. W., Lemly, A. D., McNulty, S. G., Ryan, D. F., & Stottlemyer, R. (1998). Nitrogen Excess in North American Ecosystems: Predisposing Factors, Ecosystem Responses, and Management Strategies. *Ecological Applications*, *8*(3), 706–733. https://doi.org/10.1890/1051-0761(1998)008%255B0706:NEINAE%255D2.0.CO;2

Flechard, C. R., Spirig, C., Neftel, A., & Ammann, C. (2010). The annual ammonia budget of fertilised cut grassland – Part 2: Seasonal variations and compensation point modeling. *Biogeosciences*, *7*(2), 537–556. https://doi.org/10.5194/bg-7-537-2010

Fountoukis, C., & Nenes, A. (2007). ISORROPIA II: A computationally efficient thermodynamic equilibrium model for K^+&Ca^{2+}&Mg^{2+}&NH_4^+&$Na^+$$SO_4^{2-}$&$NO_3^-$&$Cl^-$&$H_2O$. *Atmospheric Chemistry and Physics*, *7*(17), 4639–4659. https://doi.org/10.5194/acp-7-4639-2007

Fowler, D., Coyle, M., Skiba, U., Sutton, M. A., Cape, J. N., Reis, S., Sheppard, L. J., Jenkins, A., Grizzetti, B., Galloway, J. N., Vitousek, P., Leach, A., Bouwman, A. F., Butterbach-Bahl, K., Dentener, F., Stevenson, D., Amann, M., & Voss, M. (2013). The global nitrogen cycle in the twenty-first century. *Philosophical Transactions of the Royal Society B: Biological Sciences*, *368*(1621), 20130164. https://doi.org/10.1098/rstb.2013.0164

Galloway, J. N., Aber, J. D., Erisman, J. W., Seitzinger, S. P., Howarth, R. W., Cowling, E. B., & Cosby, B. J. (2003). The Nitrogen Cascade. *BioScience*, *53*(4), 341–356. https://doi.org/10.1641/0006-3568(2003)053%255B0341:TNC%255D2.0.CO;2

Geadah, M.-L. (1985). *National inventory of natural and anthropogenic sources and emissions of ammonia (1980)*. Environment Canada, Environmental Protection Service.

Heald, C. L., Collett, J. L. J., Lee, T., Benedict, K. B., Schwandner, F. M., Li, Y., Clarisse, L., Hurtmans, D. R., Van Damme, M., Clerbaux, C., Coheur, P.-F., Philip, S., Martin, R. V., & Pye, H. O. T. (2012). Atmospheric ammonia and particulate inorganic nitrogen over the United States. *Atmospheric Chemistry and Physics*, *12*(21), 10295–10312. https://doi.org/10.5194/acp-12-10295-2012

Holmes, C. D., Bertram, T. H., Confer, K. L., Graham, K. A., Ronan, A. C., Wirks, C. K., & Shah, V. (2019). The Role of Clouds in the Tropospheric NOx Cycle: A New Modeling Approach for Cloud Chemistry and Its Global Implications. *Geophysical Research Letters*, *46*(9), 4980–4990. https://doi.org/10.1029/2019GL081990

Hudman, R. C., Moore, N. E., Mebust, A. K., Martin, R. V., Russell, A. R., Valin, L. C., & Cohen, R. C. (2012). Steps towards a mechanistic model of global soil nitric oxide emissions: Implementation and space based-constraints. *Atmospheric Chemistry and Physics*, *12*(16), 7779–7795. https://doi.org/10.5194/acp-12-7779-2012

Jain, P., Barber, Q. E., Taylor, S. W., Whitman, E., Castellanos Acuna, D., Boulanger, Y., Chavardès, R. D., Chen, J., Englefield, P., Flannigan, M., Girardin, M. P., Hanes, C. C., Little, J., Morrison, K., Skakun, R. S., Thompson, D. K., Wang, X., & Parisien, M.-A. (2024). Drivers and Impacts of the Record-Breaking 2023 Wildfire Season in Canada. *Nature Communications*, *15*(1), 6764. https://doi.org/10.1038/s41467-024-51154-7

Khalek, I. A., Blanks, M. G., Merritt, P. M., & Zielinska, B. (2015). Regulated and unregulated emissions from modern 2010 emissions-compliant heavy-duty on-highway diesel engines. *Journal of the Air & Waste Management Association*, *65*(8), 987–1001. https://doi.org/10.1080/10962247.2015.1051606

Kirchmeier-Young, M. C., Malinina, E., Barber, Q. E., Garcia Perdomo, K., Curasi, S. R., Liang, Y., Jain, P., Gillett, N. P., Parisien, M.-A., Cannon, A. J., Lima, A. R., Arora, V. K., Boulanger, Y., Melton, J. R., Van Vliet, L., & Zhang, X. (2024). Human driven climate change increased the likelihood of the 2023 record area burned in Canada. *Npj Climate and Atmospheric Science*, *7*(1), 316. https://doi.org/10.1038/s41612-024-00841-9

Koplitz, S. N., Nolte, C. G., Sabo, R. D., Clark, C. M., Horn, K. J., Thomas, R. Q., & Newcomer-Johnson, T. A. (2021). The contribution of wildland fire emissions to deposition in the U S: Implications for tree growth and survival in the Northwest. *Environmental Research Letters*, *16*(2), 024028. https://doi.org/10.1088/1748-9326/abd26e

Lana, A., Bell, T. G., Simó, R., Vallina, S. M., Ballabrera-Poy, J., Kettle, A. J., Dachs, J., Bopp, L., Saltzman, E. S., Stefels, J., Johnson, J. E., & Liss, P. S. (2011). An updated climatology of surface dimethlysulfide concentrations and emission fluxes in the global ocean. *Global Biogeochemical Cycles*, *25*(1). https://doi.org/10.1029/2010GB003850

Langford, A. O., Fehsenfeld, F. C., Zachariassen, J., & Schimel, D. S. (1992). Gaseous ammonia fluxes and background concentrations in terrestrial ecosystems of the United States. *Global Biogeochemical Cycles*, *6*(4), 459–483. https://doi.org/10.1029/92GB02123

Lassiter, M. G., Lin, J., Compton, J. E., Phelan, J., Sabo, R. D., Stoddard, J. L., McDow, S. R., & Greaver, T. L. (2023). Shifts in the composition of nitrogen deposition in the conterminous United States are discernable in stream chemistry. *Science of The Total Environment*, *881*, 163409. https://doi.org/10.1016/j.scitotenv.2023.163409

Li, Y., Schichtel, B. A., Walker, J. T., Schwede, D. B., Chen, X., Lehmann, C. M. B., Puchalski, M. A., Gay, D. A., & Collett, J. L. (2016). Increasing importance of deposition of

reduced nitrogen in the United States. *Proceedings of the National Academy of Sciences*, *113*(21), 5874–5879. https://doi.org/10.1073/pnas.1525736113

Li, Y., Schwab, J. J., & Demerjian, K. L. (2006). Measurements of ambient ammonia using a tunable diode laser absorption spectrometer: Characteristics of ambient ammonia emissions in an urban area of New York City. *Journal of Geophysical Research: Atmospheres*, *111*(D10). https://doi.org/10.1029/2005JD006275

Li, Y., Thompson, T. M., Van Damme, M., Chen, X., Benedict, K. B., Shao, Y., Day, D., Boris, A., Sullivan, A. P., Ham, J., Whitburn, S., Clarisse, L., Coheur, P.-F., & Collett Jr., J. L. (2017). Temporal and spatial variability of ammonia in urban and agricultural regions of northern Colorado, United States. *Atmospheric Chemistry and Physics*, *17*(10), 6197–6213. https://doi.org/10.5194/acp-17-6197-2017

Lieb, A. M., Darrouzet-Nardi, A., & Bowman, W. D. (2011). Nitrogen deposition decreases acid buffering capacity of alpine soils in the southern Rocky Mountains. *Geoderma*, *164*(3), 220–224. https://doi.org/10.1016/j.geoderma.2011.06.013

Lill, E. R., Pollack, I. B., Roscioli, J. R., Middlebrook, A. M., Piasecki, A., Albertin, S., Carlson, S., Sullivan, A., Schafer, N., Peischl, J., Rollins, A., Waxman, E. M., Zuraski, K., Gilman, J. B., Treadaway, V., Selby, M., Stockwell, C. E., Coggon, M. M., Bates, K. H., … Fischer, E. V. (2025). Ammonia Observations Over Large North American Cities. *Journal of Geophysical Research: Atmospheres*, *130*(23), e2025JD044019. https://doi.org/10.1029/2025JD044019

Lindaas, J., Pollack, I. B., Calahorrano, J. J., O'Dell, K., Garofalo, L. A., Pothier, M. A., Farmer, D. K., Kreidenweis, S. M., Campos, T., Flocke, F., Weinheimer, A. J., Montzka, D. D., Tyndall, G. S., Apel, E. C., Hills, A. J., Hornbrook, R. S., Palm, B. B., Peng, Q.,

Thornton, J. A., … Fischer, E. V. (2021). Empirical Insights Into the Fate of Ammonia in Western U.S. Wildfire Smoke Plumes. *Journal of Geophysical Research: Atmospheres*, *126*(11), e2020JD033730. https://doi.org/10.1029/2020JD033730

Lindaas, J., Pollack, I. B., Garofalo, L. A., Pothier, M. A., Farmer, D. K., Kreidenweis, S. M., Campos, T. L., Flocke, F., Weinheimer, A. J., Montzka, D. D., Tyndall, G. S., Palm, B. B., Peng, Q., Thornton, J. A., Permar, W., Wielgasz, C., Hu, L., Ottmar, R. D., Restaino, J. C., … Fischer, E. V. (2021). Emissions of Reactive Nitrogen From Western U.S. Wildfires During Summer 2018. *Journal of Geophysical Research: Atmospheres*, *126*(2), e2020JD032657. https://doi.org/10.1029/2020JD032657

Liu, H., Jacob, D. J., Bey, I., & Yantosca, R. M. (2001). Constraints from 210Pb and 7Be on wet deposition and transport in a global three-dimensional chemical tracer model driven by assimilated meteorological fields. *Journal of Geophysical Research: Atmospheres*, *106*(D11), 12109–12128. https://doi.org/10.1029/2000JD900839

Liu, L., Xu, W., Lu, Xiankai, Zhong, B., Guo, Y., Lu, Xiao, Zhao, Y., He, W., Wang, S., Zhang, X., Liu, X., & Vitousek, P. (2022). Exploring global changes in agricultural ammonia emissions and their contribution to nitrogen deposition since 1980. *Proceedings of the National Academy of Sciences*, *119*(14), e2121998119. https://doi.org/10.1073/pnas.2121998119

Liu, L., Zhang, X., Wong, A. Y. H., Xu, W., Liu, X., Li, Y., Mi, H., Lu, X., Zhao, L., Wang, Z., Wu, X., & Wei, J. (2019). Estimating global surface ammonia concentrations inferred from satellite retrievals. *Atmospheric Chemistry and Physics*, *19*(18), 12051–12066. https://doi.org/10.5194/acp-19-12051-2019

Liu, M., Huang, Xin, Song, Y., Tang, J., Cao, J., Zhang, X., Zhang, Q., Wang, S., Xu, T., Kang, L., Cai, X., Zhang, H., Yang, F., Wang, H., Yu, J. Z., Lau, A. K. H., He, L., Huang, Xiaofeng, Duan, L., … Zhu, T. (2019). Ammonia emission control in China would mitigate haze pollution and nitrogen deposition, but worsen acid rain. *Proceedings of the National Academy of Sciences*, *116*(16), 7760–7765. https://doi.org/10.1073/pnas.1814880116

Liu, X., Xu, W., Du, E., Pan, Y., & Goulding, K. (2016). Reduced nitrogen dominated nitrogen deposition in the United States, but its contribution to nitrogen deposition in China decreased. *Proceedings of the National Academy of Sciences*, *113*(26), E3590–E3591. https://doi.org/10.1073/pnas.1607507113

Livingston, C., Rieger, P., & Winer, A. (2009). Ammonia emissions from a representative in-use fleet of light and medium-duty vehicles in the California South Coast Air Basin. *Atmospheric Environment*, *43*(21), 3326–3333. https://doi.org/10.1016/j.atmosenv.2009.04.009

Luo, L., Luo, B., & Tai, A. P. K. (2025). Reactive Nitrogen from Agriculture: A Review of Emissions, Air Quality, and Climate Impacts. *Current Pollution Reports*, *11*(1), 41. https://doi.org/10.1007/s40726-025-00360-y

Ma, J., Shi, H., Zhu, Y., Li, R., Wang, S., Lu, N., Yao, Y., Bian, Z., & Huang, K. (2025). The Evolution of Global Surface Ammonia Concentrations during 2001–2019: Magnitudes, Patterns, and Drivers. *Environmental Science & Technology*, *59*(10), 5066–5079. https://doi.org/10.1021/acs.est.4c14020

Mao, J., Fan, S., Jacob, D. J., & Travis, K. R. (2013). Radical loss in the atmosphere from Cu-Fe redox coupling in aerosols. *Atmospheric Chemistry and Physics*, *13*(2), 509–519. https://doi.org/10.5194/acp-13-509-2013

Marais, E. A., Pandey, A. K., Van Damme, M., Clarisse, L., Coheur, P.-F., Shephard, M. W., Cady-Pereira, K. E., Misselbrook, T., Zhu, L., Luo, G., & Yu, F. (2021). UK Ammonia Emissions Estimated With Satellite Observations and GEOS-Chem. *Journal of Geophysical Research: Atmospheres*, *126*(18), e2021JD035237. https://doi.org/10.1029/2021JD035237

Martin, R. V., Jacob, D. J., Yantosca, R. M., Chin, M., & Ginoux, P. (2003). Global and regional decreases in tropospheric oxidants from photochemical effects of aerosols. *Journal of Geophysical Research: Atmospheres*, *108*(D3). https://doi.org/10.1029/2002JD002622

Massad, R.-S., Nemitz, E., & Sutton, M. A. (2010). Review and parameterisation of bi-directional ammonia exchange between vegetation and the atmosphere. *Atmospheric Chemistry and Physics*, *10*(21), 10359–10386. https://doi.org/10.5194/acp-10-10359-2010

McDuffie, E. E., Fibiger, D. L., Dubé, W. P., Lopez-Hilfiker, F., Lee, B. H., Thornton, J. A., Shah, V., Jaeglé, L., Guo, H., Weber, R. J., Michael Reeves, J., Weinheimer, A. J., Schroder, J. C., Campuzano-Jost, P., Jimenez, J. L., Dibb, J. E., Veres, P., Ebben, C., Sparks, T. L., … Brown, S. S. (2018). Heterogeneous N2O5 Uptake During Winter: Aircraft Measurements During the 2015 WINTER Campaign and Critical Evaluation of Current Parameterizations. *Journal of Geophysical Research: Atmospheres*, *123*(8), 4345–4372. https://doi.org/10.1002/2018JD028336

Meng, J., Martin, R. V., Ginoux, P., Hammer, M., Sulprizio, M. P., Ridley, D. A., & van Donkelaar, A. (2021). Grid-independent high-resolution dust emissions (v1.0) for chemical transport models: Application to GEOS-Chem (12.5.0). *Geoscientific Model Development*, *14*(7), 4249–4260. https://doi.org/10.5194/gmd-14-4249-2021

Mgelwa, A. S., Zhu, F., Huang, D., Song, L., Wang, Y., Gurmesa, G. A., Wang, A., Liu, M., Huang, S., Qiu, Q., Sase, H., Zhu, W., & Fang, Y. (2024). Patterns and drivers of atmospheric inorganic nitrogen deposition in Northeast Asia. *Journal of Environmental Management*, *349*, 119343. https://doi.org/10.1016/j.jenvman.2023.119343

Murray, L. T., Jacob, D. J., Logan, J. A., Hudman, R. C., & Koshak, W. J. (2012). Optimized regional and interannual variability of lightning in a global chemical transport model constrained by LIS/OTD satellite data. *Journal of Geophysical Research: Atmospheres*, *117*(D20). https://doi.org/10.1029/2012JD017934

Nair, A. A., & Yu, F. (2020). Quantification of Atmospheric Ammonia Concentrations: A Review of Its Measurement and Modeling. *Atmosphere*, *11*(10), 1092. https://doi.org/10.3390/atmos11101092

Nair, A. A., Yu, F., & Luo, G. (2019). Spatioseasonal Variations of Atmospheric Ammonia Concentrations Over the United States: Comprehensive Model-Observation Comparison. *Journal of Geophysical Research: Atmospheres*, *124*(12), 6571–6582. https://doi.org/10.1029/2018JD030057

Nemitz, E., Milford, C., & Sutton, M. A. (2001). A two-layer canopy compensation point model for describing bi-directional biosphere-atmosphere exchange of ammonia. *Quarterly Journal of the Royal Meteorological Society*, *127*(573), 815–833. https://doi.org/10.1002/qj.49712757306

Nopmongcol, U., Beardsley, R., Kumar, N., Knipping, E., & Yarwood, G. (2019). Changes in United States deposition of nitrogen and sulfur compounds over five decades from 1970 to 2020. *Atmospheric Environment*, *209*, 144–151. https://doi.org/10.1016/j.atmosenv.2019.04.018

Norman, O. G., Heald, C. L., Bililign, S., Campuzano-Jost, P., Coe, H., Fiddler, M. N., Green, J. R., Jimenez, J. L., Kaiser, K., Liao, J., Middlebrook, A. M., Nault, B. A., Nowak, J. B., Schneider, J., & Welti, A. (2025). Exploring the processes controlling secondary inorganic aerosol: Evaluating the global GEOS-Chem simulation using a suite of aircraft campaigns. *Atmospheric Chemistry and Physics*, *25*(2), 771–795. https://doi.org/10.5194/acp-25-771-2025

Nowak, J. B., Neuman, J. A., Bahreini, R., Middlebrook, A. M., Holloway, J. S., McKeen, S. A., Parrish, D. D., Ryerson, T. B., & Trainer, M. (2012). Ammonia sources in the California South Coast Air Basin and their impact on ammonium nitrate formation. *Geophysical Research Letters*, *39*(7). https://doi.org/10.1029/2012GL051197

Park, R. J., Jacob, D. J., Field, B. D., Yantosca, R. M., & Chin, M. (2004). Natural and transboundary pollution influences on sulfate-nitrate-ammonium aerosols in the United States: Implications for policy. *Journal of Geophysical Research: Atmospheres*, *109*(D15). https://doi.org/10.1029/2003JD004473

Pinder, R. W., Gilliland, A. B., & Dennis, R. L. (2008). Environmental impact of atmospheric NH3 emissions under present and future conditions in the eastern United States. *Geophysical Research Letters*, *35*(12). https://doi.org/10.1029/2008GL033732

Pleim, J. E., Ran, L., Appel, W., Shephard, M. W., & Cady-Pereira, K. (2019). New Bidirectional Ammonia Flux Model in an Air Quality Model Coupled With an

Agricultural Model. *Journal of Advances in Modeling Earth Systems*, *11*(9), 2934–2957. https://doi.org/10.1029/2019MS001728

Pollack, I. B., Lindaas, J., Roscioli, J. R., Agnese, M., Permar, W., Hu, L., & Fischer, E. V. (2019). Evaluation of ambient ammonia measurements from a research aircraft using a closed-path QC-TILDAS operated with active continuous passivation. *Atmospheric Measurement Techniques*, *12*(7), 3717–3742. https://doi.org/10.5194/amt-12-3717-2019

Pope, C. A., Ezzati, M., & Dockery, D. W. (2009). Fine-particulate air pollution and life expectancy in the United States. *The New England Journal of Medicine*, *360*(4), 376–386. https://doi.org/10.1056/NEJMsa0805646

Pye, H. O. T., Liao, H., Wu, S., Mickley, L. J., Jacob, D. J., Henze, D. K., & Seinfeld, J. H. (2009). Effect of changes in climate and emissions on future sulfate-nitrate-ammonium aerosol levels in the United States. *Journal of Geophysical Research: Atmospheres*, *114*(D1). https://doi.org/10.1029/2008JD010701

Reche, C., Pérez, N., Alastuey, A., Cots, N., Pérez, E., & Querol, X. (2022). 2011–2020 trends of urban and regional ammonia in and around Barcelona, NE Spain. *Chemosphere*, *304*, 135347. https://doi.org/10.1016/j.chemosphere.2022.135347

Reche, C., Viana, M., Pandolfi, M., Alastuey, A., Moreno, T., Amato, F., Ripoll, A., & Querol, X. (2012). Urban NH3 levels and sources in a Mediterranean environment. *Atmospheric Environment*, *57*, 153–164. https://doi.org/10.1016/j.atmosenv.2012.04.021

Roscioli, J. R., Zahniser, M. S., Nelson, D. D., Herndon, S. C., & Kolb, C. E. (2016). New Approaches to Measuring Sticky Molecules: Improvement of Instrumental Response Times Using Active Passivation. *The Journal of Physical Chemistry A*, *120*(9), 1347–1357. https://doi.org/10.1021/acs.jpca.5b04395

Salcedo, D., Tao, Y., Wizenberg, T., Jones, D., & Murphy, J. (2025). Simultaneous Gas and Particle Phase Measurements Facilitate the Understanding of Ammonia's Atmospheric Budget. *Journal of Geophysical Research: Atmospheres*, *130*(13), e2025JD043435. https://doi.org/10.1029/2025JD043435

Saylor, R., Myles, L., Sibble, D., Caldwell, J., & Xing, J. (2015). Recent trends in gas-phase ammonia and PM2.5 ammonium in the Southeast United States. *Journal of the Air & Waste Management Association*, *65*(3), 347–357. https://doi.org/10.1080/10962247.2014.992554

Shephard, M. W., & Cady-Pereira, K. E. (2015). Cross-track Infrared Sounder (CrIS) satellite observations of tropospheric ammonia. *Atmospheric Measurement Techniques*, *8*(3), 1323–1336. https://doi.org/10.5194/amt-8-1323-2015

Sun, K., Tao, L., Miller, D. J., Khan, M. A., & Zondlo, M. A. (2014). On-Road Ammonia Emissions Characterized by Mobile, Open-Path Measurements. *Environmental Science & Technology*, *48*(7), 3943–3950. https://doi.org/10.1021/es4047704

Sun, K., Tao, L., Miller, D. J., Pan, D., Golston, L. M., Zondlo, M. A., Griffin, R. J., Wallace, H. W., Leong, Y. J., Yang, M. M., Zhang, Y., Mauzerall, D. L., & Zhu, T. (2017). Vehicle Emissions as an Important Urban Ammonia Source in the United States and China. *Environmental Science & Technology*, *51*(4), 2472–2481. https://doi.org/10.1021/acs.est.6b02805

Sutton, M. A., Milford, C., Dragosits, U., Place, C. J., Singles, R. J., Smith, R. I., Pitcairn, C. E. R., Fowler, D., Hill, J., ApSimon, H. M., Ross, C., Hill, R., Jarvis, S. C., Pain, B. F., Phillips, V. C., Harrison, R., Moss, D., Webb, J., Espenhahn, S. E., … Wyers, G. P. (1998). Dispersion, deposition and impacts of atmospheric ammonia: Quantifying local

budgets and spatial variability. *Environmental Pollution, Nitrogen, the Confer-N-s First International Nitrogen Conference 1998*, *102*(1, Supplement 1), 349–361. https://doi.org/10.1016/S0269-7491(98)80054-7

Tang, Y. S., Braban, C. F., Dragosits, U., Dore, A. J., Simmons, I., van Dijk, N., Poskitt, J., Dos Santos Pereira, G., Keenan, P. O., Conolly, C., Vincent, K., Smith, R. I., Heal, M. R., & Sutton, M. A. (2018). Drivers for spatial, temporal and long-term trends in atmospheric ammonia and ammonium in the UK. *Atmospheric Chemistry and Physics*, *18*(2), 705–733. https://doi.org/10.5194/acp-18-705-2018

Teng, X., Hu, Q., Zhang, L., Qi, J., Shi, J., Xie, H., Gao, H., & Yao, X. (2017). Identification of Major Sources of Atmospheric NH3 in an Urban Environment in Northern China During Wintertime. *Environmental Science & Technology*, *51*(12), 6839–6848. https://doi.org/10.1021/acs.est.7b00328

Tong, D. Q., Lamsal, L., Pan, L., Ding, C., Kim, H., Lee, P., Chai, T., Pickering, K. E., & Stajner, I. (2015). Long-term NOx trends over large cities in the United States during the great recession: Comparison of satellite retrievals, ground observations, and emission inventories. *Atmospheric Environment*, *107*, 70–84. https://doi.org/10.1016/j.atmosenv.2015.01.035

Toro, C., Sonntag, D., Bash, J., Burke, G., Murphy, B. N., Seltzer, K. M., Simon, H., Shephard, M. W., & Cady-Pereira, K. E. (2024). Sensitivity of air quality to vehicle ammonia emissions in the United States. *Atmospheric Environment*, *327*, 120484. https://doi.org/10.1016/j.atmosenv.2024.120484

US EPA. (2004). *Estimating Ammonia Emissions from Anthropogenic Nonagricultural Sources*. https://www.epa.gov/sites/production/files/2015-08/documents/eiip_areasourcesnh3.pdf

US EPA. (2019, October 1). *2016v1 Platform* [Other Policies and Guidance]. https://www.epa.gov/air-emissions-modeling/2016v1-platform

US EPA, O. (2023a). *2020 National Emissions Inventory (NEI) Data* [Other Policies and Guidance]. https://www.epa.gov/air-emissions-inventories/2020-national-emissions-inventory-nei-data

US EPA, O. (2023b, January 13). *2020 National Emissions Inventory (NEI) Technical Support Document (TSD)* [Other Policies and Guidance]. https://www.epa.gov/air-emissions-inventories/2020-national-emissions-inventory-nei-technical-support-document-tsd

Van Damme, M., Clarisse, L., Whitburn, S., Hadji-Lazaro, J., Hurtmans, D., Clerbaux, C., & Coheur, P.-F. (2018). Industrial and agricultural ammonia point sources exposed. *Nature*, *564*(7734), 99–103. https://doi.org/10.1038/s41586-018-0747-1

von Bobrutzki, K., Braban, C. F., Famulari, D., Jones, S. K., Blackall, T., Smith, T. E. L., Blom, M., Coe, H., Gallagher, M., Ghalaieny, M., McGillen, M. R., Percival, C. J., Whitehead, J. D., Ellis, R., Murphy, J., Mohacsi, A., Pogany, A., Junninen, H., Rantanen, S., … Nemitz, E. (2010). Field inter-comparison of eleven atmospheric ammonia measurement techniques. *Atmospheric Measurement Techniques*, *3*(1), 91–112. https://doi.org/10.5194/amt-3-91-2010

Walker, J. M., Philip, S., Martin, R. V., & Seinfeld, J. H. (2012). Simulation of nitrate, sulfate, and ammonium aerosols over the United States. *Atmospheric Chemistry and Physics*, *12*(22), 11213–11227. https://doi.org/10.5194/acp-12-11213-2012

Walters, W. W., Karod, M., Willcocks, E., Baek, B. H., Blum, D. E., & Hastings, M. G. (2022). Quantifying the importance of vehicle ammonia emissions in an urban area of

northeastern USA utilizing nitrogen isotopes. *Atmospheric Chemistry and Physics*, *22*(20), 13431–13448. https://doi.org/10.5194/acp-22-13431-2022

Walters, W. W., Song, L., Chai, J., Fang, Y., Colombi, N., & Hastings, M. G. (2020). Characterizing the spatiotemporal nitrogen stable isotopic composition of ammonia in vehicle plumes. *Atmospheric Chemistry and Physics*, *20*(19), 11551–11567. https://doi.org/10.5194/acp-20-11551-2020

Wang, Q., Jacob, D. J., Fisher, J. A., Mao, J., Leibensperger, E. M., Carouge, C. C., Le Sager, P., Kondo, Y., Jimenez, J. L., Cubison, M. J., & Doherty, S. J. (2011). Sources of carbonaceous aerosols and deposited black carbon in the Arctic in winter-spring: Implications for radiative forcing. *Atmospheric Chemistry and Physics*, *11*(23), 12453–12473. https://doi.org/10.5194/acp-11-12453-2011

Wang, Q., Jacob, D. J., Spackman, J. R., Perring, A. E., Schwarz, J. P., Moteki, N., Marais, E. A., Ge, C., Wang, J., & Barrett, S. R. H. (2014). Global budget and radiative forcing of black carbon aerosol: Constraints from pole-to-pole (HIPPO) observations across the Pacific. *Journal of Geophysical Research: Atmospheres*, *119*(1), 195–206. https://doi.org/10.1002/2013JD020824

Wang, Y., Jacob, D. J., & Logan, J. A. (1998). Global simulation of tropospheric O3-NO x - hydrocarbon chemistry: 1. Model formulation. *Journal of Geophysical Research: Atmospheres*, *103*(D9), 10713–10725. https://doi.org/10.1029/98JD00158

Wang, Zhe, Wang, Zifa, Zou, Z., Chen, X., Wu, H., Wang, W., Su, H., Li, F., Xu, W., Liu, Z., & Zhu, J. (2024). Severe Global Environmental Issues Caused by Canada's Record-Breaking Wildfires in 2023. *Advances in Atmospheric Sciences*, *41*(4), 565–571. https://doi.org/10.1007/s00376-023-3241-0

Wen, Z., Ma, X., Xu, W., Si, R., Liu, L., Ma, M., Zhao, Yuanhong, Tang, A., Zhang, Yangyang, Wang, K., Zhang, Ying, Shen, J., Zhang, L., Zhao, Yu, Zhang, F., Goulding, K., & Liu, X. (2024). Combined short-term and long-term emission controls improve air quality sustainably in China. *Nature Communications*, *15*(1), 5169. https://doi.org/10.1038/s41467-024-49539-9

Wesely, M. L. (1989). Parameterization of surface resistances to gaseous dry deposition in regional-scale numerical models. *Atmospheric Environment (1967)*, *23*(6), 1293–1304. https://doi.org/10.1016/0004-6981(89)90153-4

Wichink Kruit, R. J. (Roy), van Pul, W. A. J., Otjes, R. P., Hofschreuder, P., Jacobs, A. F. G., & Holtslag, A. A. M. (2007). Ammonia fluxes and derived canopy compensation points over non-fertilized agricultural grassland in The Netherlands using the new gradient ammonia—High accuracy—Monitor (GRAHAM). *Atmospheric Environment*, *41*(6), 1275–1287. https://doi.org/10.1016/j.atmosenv.2006.09.039

Wolfe, A. P., Baron, J. S., & Cornett, R. J. (2001). Anthropogenic nitrogen deposition induces rapid ecological changes in alpine lakes of the Colorado Front Range (USA). *Journal of Paleolimnology*, *25*(1), 1–7. https://doi.org/10.1023/A:1008129509322

Wolfe, A. P., Van Gorp, A. C., & Baron, J. S. (2003). Recent ecological and biogeochemical changes in alpine lakes of Rocky Mountain National Park (Colorado, USA): A response to anthropogenic nitrogen deposition. *Geobiology*, *1*(2), 153–168. https://doi.org/10.1046/j.1472-4669.2003.00012.x

Wyer, K. E., Kelleghan, D. B., Blanes-Vidal, V., Schauberger, G., & Curran, T. P. (2022). Ammonia emissions from agriculture and their contribution to fine particulate matter: A

review of implications for human health. *Journal of Environmental Management*, *323*, 116285. https://doi.org/10.1016/j.jenvman.2022.116285

Yao, X., & Zhang, L. (2016). Trends in atmospheric ammonia at urban, rural, and remote sites across North America. *Atmospheric Chemistry and Physics*, *16*(17), 11465–11475. https://doi.org/10.5194/acp-16-11465-2016

Yu, X., Zhou, M., Li, J., Qiao, L., Lou, S., Han, W., Zhang, Z., Huang, C., & Yu, J. Z. (2023). First Online Observation of Aerosol Total Organic Nitrogen at an Urban Site: Insights Into the Emission Sources and Formation Pathways of Nitrogenous Organic Aerosols. *Journal of Geophysical Research: Atmospheres*, *128*(19), e2023JD038921. https://doi.org/10.1029/2023JD038921

Zeng, Y., Tian, S., & Pan, Y. (2018). Revealing the Sources of Atmospheric Ammonia: A Review. *Current Pollution Reports*, *4*(3), 189–197. https://doi.org/10.1007/s40726-018-0096-6

Zhan, X., Bo, Y., Zhou, F., Liu, X., Paerl, H. W., Shen, J., Wang, R., Li, F., Tao, S., Dong, Y., & Tang, X. (2017). Evidence for the Importance of Atmospheric Nitrogen Deposition to Eutrophic Lake Dianchi, China. *Environmental Science & Technology*, *51*(12), 6699–6708. https://doi.org/10.1021/acs.est.6b06135

Zhang, L., Gong, S., Padro, J., & Barrie, L. (2001). A size-segregated particle dry deposition scheme for an atmospheric aerosol module. *Atmospheric Environment*, *35*(3), 549–560. https://doi.org/10.1016/S1352-2310(00)00326-5

Zhang, L., Jacob, D. J., Knipping, E. M., Kumar, N., Munger, J. W., Carouge, C. C., van Donkelaar, A., Wang, Y. X., & Chen, D. (2012). Nitrogen deposition to the United

States: Distribution, sources, and processes. *Atmospheric Chemistry and Physics*, *12*(10), 4539–4554. https://doi.org/10.5194/acp-12-4539-2012

Zhang, L., Wright, L. P., & Asman, W. a. H. (2010). Bi-directional air-surface exchange of atmospheric ammonia: A review of measurements and a development of a big-leaf model for applications in regional-scale air-quality models. *Journal of Geophysical Research: Atmospheres*, *115*(D20). https://doi.org/10.1029/2009JD013589

Zhang, Q., Wang, Y., Xiao, Q., Geng, G., Davis, S. J., Liu, X., Yang, J., Liu, J., Huang, W., He, C., Luo, B., Martin, R. V., Brauer, M., Randerson, J. T., & He, K. (2025). Long-range PM2.5 pollution and health impacts from the 2023 Canadian wildfires. *Nature*, 1–7. https://doi.org/10.1038/s41586-025-09482-1

Zhang, Y., Mathur, R., Bash, J. O., Hogrefe, C., Xing, J., & Roselle, S. J. (2018). Long-term trends in total inorganic nitrogen and sulfur deposition in the US from 1990 to 2010. *Atmospheric Chemistry and Physics*, *18*(12), 9091–9106. https://doi.org/10.5194/acp-18-9091-2018

Zhang, Z., Zeng, Y., Zheng, N., Luo, L., Xiao, Hongwei, & Xiao, Huayun. (2020). Fossil fuel-related emissions were the major source of NH3 pollution in urban cities of northern China in the autumn of 2017. *Environmental Pollution*, *256*, 113428. https://doi.org/10.1016/j.envpol.2019.113428

Zhou, C., Zhou, H., Holsen, T. M., Hopke, P. K., Edgerton, E. S., & Schwab, J. J. (2019). Ambient Ammonia Concentrations Across New York State. *Journal of Geophysical Research: Atmospheres*, *124*(14), 8287–8302. https://doi.org/10.1029/2019JD030380

Zhu, L., Henze, D., Bash, J., Jeong, G.-R., Cady-Pereira, K., Shephard, M., Luo, M., Paulot, F., & Capps, S. (2015). Global evaluation of ammonia bidirectional exchange and livestock

diurnal variation schemes. *Atmospheric Chemistry and Physics*, *15*(22), 12823–12843. https://doi.org/10.5194/acp-15-12823-2015

Zhu, L., Henze, D. K., Cady-Pereira, K. E., Shephard, M. W., Luo, M., Pinder, R. W., Bash, J. O., & Jeong, G.-R. (2013). Constraining U.S. ammonia emissions using TES remote sensing observations and the GEOS-Chem adjoint model. *Journal of Geophysical Research: Atmospheres*, *118*(8), 3355–3368. https://doi.org/10.1002/jgrd.50166

Zou, X., Wang, S., Liu, J., Zhu, J., Zhang, S., Xue, R., Gu, C., & Zhou, B. (2024). Role of gas-particle conversion of ammonia in haze pollution under ammonia-rich environment in Northern China and prospects of effective emission reduction. *Science of The Total Environment*, *934*, 173277. https://doi.org/10.1016/j.scitotenv.2024.173277

APPENDIX A

SUPPLEMENTAL INFORMATION FOR CHAPTER 2

Table A1: Table of flight date, location, HMS plume present, and mean CH_3CN mixing ratio for individual flights.

Date	Location	HMS Plume Present	Mean Acetonitrile (ppt)
7/28/23	NYC	Medium	166
8/1/23	Chicago	Medium	199
8/2/23	Chicago	Light	215
8/4/23	Toronto	Medium	402
8/5/23	Toronto	Medium	240
8/8/23	Chicago	No	282
8/9/23	NYC	Heavy	218
8/12/23	Chicago	No	174
8/15/23	Chicago	Light	253
8/16/23	NYC	Light	139
8/23/23	LA	No	106
8/25/23	LA	No	111
8/26/23	LA	No	102

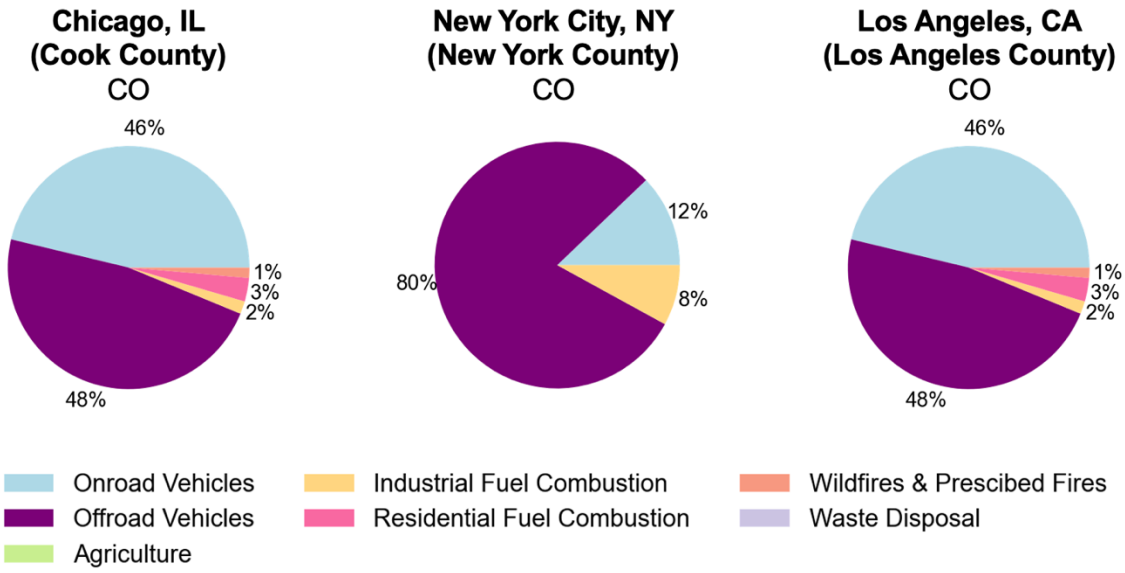

Figure A1: 2020 NH_3 emissions by sector for Chicago, NYC, and LA (US EPA, 2023).

APPENDIX B

SUPPLEMENTAL INFORMATION FOR CHAPTER 3

Table B1: PILS and AMS NH_x ratios for NYC, LA, and Chicago with the associated r^2 value. The Chicago ratios are from the downwind leg. There are no PILS ratios from Chicago as there were too few data points.

City	PILS NH_x:CO Ratio	AMS NH_x:CO Ratio	PILS NH_x:NO_x Ratio	AMS NH_x:NO_x Ratio	PILS NH_x:NO_y Ratio	AMS NH_x:NO_y Ratio
NYC (16 August)	0.020 ± 0.004; $r^2 = 0.65$	0.043 ± 0.001; $r^2 = 0.92$	0.257 ± 0.075; $r^2 = 0.66$	0.472 ± 0.143; $r^2 = 0.85$	0.115 ± 0.024; $r^2 = 0.76$	0.269 ± 0.006; $r^2 = 0.92$
LA (Average of 23, 25, & 26 August)	0.038 ± 0.002; $r^2 = 0.93$	0.046 ± 0.001; $r^2 = 0.85$	0.936 ± 0.172; $r^2 = 0.77$	1.19 ± 0.030; $r^2 = 0.67$	0.51 ± 0.084; $r^2 = 0.81$	0.687 ± 0.011; r^2 =0.86
Chicago (01 August)	N/A	0.069 ± 0.002; $r^2 = 0.75$	N/A	0.357 ± 0.028; $r^2 = 0.57$	N/A	0.297 ± 0.158; $r^2 = 0.65$
Chicago (12 August)	N/A	0.030 ± 0.004; $r^2 = 0.94$	N/A	0.774 ± 0.094; $r^2 = 0.89$	N/A	0.188 ± 0.028; $r^2 = 0.95$

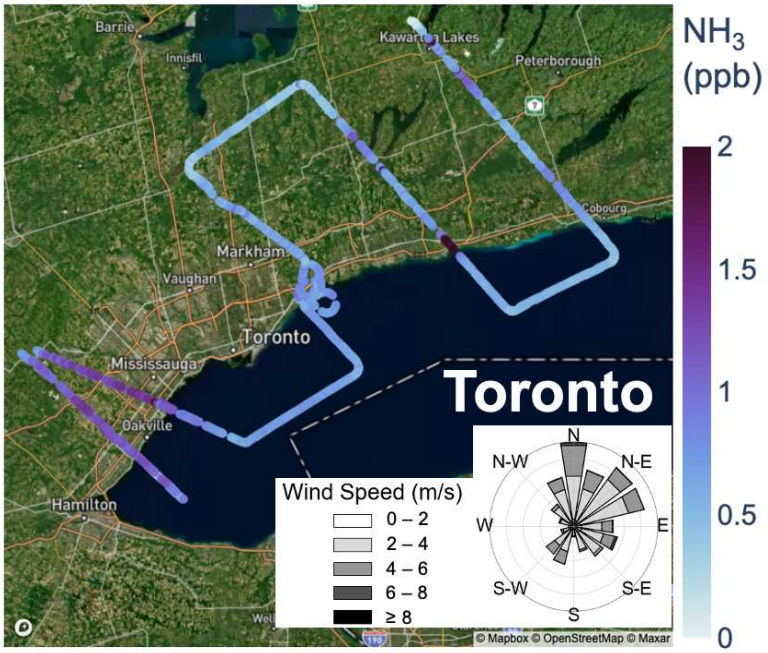

Figure B1: Example flight track for Toronto (05 Aug. 2023): (43.3 – 44.4°N); (279.7 – 281.9 °W) colored by NH_3 mixing ratio.

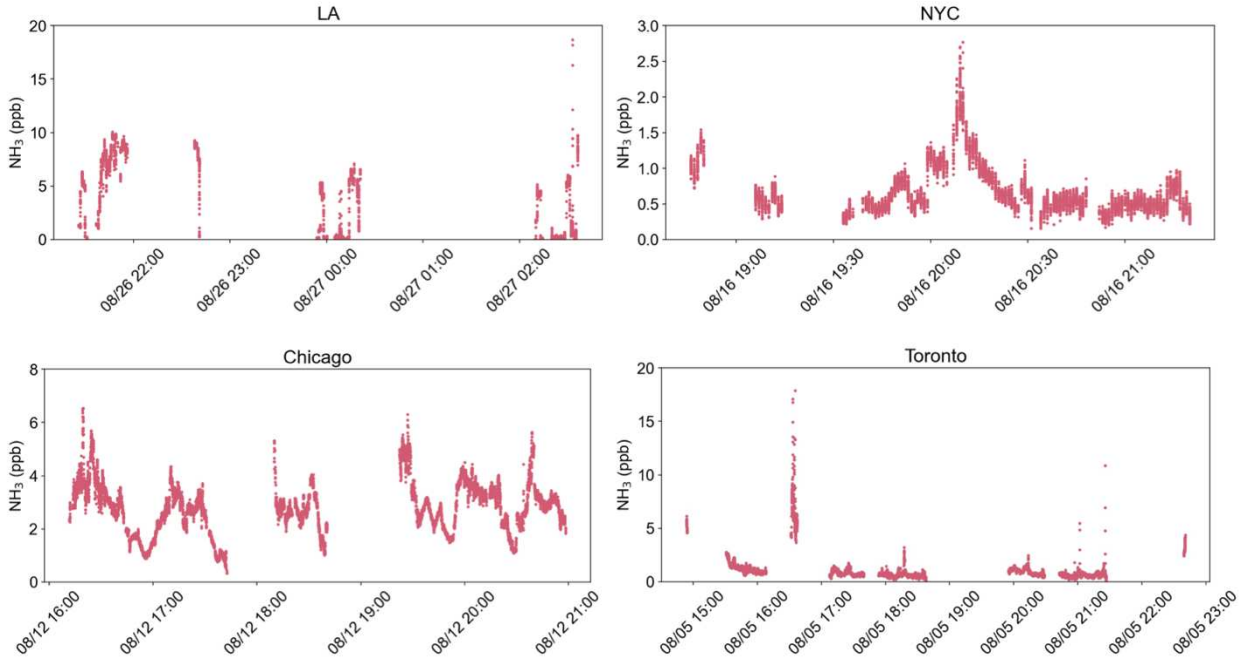

Figure B2: Time series for the data presented for each city in Figure 2.1, in the main manuscript, and Figure B1 utilizing the same latitude, longitude, and altitude bounding.

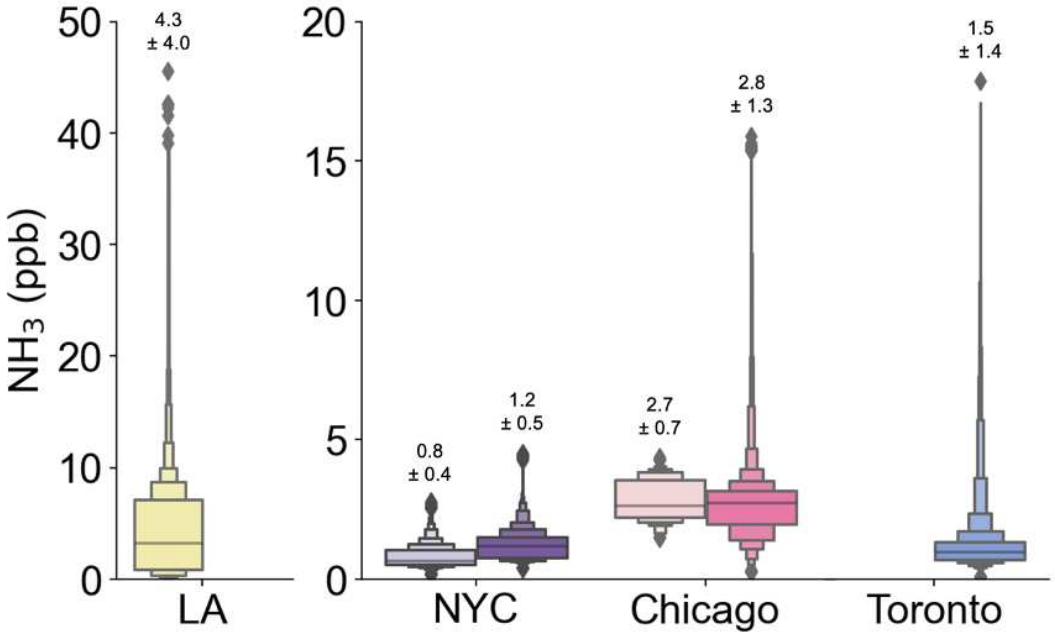

Figure B3: Boxplots of NH3 observed over LA, NYC, and Chicago, and Toronto under smoke-impacted (darker color) and low/no smoke (lighter color) conditions. LA only experienced low/no smoke conditions and Toronto only experienced smoke-impacted conditions during the AEROMMA sampling periods. The large box in the center of each boxplot represents the median (middle line) and the fourths on each side of the median. The following smaller boxes represent eighths, sixteenths, etc. The numbers above each boxplot represent the mean NH3 mixing ratio and the 1-sigma standard deviation.

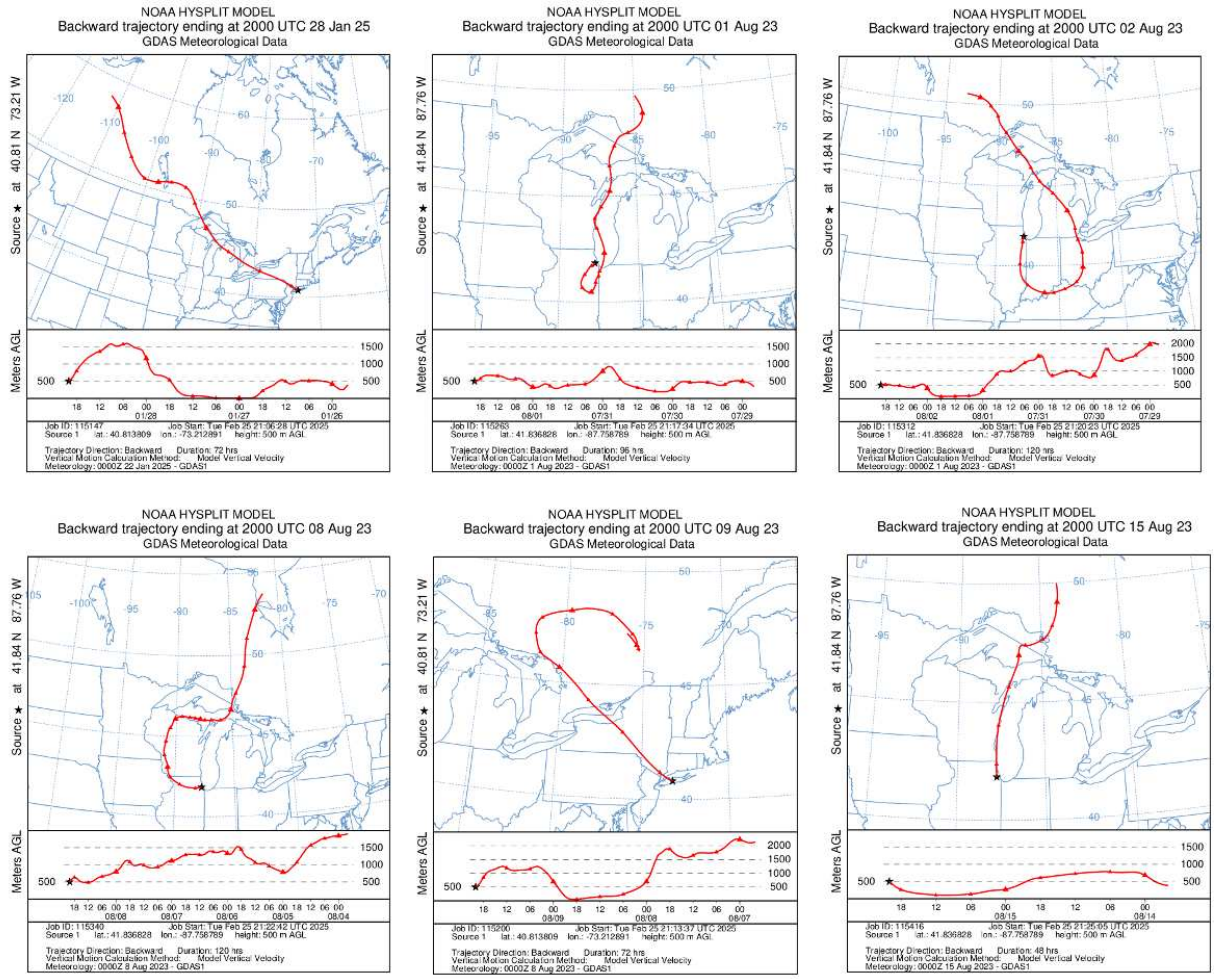

Figure B4: Hysplit Trajectories for smoke impacted days in NYC and Chicago.

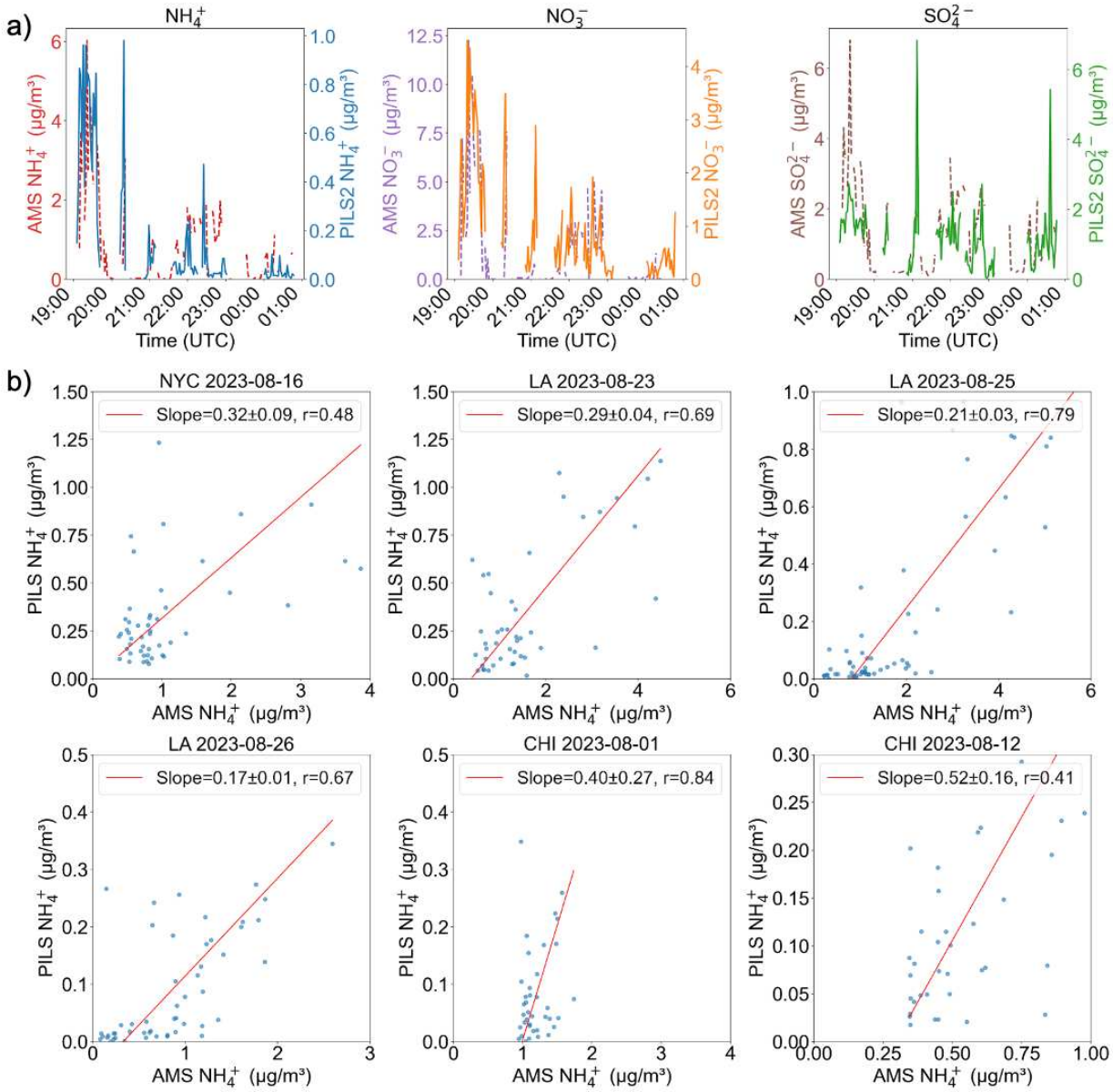

Figure B5: a) Timeseries of NH_4^+, NO_3^-, and SO_4^{2-} from the PILS and AMS in LA on 25 August 2023 and b) scatter plots of AMS NH_4^+ and PILS NH_4^+ with the RMA regression lines for each flight used in this study.

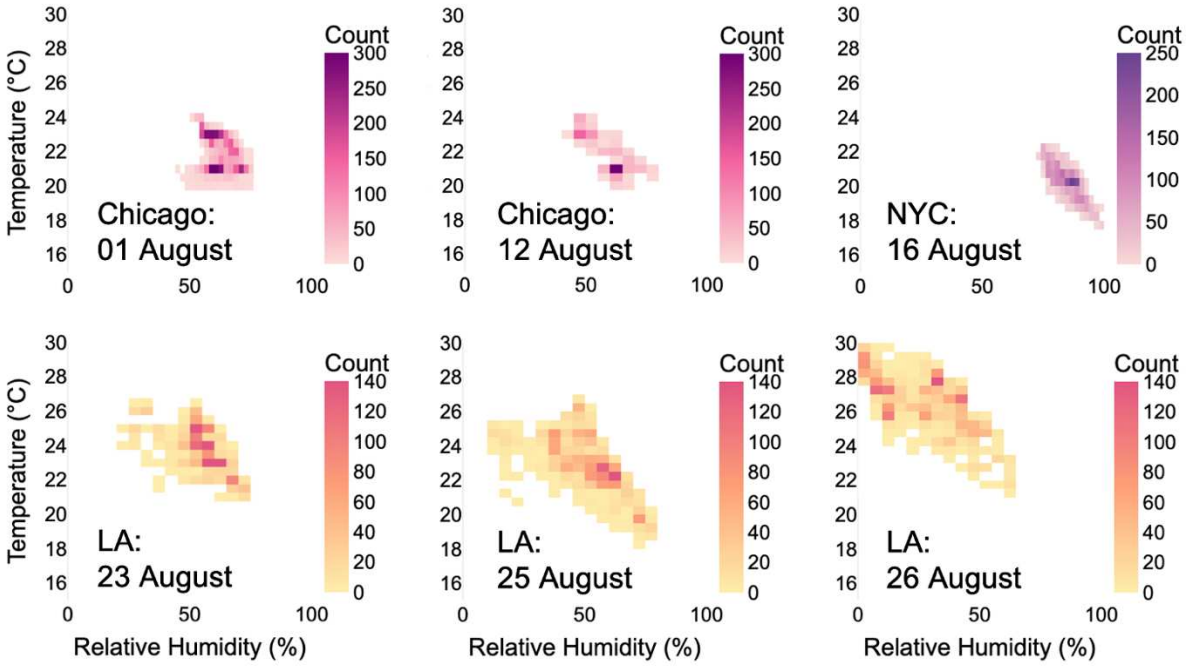

Figure B6: Heatmaps of relative humidity versus temperature for each flight shown in Figure 3.2 in the main text.

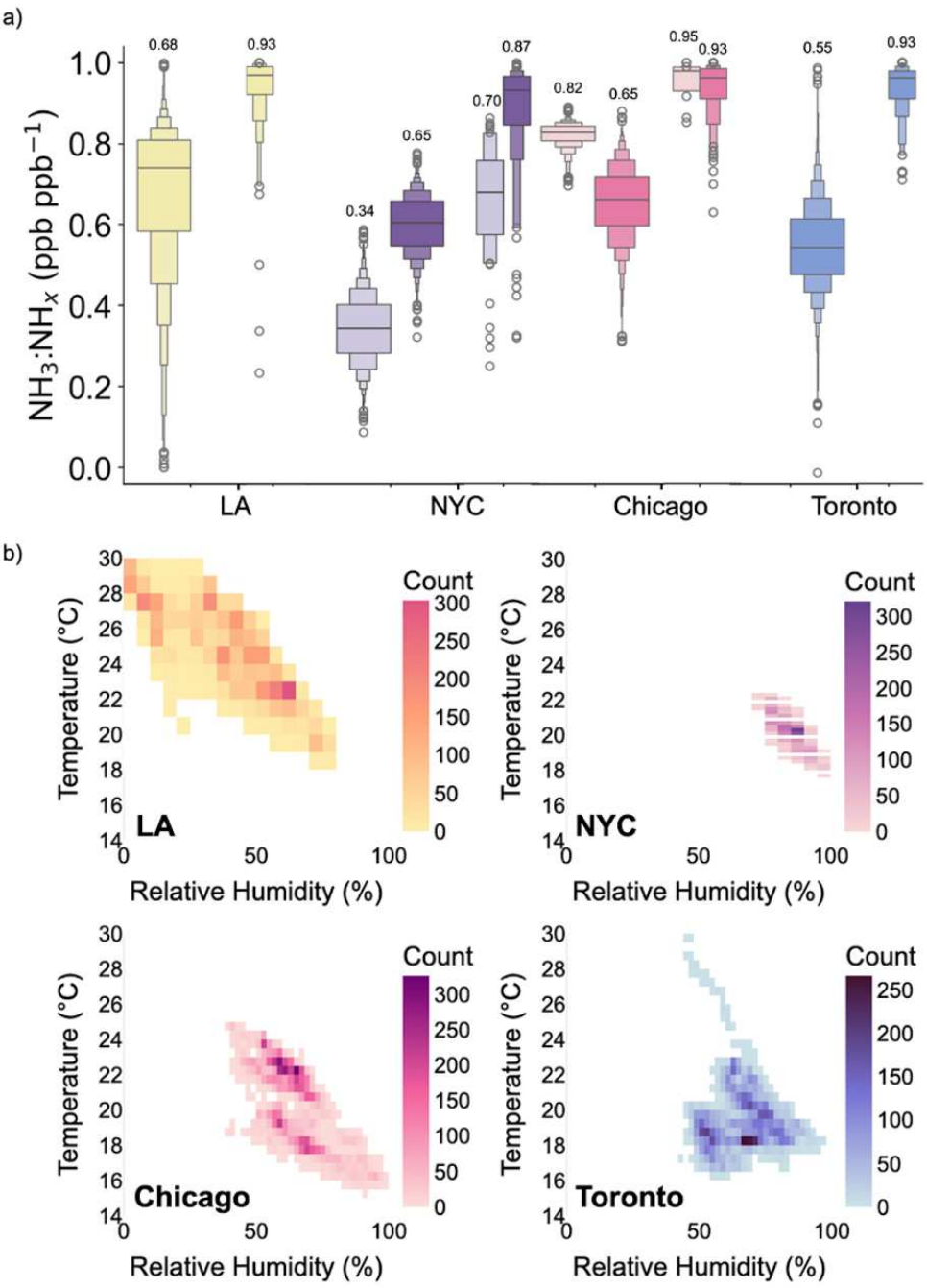

Figure B7: a) Boxplots of the boundary layer NH_3:NH_x ratio in LA, NYC, Chicago, and Toronto under smoke-impacted (darker color) and low/no smoke (lighter color) conditions with NH_4^+ data from the AMS (wider plots) and the PILS (thinner plots). The numbers above each boxplot represent the mean NH_3:NH_x ratio. A NH_3:NH_x ratio close to zero indicates that a majority of the NH_x is in the particle-phase (NH_4), while a NH_3:NH_x ratio close to one indicates that a majority of the NH_x is in the gas-phase (NH_3), and b) heatmaps of relative humidity versus temperature for all flights in each city.

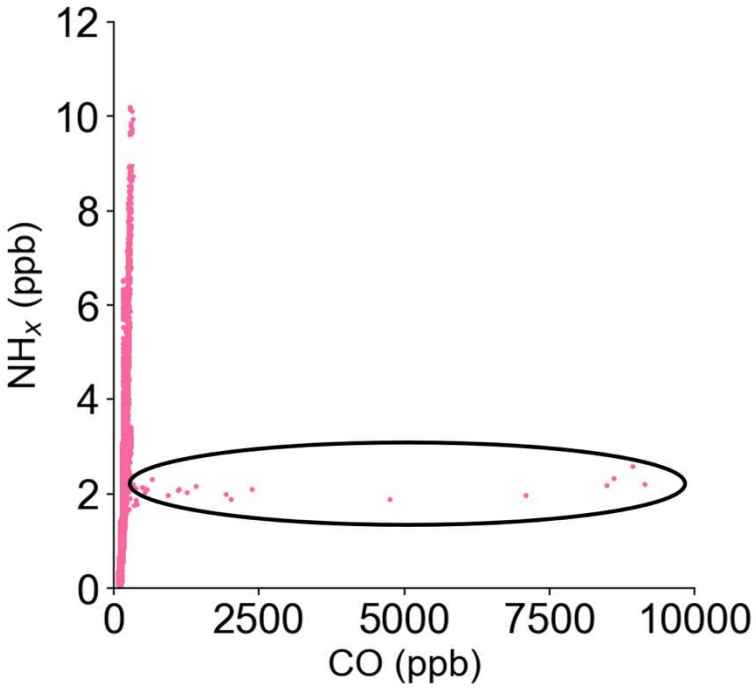

Figure B8: AMS NH_x:CO ratio for the 16 August 2023 NYC flight with the Northport Power Station included and circled.

Figure B9: Map of NYC on 16 August 2023 overlaid with flight track colored by NH3. The grey box represents the region directly overhead NYC and the white box represents the region north of NYC.

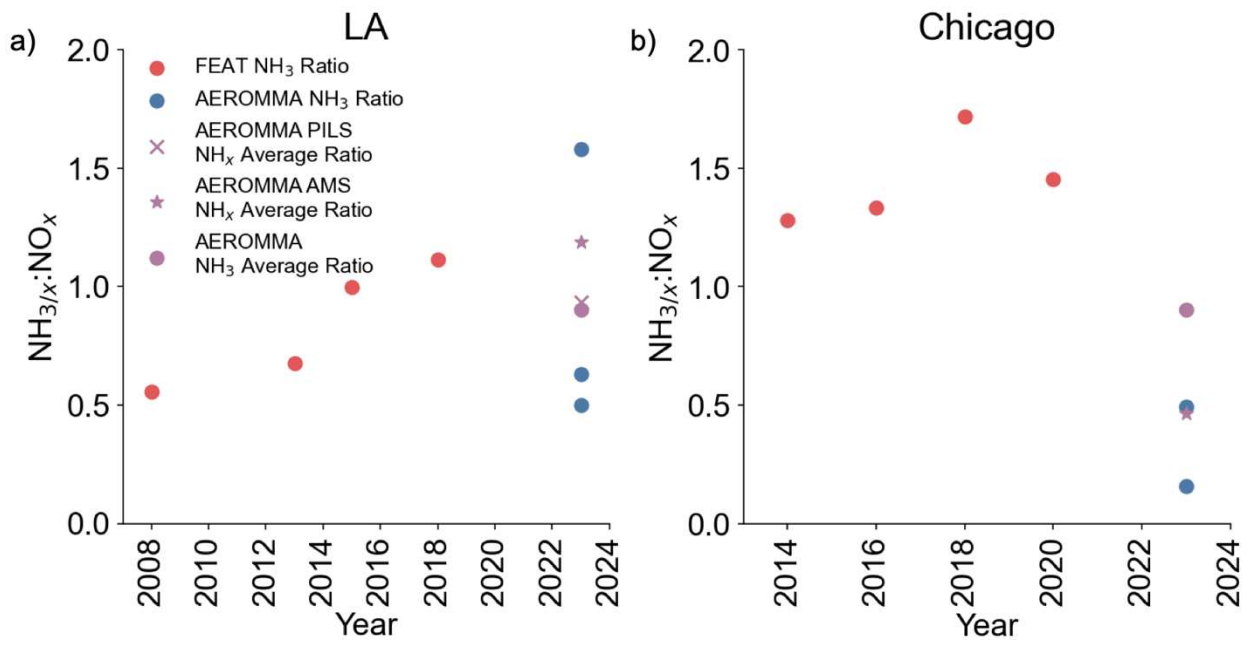

Figure B10: $NH_{3/X}$:CO ratios from the fuel efficiency automobile test (FEAT) publications for past years in a) LA and b) Chicago plotted with ratios from AEROMMA (G. Bishop, 2019, 2021; G. Bishop et al., 2010).

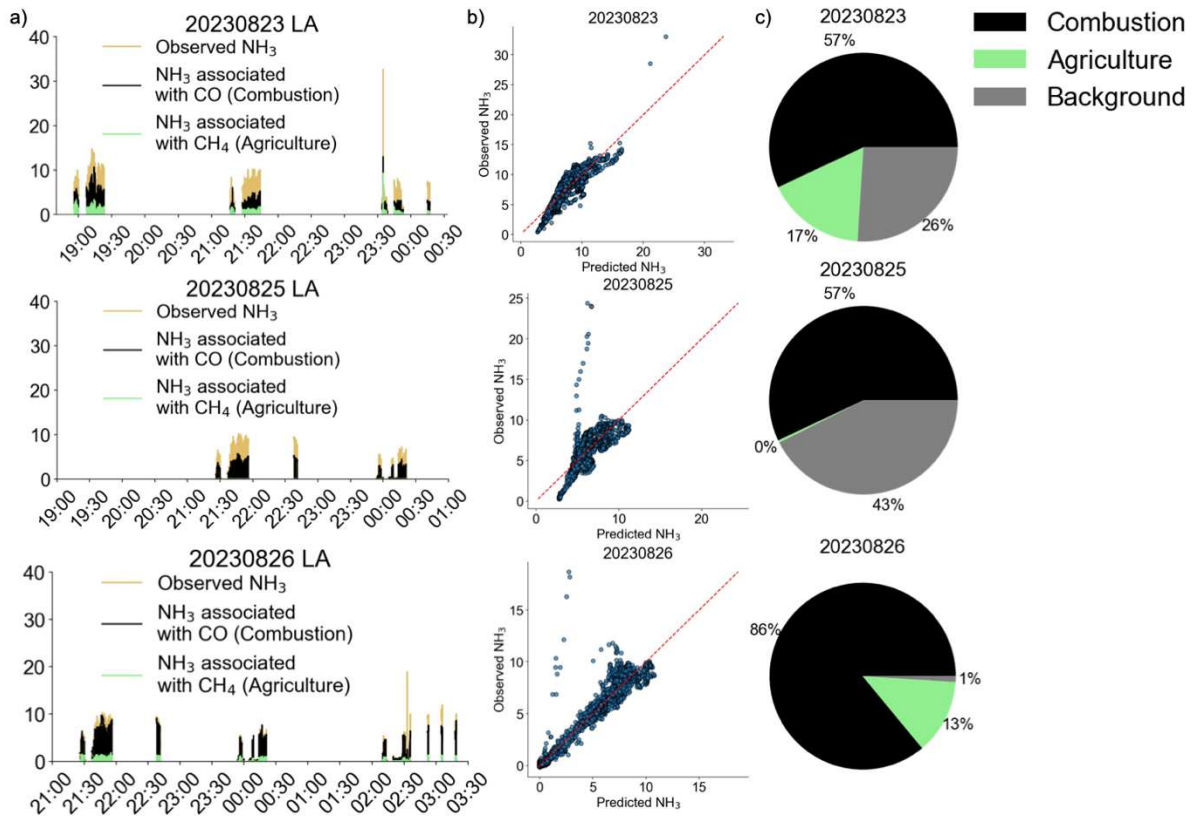

Figure B11: a) Timeseries of multivariate linear regression (MLR) results for each LA flight, b) NH_3 predicted by MLR v. observed NH_3 for each LA flight, and c) pie charts of average fractional contribution of NH_3 associated with combustion (CO), agriculture (CH_4), and background.

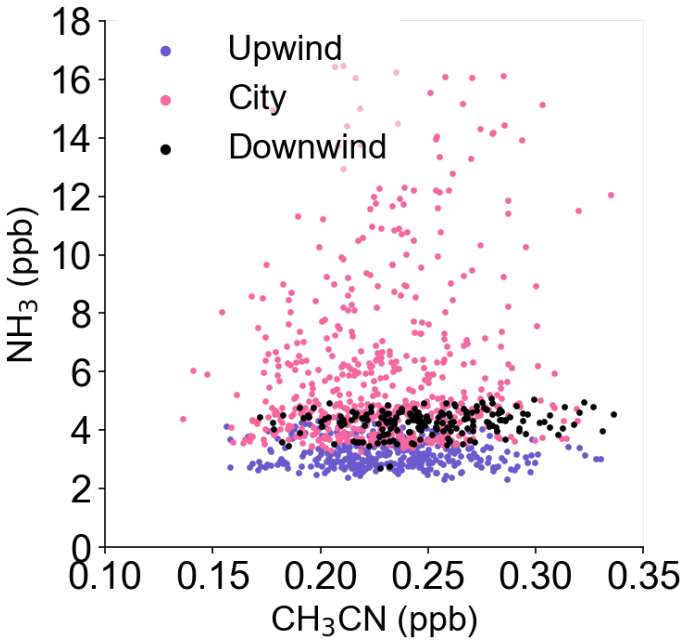

Figure B12: NH_3 v. CH_3CN for each segment of the 01 August 2023 Chicago flight.

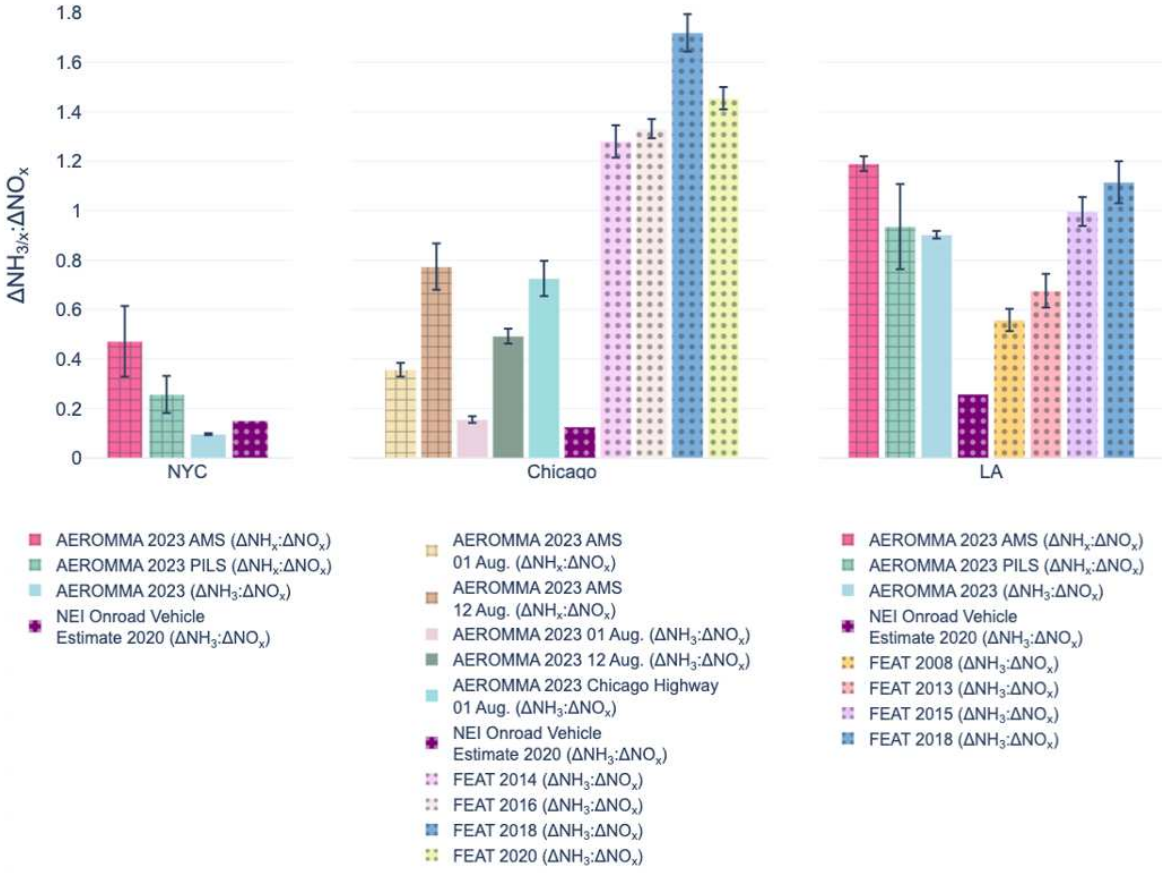

Figure B13: Bar chart of various $\Delta NH_{3/x}$:ΔNO_x ratios. AEROMMA NH_x ratios are denoted by hatched bars, AEROMMA NH_3 ratios are denoted by solid bars, and non-AEROMMA ratios are denoted by dotted bars. Note that the AEROMMA ratios for Chicago were taken from the downwind leg on the 01 August flight and the second downwind leg on the 12 August flight. The AEROMMA 2023 ratios in LA are an average of the three flights.

APPENDIX C

SUPPLEMENTAL INFORMATION FOR CHAPTER 4

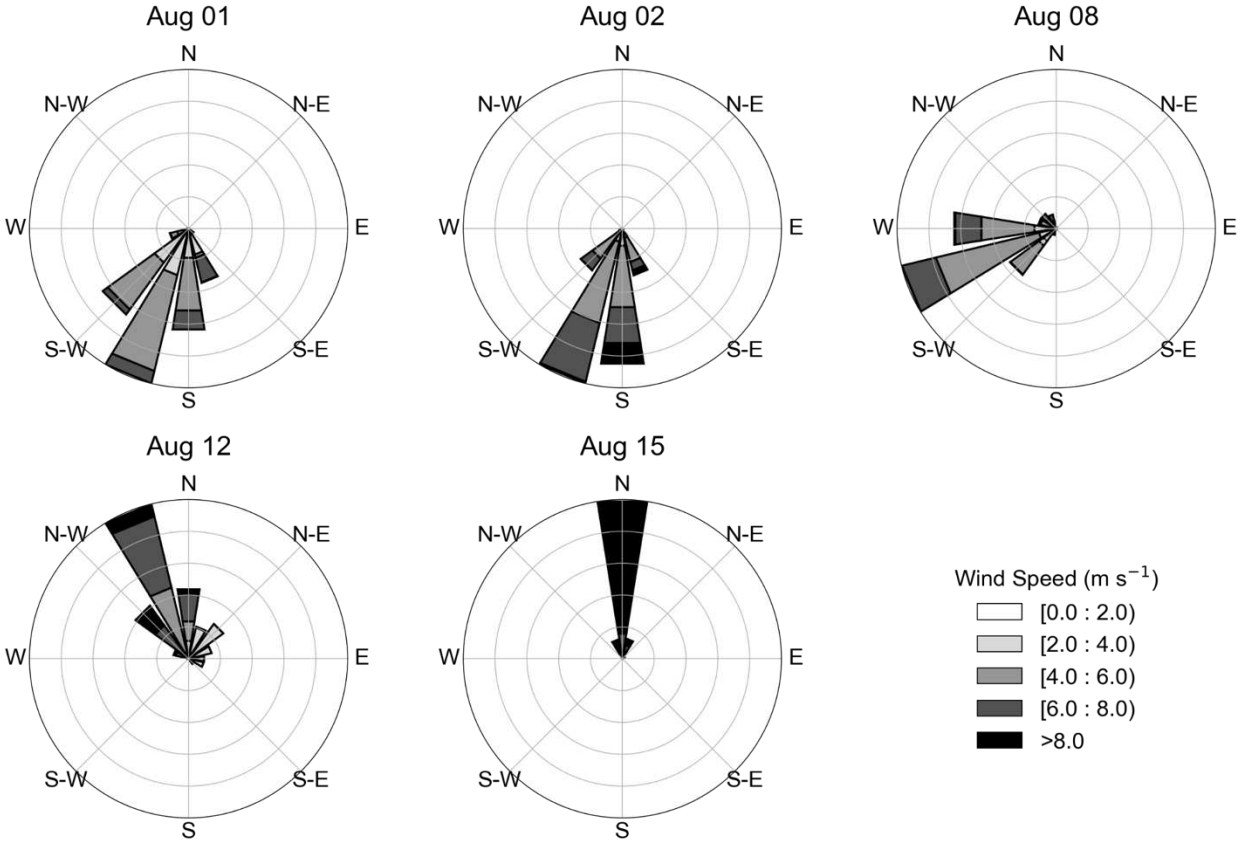

Figure C1: Wind roses for individual Chicago flights.

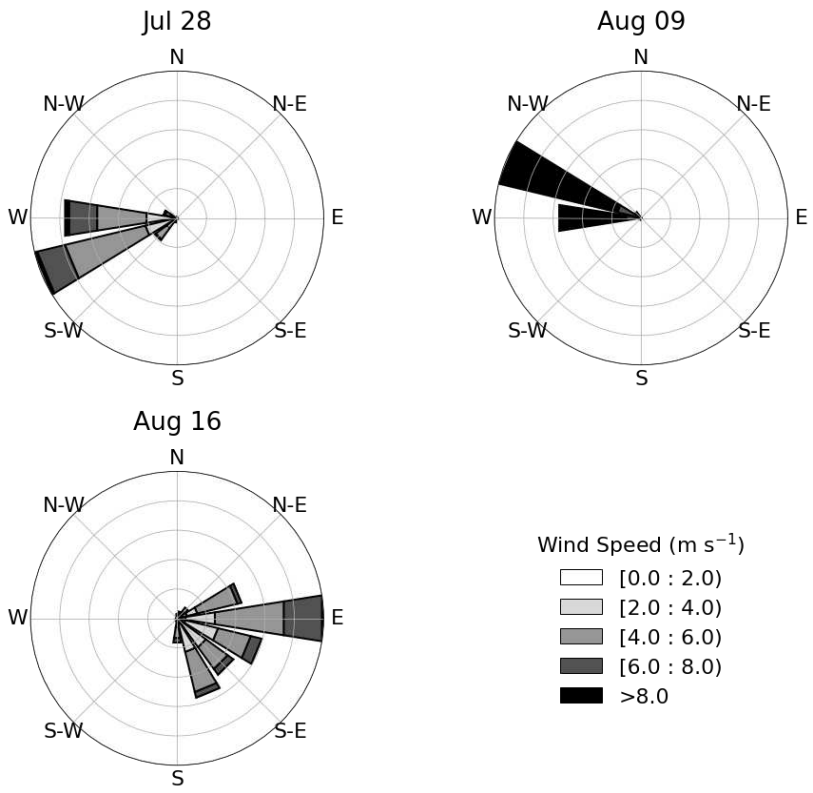

Figure C2: Wind roses for individual NYC flights.

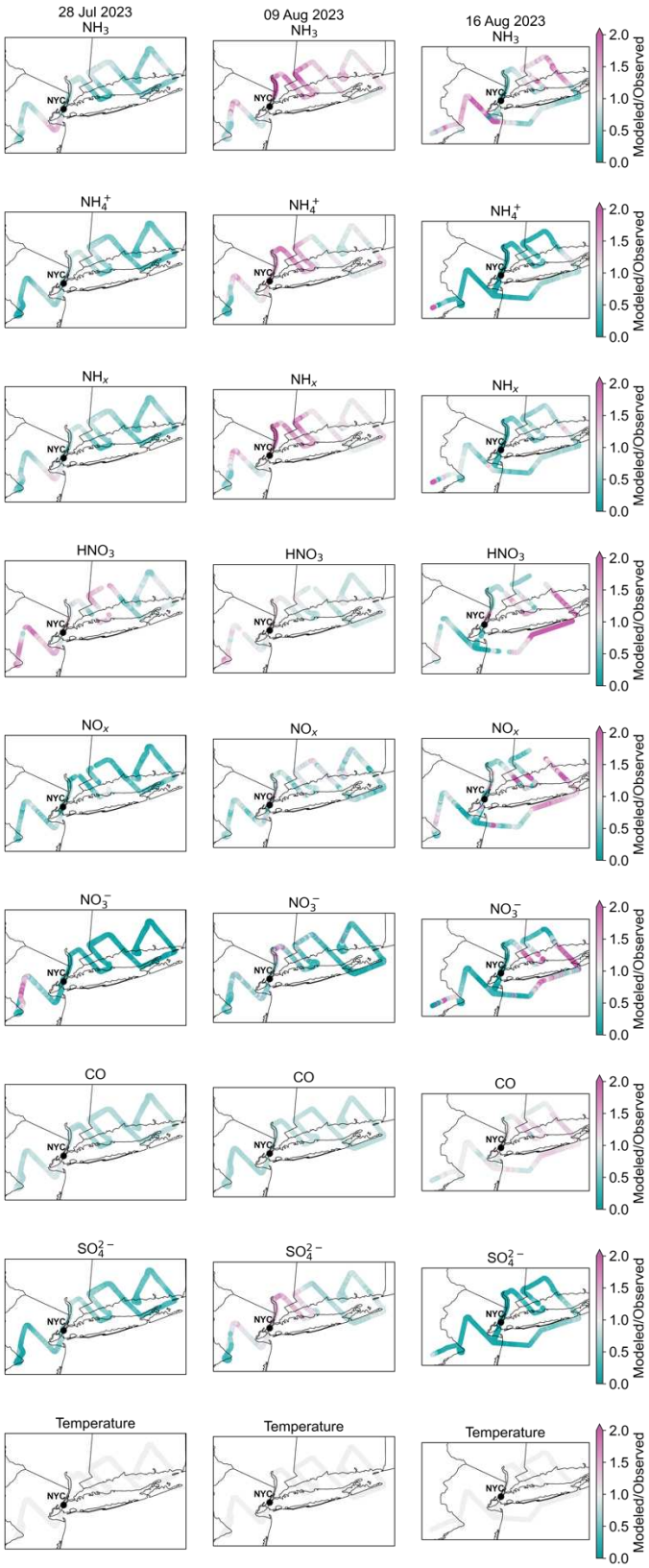

Figure C3: Maps of the modeled to observed ratio for NH_3, NH_4^+, NH_x, HNO_3, NO_x, NO_3^-, CO, SO_4^{2-}, and temperature for each individual flight in NYC.

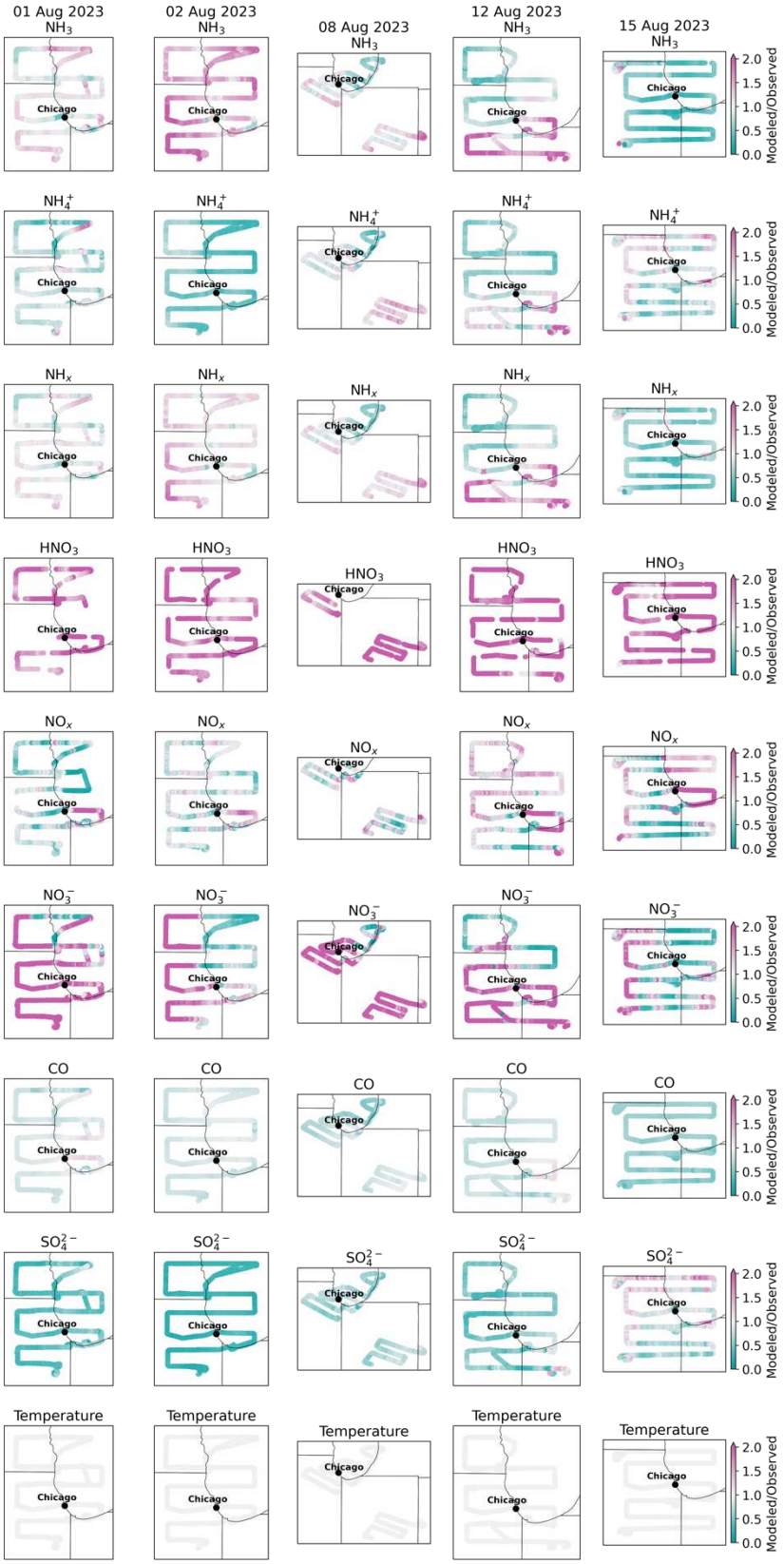

Figure C4: Maps of the modeled to observed ratio for NH_3, NH_4^+, NH_x, HNO_3, NO_x, NO_3^-, CO, SO_4^{2-}, and temperature for each individual flight in Chicago.

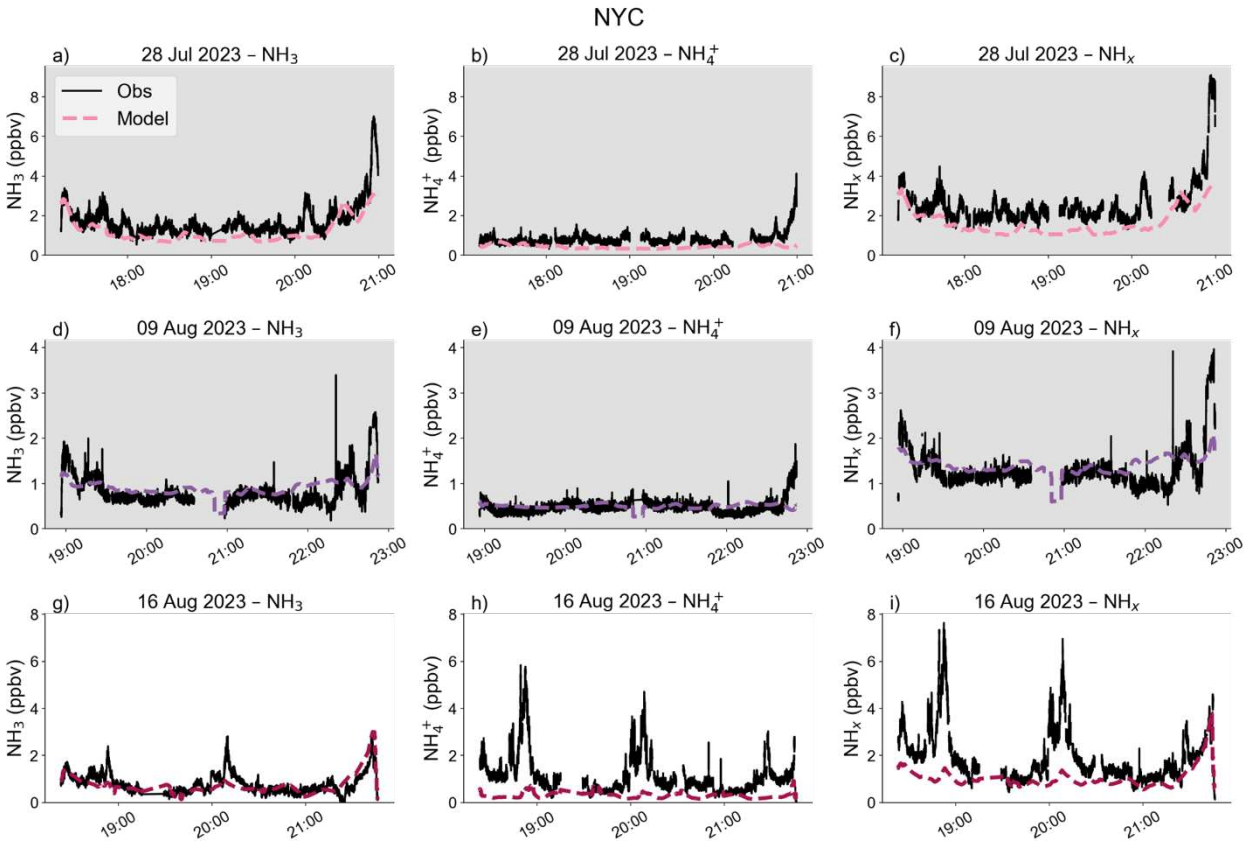

Figure C5: Timeseries of simulated (colored) and observed (black) NH_3 (a, d, g), NH_4^+ (b, e, h), and NH_x (c, f, i) for the 28 July, 09 August, and 16 August NYC flights. The grey shading indicates a smoke-impacted flight as determined in Chapter 3.

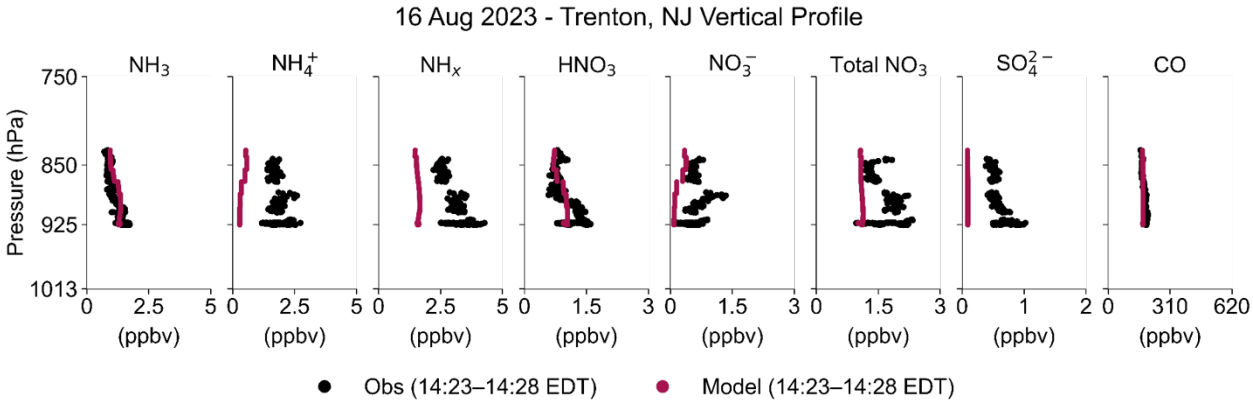

Figure C6: Vertical profiles over Trenton, NJ on 16 August. Observations are plotted in black while modeled data is plotted in red.

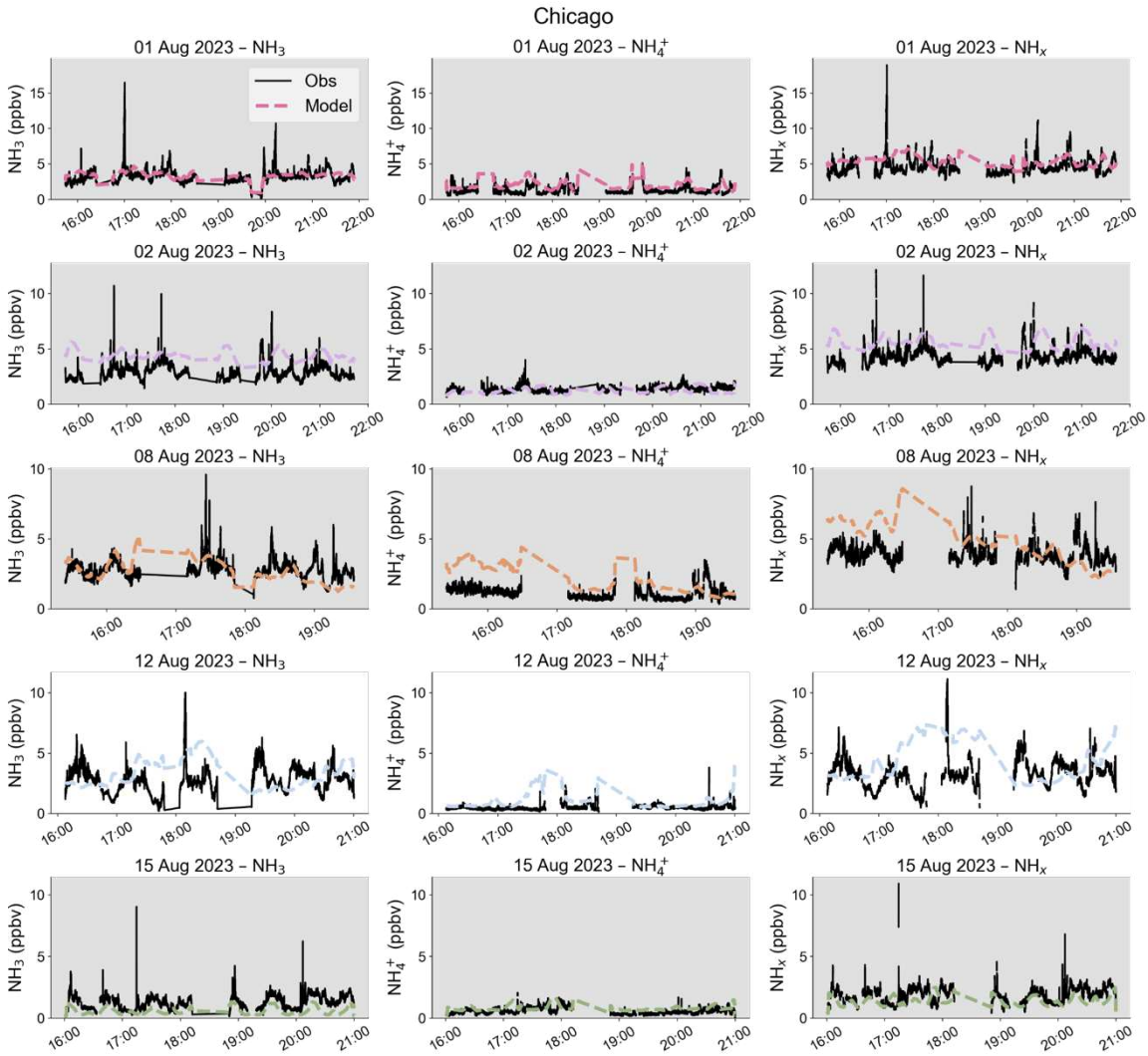

Figure C7: Vertical profiles of simulated (colored) and observed (black) NH_3 (a, d, g, j, m), NH_4^+ (b, e, h, k, n), and NH_x (c, f, i, l, o) for the 01 August, 02 August, 08 August, 12 August, and 15 August Chicago flights. The grey shading indicates a smoke-impacted flight as determined in Chapter 3.

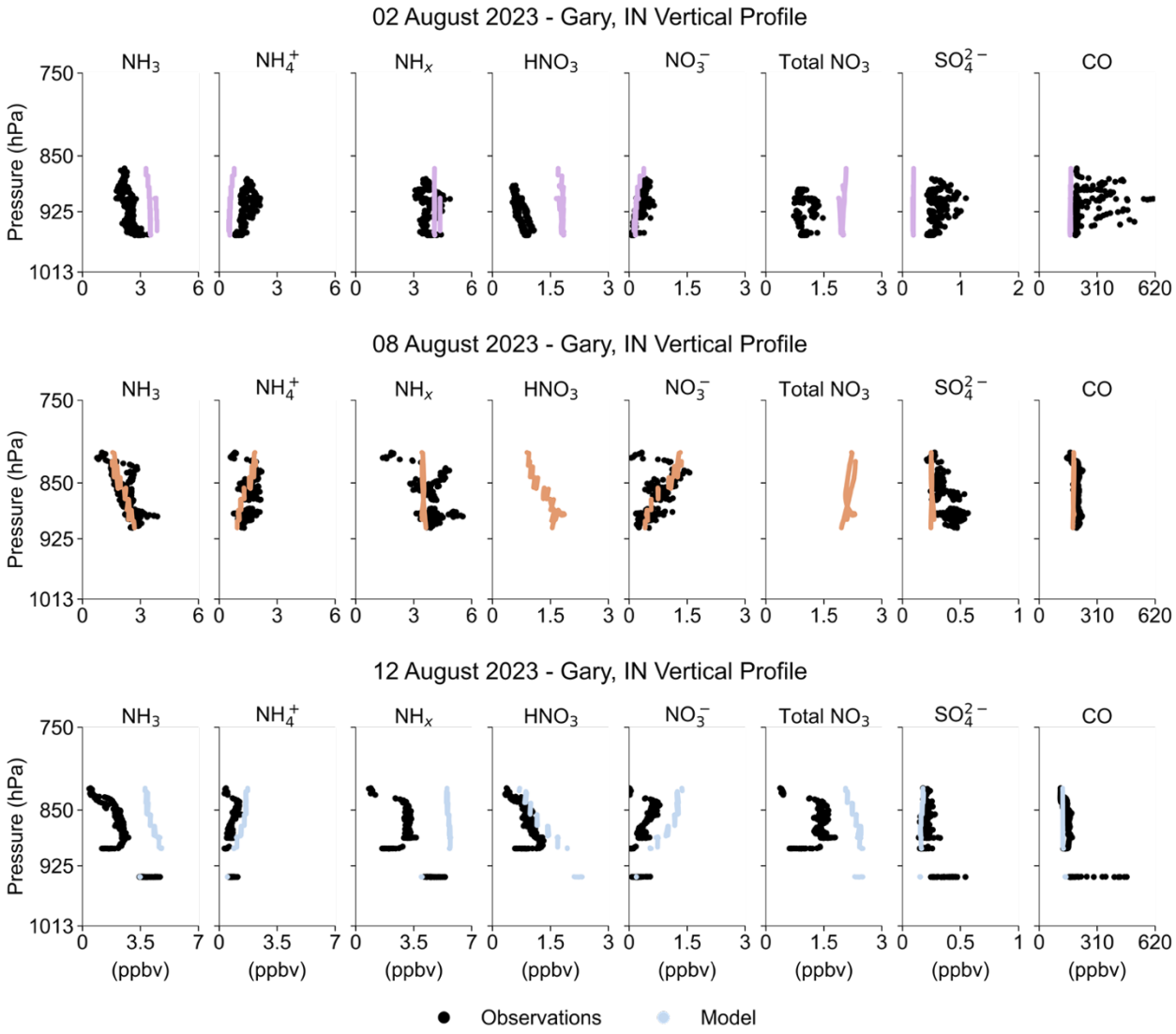

Figure C8: Vertical profiles near Gary, IN on 02 August, 08 August, and 12 August. Observations are plotted in black while modeled data is plotted in colors.

APPENDIX D

SUPPLEMENTAL INFORMATION FOR CHAPTER 4

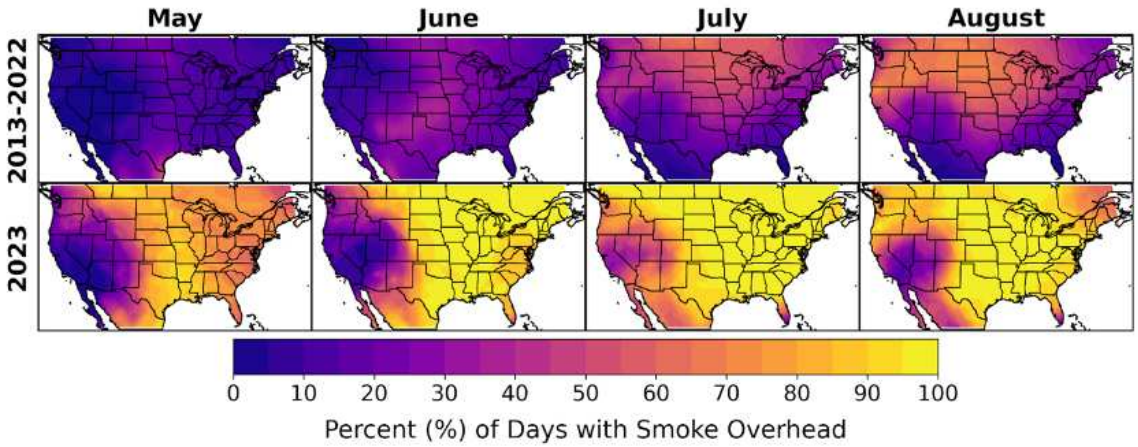

Figure D1: Percentage of days with smoke overhead in May, June, July, and August in 2023 (bottom row) and the 2013 - 2022 average (top row) based on the overlap of the HMS smoke product plume polygons with the centroid of a 1° grid.

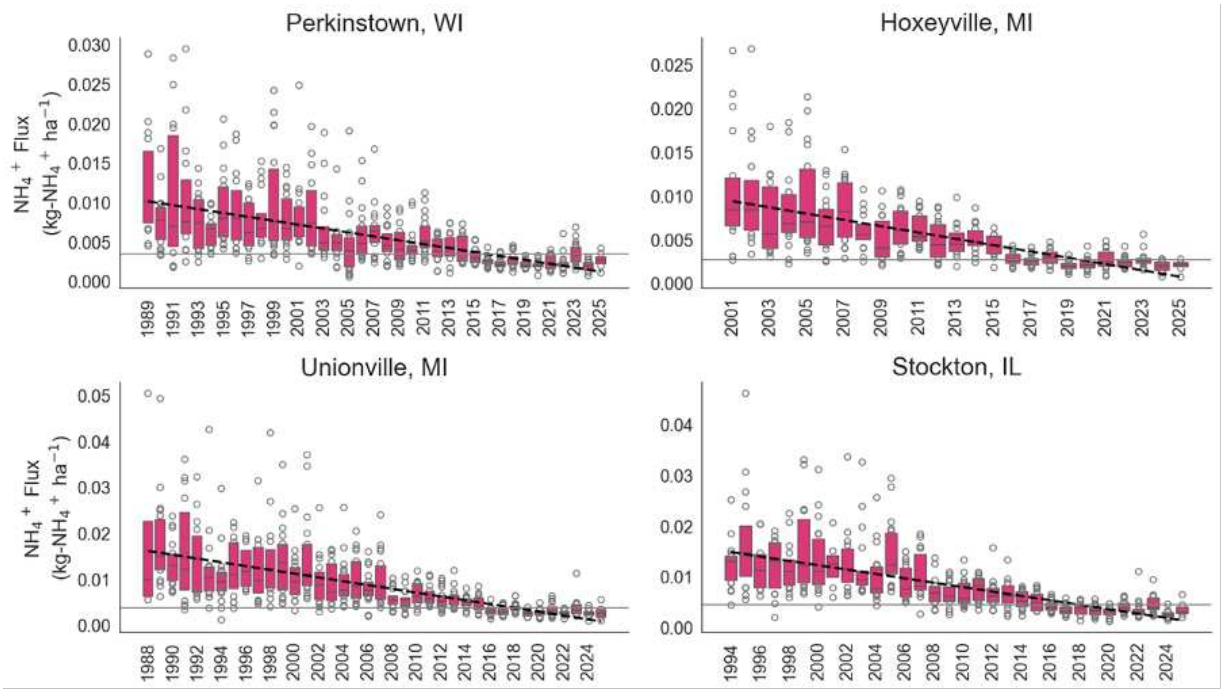

Figure D2: Time series of boxplots of 01 May - 01 August CASNET NH_4^+ deposition flux observations for sites in the Upper Midwest. The black dashed line indicates the trend of mean 01 May - 01 August values over time with the grey horizontal line indicating the mean value for 2023.

We use data from the Interagency Monitoring of Protected Visual Environments (IMPROVE) network from 2018 - 2023, which provides integrated filter concentrations for elemental carbon every third day. More information on the IMPROVE network can be found in Solomon et al. (2014).

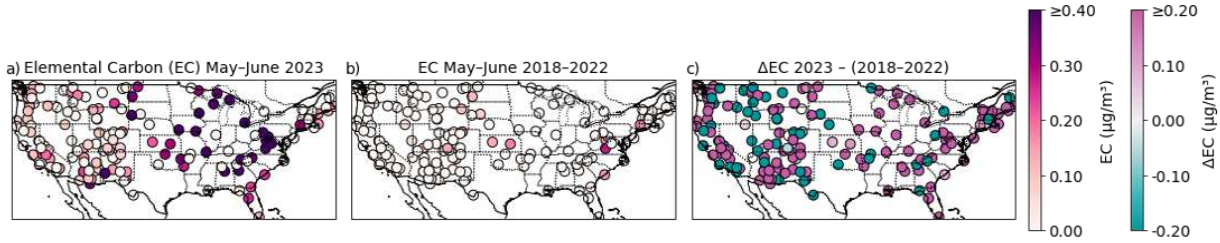

Figure D3: Maps of IMPROVE monitoring network elemental carbon stations colored by average May - June concentrations of NH3 and NH4+, respectively, in 2023 (a, d), average May - June in 2018 - 2022 (b, e), and the difference between the two averages (c, f).

Table S1: Site ID, location, and measurement start and end dates for each AMON site in the Upper Midwest.

Site ID	Site Location	Start Date	End Date
IL37	Stockton, IL	4/26/11 17:00	12/3/24 18:59
MI51	Unionville, MI	1/18/15 17:38	11/19/24 12:20
MI95	Hoxeyville, MI	1/13/15 15:50	12/3/24 13:26
MN02	Red Lake, MN	1/13/15 21:55	12/3/24 15:32
MN18	Fernberg, MN	12/21/10 17:30	12/3/24 15:20
WI01	Odanah, WI	10/2/18 9:07	12/3/24 15:36
WI06	Madison, WI	2/19/19 18:35	12/3/24 16:43
WI35	Perkinstown, WI	3/29/11 10:00	12/3/24 13:50

Table S2: Site ID, location, and measurement start and end dates for each CASTNET site in the Upper Midwest.

SITE ID	Site Location	Start Date	End Date
PRK134	Perkinstown, WI	5/2/89	6/17/25
HOX148	Hoxeyville, MI	5/1/01	6/17/25
UVL124	Unionville, MI	6/28/88	6/17/25
STK138	Stockton, IL	5/3/94	6/17/25

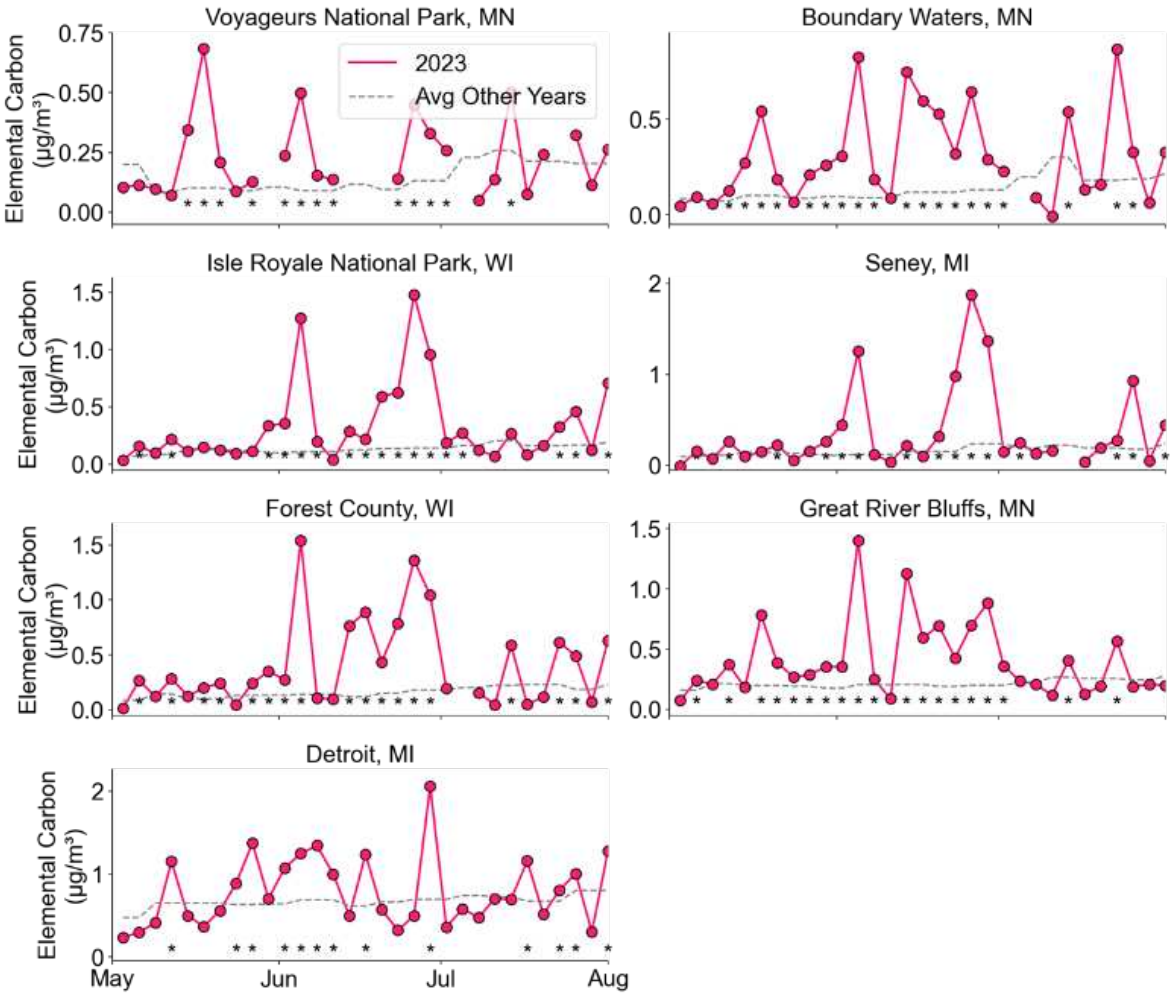

Figure D4: Time series of observed 01 May - 01 August IMPROVE elemental carbon concentration in 2023 (solid line) and the average of previous years (dashed line). The stars underneath points indicate if the 2023 value is significantly higher (95% confidence) than the mean of the non-2023 years.